UNIVERSITÀ DEGLI STUDI DI PALERMO

Dottorato di ricerca in Scienze Fisiche
Dipartimento di Fisica e Chimica
Fis/05

X-RAY MICROCALORIMETER DETECTORS – TECHNOLOGY DEVELOPMENTS FOR HIGH ENERGY ASTROPHYSICS SPACE MISSIONS

IL DOTTORE
SALVATORE FERRUGGIA BONURA

IL COORDINATORE
PROF. G. MASSIMO PALMA

IL TUTOR
PROF. MARCO BARBERA

CO TUTOR
DR. UGO LO CICERO

CICLO XXXII
2020

INDEX

ABSTRACT 4
INTRODUCTION 6
Chapter 1 _Neutron transmutation doped germanium microcalorimeters 13
1.1 Neutron transmutation doped germanium (NTD-Ge) 13
1.2 Microcalorimeter structure and operation 14
1.3 Array readout 26
1.4 Present device performances 26
1.5 Main applications 27
Chapter 2 _Absorber design for high energy NTD-Ge microcalorimeters 30
2.1 Absorbers design methodology 30
2.2 Material choice 31
2.3 Absorber design 35
Chapter 3 _Absorber fabrication 38
3.1 Bismuth layer growth techniques 38
3.2 The electroplating process 38
3.3 Bismuth electroplating 42
3.4 Absorber array microlithographic mask fabrication 53
3.5 Absorber array fabrication 55
3.6 Samples for Electrochemical Impedence Spectroscopy (EIS) 57
Chapter 4 Absorber characterization 59
4.1 Scanning electron microscope observation 59
4.2 Energy dispersive X-ray spectroscopy 59
4.3 Electrical bismuth layer characterization 59
4.4 Electrochemical impedance spectroscopy for bismuth layers 61
4.5 Other absorber characterization methods 65
4.6 Absorber characterization 68
4.7 Electrochemical Impedance Spectroscopy characterization 73
4.8 Conclusions 75

Chapter 5 Characterization of filters for microcalorimeters 77
5.1 Scope of the activity 77
5.2 Mechanical characterization of X-IFU filters 81
5.3 Radio frequency shielding of X-IFU filters 84
5.4 Radiation damage 88
5.5 Characterization conclusions 100
CONCLUSIONS 101
APPENDIX 102
REFERENCES 109
PUBLICATIONS 118
AKNOWLEDGMENTS 120

ABSTRACT

Improvements in the design, fabrication, and performance of astronomical detectors has ushered in the so-called era of multi messenger astrophysics, in which several different signals (electromagnetic waves, gravitational waves, neutrinos, cosmic rays) are processed to obtain detailed descriptions of their sources.

Soft x-ray instrumentation has been developed in the last decades and used on board numerous space missions. This has allowed a deep understanding of several physical phenomena taking place in astrophysical sources of different scales from normal stars to galaxy clusters and huge black holes. On the other hand, imaging and spectral capabilities in the the hard x-rays are still lagging behind with high potentials of discovery area.

Modern cryogenic microcalorimeters have two orders of magnitude or more better energy resolution with respect to CCD detectors at the same energy in the whole X-ray band. This significant improvement will permit important progress in high energy astrophysics thanks to the data that will be provided by future missions adopting this detector technology such as the ESA L2 mission Athena [1], the JAXA/NASA mission XRISM [2], both under development, or the NASA LYNX mission presently under investigation [3]. The JAXA/NASA mission Hitomi [4], launched in 2016 and failed before starting normal operation, has already given a hint of the high potential of such detectors [5].

Due to their very high sensitivity, X-ray cryogenic microcalorimeters need to be shielded from out of band radiation by the use of efficient thin filters.

These microcalorimeters work by measuring the temperature increase caused by a photon that hits an X-ray absorber. In neutron transmutation doped germanium (NTD Ge) devices the temperature increase in the absorber is measured by a semiconductor thermometer made of germanium doped by the neutron transmutation doping technique. They are characterized by relatively low specific heat and low sensitivity to external magnetic fields. These characteristics make them promising detectors for hard X-ray detectors for space and laboratory applications.

Research groups of the the X-ray Astronomy Calibration and Testing (XACT) Laboratory of the Osservatorio Astronomico di Palermo – Istituto Nazionale di Astrofisica (INAF-OAPA), and of the Dipartimento di Fisica e Chimica "Emilio Segrè" (DiFC) of the Università di Palermo have already developed experience related to the design, fabrication and testing of NTD Ge microcalorimeters [6, 7, 8, 9]. Furthermore, the research group has participated for many years in the design and development of filters for x-ray detectors in different space missions [10, 11, 12, 13].

This thesis concerns the development of materials and technologies for high energy microcalorimeters. In particular its aim is to design and fabricate thick bismuth absorbers for NTD germanium microcalorimeter arrays to extend their detection band toward hard X-ray energies. Filters for shielding microcalorimeters from different background radiation arriving on the detectors were also studied.

The design and fabrication of thick bismuth absorbers for hard x-rays detection (20 keV $\leq$ E $\leq$ 100 keV) is part of an ongoing effort to develop arrays of NTD Ge microcalorimeters by planar technologies for astrophysical applications. One potential application of such detectors is in the high spectral resolution (ΔE ~ 50 eV) investigation of the hard X-ray emission from the solar corona, which is the goal of a stratospheric balloon borne experiment concept named MIcrocalorimeters STratospheric ExpeRiment for solar hard X rays (MISTERX) presently under study at INAF-OAPA.

The characterization activity of filters for microcalorimeters in also related to the implementation of the European Space Agency high energy mission named Athena (Advanced Telescopes for High Energy Astrophysics).

This thesis describes the design, fabrication, and characterization of the bismuth absorbers, as well as the characterization of filters for Athena.

Chapter one summarizes the working principles of NTD Ge microcalorimeters and their applications. Chapter 2 describes the design of the bismuth absorber array on suitable substrates. Chapter 3 focuses on the electroplating process for the bismuth layer deposition, with details about the design and fabrication of the microlithographic mask for the array patterning, and about the development of the microlithographic process for the array fabrication on the chosen substrates. The fabrication of 4 x 4 absorber arrays is also described. Chapter 4 reports on the characterization activity of deposited bismuth layers by different techniques; their morphology was investigated by scanning electron microscopy. The electrochemical impedance spectroscopy technique was used to increase grown layer quality. Fabricated arrays were also characterized. Chapter 5 describes the characterization activity for different filter prototype samples developed for Athena. Mechanical robustness, radio frequency attenuation and radiation damage caused by protons were evaluated. Radiation damage effects at different doses were in particular investigated on silicon nitride filters by scanning electron microscopy (SEM), atomic force microscopy (AFM), UV-Vis-IR spectroscopy and x-ray attenuation measurements.

Details on both technical detector requirements and different sensor types are given in the Appendix.

INTRODUCTION

The first x-ray observation was performed in 1946, when the American astronomer Herbert Friedmann of Navy Research Laboratories looked at the Sun using a recovered V2 rocket [14]. In the years since, x-ray astronomy has become a very important research field. Many x-ray observatories have been launched in the outer part of terrestrial atmosphere and in space, both on balloons and on sophisticated satellites, like XMM-Newton and Chandra [15, 16, 17]. The development of x-ray observations, together with efforts in γ-ray detection, gave origin to modern High Energy Astrophysics that explores the hot and energetic part of the Universe.

X-ray emission has been detected through high energy space exploration in~~:~~ nearly all stars across the Hertzsprung-Russell diagram, binary systems, compact objects including black holes, supernova remnants, galaxy clusters and active galactic nuclei [15]. X-rays are produced by many phenomena, such as electronic transitions, Compton scattering, bremsstrahlung, black body radiation. Elemental composition, density, temperature and other environmental characteristics of the emitter can be evaluated by spectral analysis [18]. It was ascertained that x-ray emissions by stars influence their disk evolution, planet formation and planetary atmospheres [15].

The high performance achieved by X-ray devices in the last fifty years has contributed to the advancement of Multi-Messenger Astrophysics, in which signals of different type coming from the same source are observed, analyzed, and interpreted together [19, 20]. The signals include electromagnetic waves, neutrinos, cosmic rays, and gravitational waves.

An example that shows the importance of Multi-Messenger Astrophysics is GW17087, a gravitational wave observed by LIGO and VIRGO, followed by a gamma-ray burst 1.7s after. The electromagnetic follow-up campaign found an astronomical transient eleven hours after the gravitational wave signal, and that was observed from radio to x-ray wavelengths for weeks. This was not the first observed neutron star merger event, but it had the best quality data, making it the strongest evidence so far that short gamma-ray bursts are caused by neutron star mergers. [21].

CCDs are the most commonly used x-ray detectors in recent high energy missions. Cryogenic microcalorimeters measure the temperature increase when they absorb photons, and they outperform CCD detectors' energy resolution by two orders of magnitude or more [22].

Cryogenic microcalorimeters have been developed for or are currently planned for the following space missions:

- ASTRO-H (Hitomi) [23], developed by JAXA and NASA with the collaboration of many international space institutions; it was equipped with four instruments. One of which, the Soft X-ray Spectrometer (SXS), employed a 32 channel microcalorimeter array whose resolution is less than 7 eV in the 0.3 ÷ 12 keV band; Hitomi was launched on February 17, 2016 but unfortunately the mission failed before entering into normal operation. During the early in flight calibration, as the planned measurement were stopped by the mission failure, several useful information could be obtained with the Dewar still in thermal equilibrium. The SXS energy resolution was tested by an on board x-ray source. Emissions by two pulsar wind nebulae allowed to better measure the gate valve beryllium window thickness. The data collected during that phase confirmed expected SXS performances and proved the high potential of the x-ray microcalorimeter spectrometer technology [24].

- the X-ray imaging and spectroscopy mission (XRISM) [25], a joint JAXA/NASA collaborative mission, in which ESA also participates Its payload consists of two instruments, one of which, called Resolve, is a soft x-ray spectrometer, that includes an x-ray microcalorimeter array providing 5 ÷ 7 eV resolution in the 0.3 ÷ 12 keV band. XRISM's launch is scheduled for the end of 2021.

- The Advanced Telescope for High-Energy Astrophysics (Athena) [26] is the second Large (L2) astrophysics space mission selected by ESA in the Cosmic Vision 2015-2025 Science Programme to address the Hot and Energetic Universe science theme [27]. Athena will orbit the second Lagrange point of the Sun-Earth system (L2) and its launch is scheduled around 2030. It will be equipped with a 12 m focal length grazing incidence X-ray telescope based on the innovative Silicon Pore Optics technology, capable of providing 1.4 m^2 effective area at 1 keV with an angular resolution of 5 arcsec full width at half maximum (FWHM) over a large field of view (> 40 arcmin diameter)[28, 29]. The telescope will be mounted on a moveable platform which will allow both focus adjustment and tilt to point the X-ray beam on one of the two focal plane instruments: the X-Ray Integral Field Unit (X-IFU) [30, 31], an array of micro-calorimeters, and the Wide Field Imager (WFI), a large array of depleted field effect transistor (DEPFET) pixels[32, 33]. The X-IFU, based on an array of 3840 transition edge sensors (TES) microcalorimeters, will provide integral field spectroscopy in the range of 0.2-12 keV with an energy resolution of 2.5 eV FWHM up to 7 keV, and 5 arcsec half energy width (HEW) spatial resolution over a field of view of 5 arc minute equivalent diameter [30, 31].

- the Lynx X-ray observatory [34], a sophisticated soft x-ray observatory under development by NASA, employing a high performance microcalorimeter array with less than 3 eV resolution in the 0.2 ÷ 7 keV band; subarrays will also provide energy resolution up to 0.3 eV.

The main sources of noise for x-ray cryogenic microcalorimeters are:

- infrared radiation emitted by warm walls of the cryogenic Dewar in which they are mounted contributing to the photon shot noise (signals caused by random photons arriving on the sensor) on the full detector array. This perturbation causes a noise equivalent power (NEP) that reduces the energy resolution of detectors [35];
- visible and ultraviolet radiation emitted by space sources;
- RF electromagnetic radiation due to the onboard telemetry system and electronics;
- particles with energies of a few MeV or more, such as-protons, light and heavy ions, atoms, electrons emitted by energetic phenomena like solar flares or of galactic and extragalactic origins [36]. Cosmic galactic radiation (GCR) consisting of ions originating inside the Milky Way that had all electrons stripped and move at relativistic speeds, has to be mentioned due to their high energy content [37];
- molecular contamination due to particles trapped inside the microcalorimeter Dewar or desorbed by the spacecraft surfaces.

Filters are necessary to minimize the effects of noise. Ideal filters shield the sensors from all the noise sources mentioned above, while at the same time permitting x-rays to reach the detector. However, filters themselves produce photon shot noise by irradiation, but if they are well designed their contribution to energy resolution degradation is negligible [35].

Notice that high energy particles (E > 100 keV) can't be blocked by such filters and have to be rejected or identified by other means, like the anticoincidence detector.

While noise components are strongly attenuated by filters, the x-ray signal intensity reaching the detector will also be slightly reduced. The filters need to be designed to carefully balance their noise blocking power and the x-ray transmission.

Such filters have already been deployed in the microcalorimeter based observation instrument of the Hitomi space mission [38].

X-ray sensors for astrophysics

Since the discovery of x-rays, many devices to detect high energy photons have been developed [39, 40, 41, 42, 43]. In the years since, the progress in the fabrication technology has allowed the design and fabrication of several types of devices. The improvements in energy and spatial resolution, quantum efficiency, and detection rate that have been achieved over the years [39, 40] made them suitable for use in satellite instruments.

Gas detectors [39], the first invented x-ray sensors, are very easy to fabricate, but they have very poor energy resolution (about 1 keV at 6 - 8 keV energy). Similarly, scintillators [40] are characterized by some keV resolution at 50 – 60 keV radiation energy. Microchannel plates [40] have poor (0.05 – 0.1) quantum efficiency in the soft x-ray band, and CCD count rates are less than 100 Hz [42]. On the other hand, microcalorimeters [44, 45, 46] have very high energy resolutions, e.g 3.1 eV at 6 keV [47], but also higher sensitivity, quantum efficiency, and higher count rates (up to 300 – 500 cps).

Microcalorimeter detectors

When microcalorimeter detectors are hit by a photon, they absorb its energy and heat up. The change in temperature is measured by the change of some parameter of the system whose relationship to temperature is known such that the incident photon energy can be inferred.

The structure of a generic microcalorimeter is depicted in Figure 1.

The absorber is made of high Z (atomic number) materials, like tin, bismuth, or gold, in order to have a high stopping power for x-ray photons, and is the part of the microcalorimeter that absorbs the photon energy E and heats up. The absorber is placed in contact with the thermometer (e.g. doped semiconductor thermistor, transition edge superconducting film, superconducting inductors), in order to measure the temperature increase ΔT with respect to the operating temperature T_0. If the heat capacities of the absorber and the thermometer are C_a and C_t respectively, the resulting ΔT is:

$$\Delta T = \frac{E}{C_a + C_t} = \frac{E}{C_{tot}} \tag{0.1}$$

Both elements operate at cryogenic temperatures (20 – 50 mK) as both heat capacities assume very low values (e.g. $C_{bismuth} = 2.38 \cdot 10^{-15}$ $J \cdot K^{-1}$ @ 100 mK) in this range and thermal noise is small, allowing the detection of single photons.

After a photon is detected, a weak thermal link permits heat transfer from the thermometer to the thermal sink, also kept at a cryogenic temperature (T<100 mK). Once the thermometer has cooled back to its equilibrium temperature the microcalorimeter is ready to measure the energy of another photon. The thermal time constant τ of this process is:

$$\tau = \frac{C_{tot}}{G} \tag{0.2}$$

in which G is the heat conductance of the weak thermal link. The detector is read by an electronic circuit based on a very low noise, high gain input amplifier.

Several types of microcalorimeters exist based on specific physical phenomena and structures including:

1) neutron transmutation doped germanium (NTD Ge);
2) transition edge sensors (TESs);
3) metallic magnetic microcalorimeters (MMCs);
4) thermal kinetic inductance detectors (TKIDs).

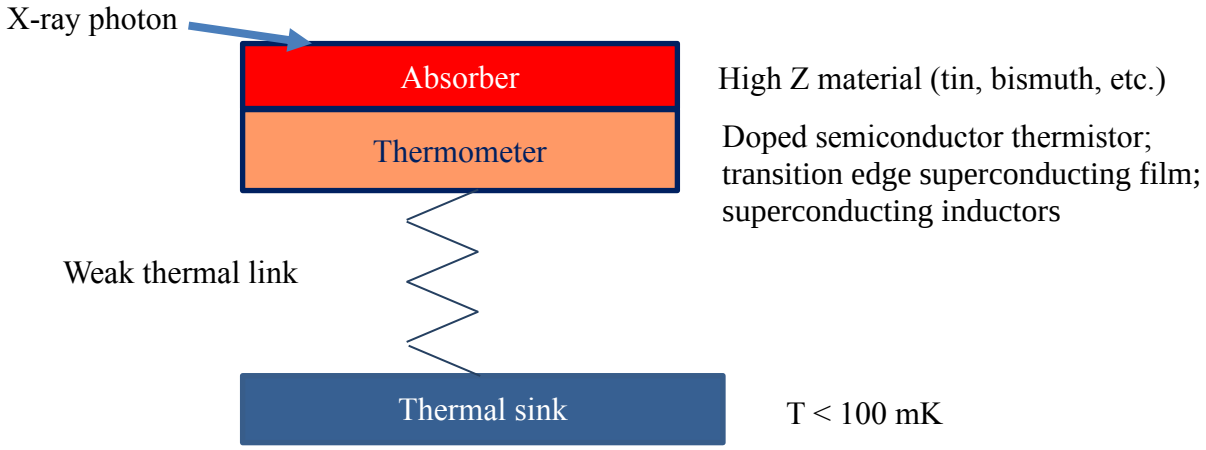

Figure 1 - Schematic of a generic microcalorimeter.

The energy resolution limit of a microcalorimeter is given by [48]:

$$\Delta E_{FWHM} \cong 2.355\xi\sqrt{k_B T_0^2 C_{tot}} \tag{0.3}$$

in which k_B is the Boltzmann constant and ξ-depends on the sensitivity of the thermal sensor used in the specific microcalorimeter technology, and is usually of order one.

- **Neutron transmutation doped germanium (NTD Ge) microcalorimeters**

NTD Ge microcalorimeters are based on the measurement of the temperature increase in the absorber by a semiconductor thermometer [45] made of NTD Ge. This heating is due to the x-ray photon absorption, mainly by photoelectric effect and related thermalization caused by the electron to phonon energy conversion.

NTD Ge microcalorimeter energy resolutions (FWHM) are 3.1 eV @ 6 keV [47] and 50 eV @ 60 keV [49].

- **Transition edge sensors (TESs)**

Transition edge sensor microcalorimeters [46] have the same structure of NTD Ge ones, with the absorber placed on top of the thermometer. In this case the thermometer is made of a superconducting thin film operating at the phase transition temperature.

When the x-ray photon hits the absorber, the temperature increase causes a transition to the non-superconducting state of the thin film; the temperature increase is given by (0.1) and the thermal time constant by (0.2). In order to be read out, TES microcalorimeters are inductively coupled to low noise superconducting quantum interference device (SQUID) amplifiers.

The thin film is usually made of a metal bilayer (Ti/Au, Mo/Au, etc.) with a total thickness of ten to a hundred nanometers, whose transition temperature is in the range 50 to 200mK. The resistance at temperatures above its transition temperature is around a few milliohms.

The TES energy resolution is around 1.6 eV FWHM @ 5.9 keV [50]; up to now they have been planned for soft X-ray photon detection (e.g. Athena X-IFU instrument).

- **Metallic magnetic microcalorimeters (MMCs)**

Metallic magnetic microcalorimeters [51] are made of an absorber in contact with a magnetic sensor, made of a gold or silver film doped with paramagnetic erbium. The detector works below 50 mK; a small magnetic field is applied so that Zeman levels of erbium are split and unevenly occupied.

When an x-ray photon is absorbed and the system heats up, erbium spins are excited into the higher energy state and the magnetization varies; this change can be read out by a SQUID amplifier. A weak thermal link transfers heat from the absorber to the sink.

An important advantage of this type of microcalorimeter-is the nearly linear response, apart from a small quadratic dependence of both heat capacity and susceptibility by the temperature [52].

The energy resolution of MMCs can be as high as 1.58 eV @ 5.9 keV [51] and better than 40 eV FWHM @ 60 keV [52].

- **Thermal kinetic inductance detectors (TKIDs)**

These devices [53] are based on the same working principle as microwave kinetic inductance detectors (MKIDs) [43], where the frequency change of a resonator is measured to detect incident photons. The x-ray absorber is connected to the resonator so that heat produced by photon absorption breaks Cooper pairs in the superconducting inductor, and as a consequence the resonator frequency changes. [54]. Their energy resolution (about 10 eV @ 6 keV [53]) is less than that of NTD Ge and TES, but TKIDs have the same great advantage of MKIDs of frequency domain multiplexing for reading out very large (thousands of pixels) microcalorimeter arrays [43].

Microcalorimeter filters

As mentioned above, filters are necessary to shield the detectors from noise, while at the same time allowing signals to come through.

A series of five filters made of a polyimide membrane coated with an aluminum layer and, for three of them, supported by a silicon mesh, was used in the 36 pixel array of the Hitomi X-ray

Calorimeter Spectrometer (XCS) of the Soft X-ray Spectrometer (SXS) instrument [38]. These filters shield from UV and longer wavelength radiation.

Filters made of 90 nm polyimide coated with 80 nm aluminum were used to implement the same filtering structure in ASTRO-E and in Suzaku (ASTRO-E2) [55].

Both the X-IFU and WFI instruments of Athena are currently being designed with filters made of polyimide films coated with thin aluminum layers; polyimide films are glued to metallic meshes with hexagonal cells, and the whole structure is then fixed to a metallic frame.

In particular, a polyimide-based five filter series, in which a very thin layer (45 nanometers) of this polymer is covered with one- or both side 30 nm thickness aluminum films and supported by a stainless steel 40 ÷ 80 μm thick mesh, is being developed for the X-IFU, and their design is still ongoing [56, 57].

The Resolve instrument of XRISM [58] employs the same filters of SXS; in this case transmission specifications are 5.10^{-3} and 5.10^{-4} for visible and infrared radiation (3 ÷ 25 μm), respectively, for the two thinner filters, and 5.10^{-5} and 1.10^{-4} for visible and infrared radiation, respectively for the three thicker, mesh supported ones.

A more complex filtering structure is being designed for the LYNX mission, in which a series of six filters will be used: four made of a polyimide membrane coated with a thin aluminum layer and supported by silicon meshes, and two are waveguide cut-off filters; they don't use thin films [59].

Another type of filter, developed by AMETEK (Finland), is presently under consideration for their possible use for future space missions; they are made of a thin silicon nitride (Si_3N_4) layer whose thickness is between 20 and 40 nm and covered on one or both sides by thin (10 ÷ 15 nm) aluminum films and attached to a silicon mesh.

Research framework of this thesis

The topics discussed in this thesis concern two research activities that are currently under development at the X-ray Astronomy Calibration and Testing (XACT) Laboratory of the Osservatorio Astronomico di Palermo – Istituto Nazionale di Astrofisica (INAF-OAPA), and at the Dipartimento di Fisica e Chimica "Emilio Segrè" (DiFC) of the Università di Palermo, namely:

1) development of cryogenic microcalorimeter detector;

2) development of filters for x-ray detectors in space missions.

The first activity concerns, in particular, the design and fabrication of hard X-ray (20 keV ≤ E ≤ 100 keV) neutron transmutation doped germanium (NTD Ge) microcalorimeter arrays by planar technology. This work will be based on the experience of the INAF-OAPA and DiFC research groups on the use of NTD Ge microcalorimeters for soft X-ray detection, and technology developments towards planar array fabrication [6, 7, 8, 9].

These microcalorimeter arrays are mainly aimed at astrophysical applications, and they are baselined for the stratospheric balloon borne experiment concept MISTERX presently under study at INAF-OAPA aimed at observing hard X-rays from the solar corona in the 20÷100 keV energy band, with an energy resolution of about ΔE=50 eV.

During solar flares, hard X-rays are emitted in the hot (well above 10 MK) plasma, due to the impact with the star surface of relativistic electrons guided by the magnetic field. However, this standard model is not able to explain some recent data [60] provided by the Reuven Hamaty high energy solar spectroscopic imager (RHESSI) [61] mission, that for about 16 years observed these events using nine high purity germanium crystal (HPGe) detectors with about 1 keV energy

resolution. This spectral resolution, achieved also in other smaller balloon-borne experiments, is appropriate to constrain the general features of the non-thermal component of the solar emission, e.g. the slope of the power law, but does not discern any deviation from the envelope trend, nor resolve any possible spectral line, which might come from highly ionized heavy elements.

Single flare energy has a broad distribution: very energetic flares are rare events, whilst lower energy ones are more frequent. The flaring process analysis is very scientifically relevant~~,~~ due to the influence that magnetic storms caused by flares have on Earth, and because advances in plasma physics that can be obtained by the understanding of flare behavior. Many studies are currently ongoing on solar flare analysis in the hard X-ray band, in particular to better understand the related electronic transport [60, 62].

The MISTERX experiment will improve the spectral energy resolution to 50 eV, greatly benefitting the solar flare observations. This improvement will be allowed by the use of hard X-ray NTD Ge microcalorimeter arrays currently under development at INAF-OAPa. The high cadence and high energy resolution of the MISTERX experiment will allow the investigation of impulsive magnetic reconnection and heating mechanisms in the solar corona and accurate diagnostics of thermal and non-thermal emission. One advantage will be the automatic cut-off of the softer overwhelming thermal emission, complementing observations, e.g., NuSTAR [63], thus allowing exclusive detection of the highest temperature components and details of the non-thermal ones.

The second research activity described in this work is related to filter development for the Athena mission. The research group at INAF-OAPa and DiFC I collaborated with is responsible for the design, development and characterization of the filters for both of the Athena instruments, namely the X-IFU and WFI. Besides the efforts for Athena, new filters based on silicon nitride have been investigated within an ESA R&D contract.

Chapter 1

NEUTRON TRANSMUTATION DOPED GERMANIUM MICROCALORIMETERS

1.1 Neutron transmutation doped germanium (NTD-Ge)

Doped semiconductors are well suited to fabricate low temperature thermometers due to their very sensitive resisitivity dependence on temperature and low noise at cryogenic temperatures; in particular, doped germanium allows very high sensitivities compared to silicon due to its smaller bandgap.

Doped crystals grown by the Czochralski method do not present a very homogeneous doping atom concentration as this parameter depends on the effective segregation coefficient and the impurity concentration in the liquid phase [64]. Doping inhomogeneities of the crystal on micron–to–millimeter scale, may result both in the radial and longitudinal directions. This implies that the electrical conduction in such materials is locally dependent on the doping concentration, making these crystals unsuitable for low temperature thermistors.

The best technique to produce very homogeneous doping in semiconductors is neutron transmutation doping (NTD) [65], that consists in exposing semiconductor crystals to a neutron flux in a nuclear reactor. This technique is based on the transmutation of semiconductor isotopes when they capture slow (thermal, whose energy is about 0.025 eV) neutrons. Several nuclear reactions can take place depending on the isotopic distribution of the irradiated material.

This method was used for both silicon and germanium, in fact, power electronic devices (e.g. rectifier diodes) also need very homogeneously doped semiconductors.

The starting nuclear reaction is [65]:

$$\Phi\sigma_i {}^{A}_{z}N \quad = {}^{A+1}_{z}N \tag{1.1}$$

where:

Φ is the neutron irradiation dose;
σ_i is the thermal neutrons capture cross section for the i-isotope;
${}^{A}_{z}N$ is the initial reaction specie concentration;
${}^{A+1}_{z}N$ is the final reaction product concentration;
z is the nuclear charge;
A is the nuclear mass.

The capture cross section generally depends on the neutron energy E as:

$$\sigma_i \sim E^{-0.5} \tag{1.2}$$

for E up to about 10^4 eV.

When produced isotopes, with increased mass number, are unstable they decay with their half-life time τ_i; β decay (one neutron emits an electron and transforms itself in a proton) produces elements with increased atomic number $z+1$, whilst K-capture (the nucleus capture a K-shell electron of the same atom) originates decreased atomic number $z-1$ elements; in formulas:

$$ {}^{A+1}_{z}N \quad -\beta \rightarrow {}^{A+1}_{z+1}N \tag{1.3} $$

$$ {}^{A+1}_{z}N \quad -K-capture \rightarrow {}^{A+1}_{z-1}N \tag{1.4} $$

When the semiconductor is germanium, three different elements are formed: gallium (Ga), arsenic (As), and selenium (Se), according to the following reactions, starting from the active isotopes ${}^{70}_{32}Ge$, ${}^{74}_{32}Ge$ and ${}^{76}_{32}Ge$:

$$ {}^{70}_{32}Ge \quad +n = {}^{71}_{32}Ge \quad -K-capture \rightarrow {}^{71}_{31}Ga \tag{1.5} $$

$$ {}^{74}_{32}Ge \quad +n = {}^{75}_{32}Ge \quad -\beta \rightarrow {}^{75}_{33}As \tag{1.6} $$

$$ {}^{76}_{32}Ge \quad +n = {}^{77}_{32}Ge \quad -\beta \rightarrow {}^{77}_{33}As \quad -\beta \rightarrow {}^{77}_{34}Se \tag{1.7} $$

Gallium is an acceptor dopant, while arsenic and selenium are donors. Since the former is produced in concentration N_A, which is greater than the sum (N_{AS} +2N_{SE} , as selenium is a double donor) a p-type doping of germanium is obtained. The net doping concentration depends on the irradiation fluence.

The compensation ratio K defined in (1.8) is an important parameter describing the material behavior:

$$ K = \frac{N_{AS}+2N_{SE}}{N_A} \tag{1.8} $$

After the neutron irradiation, a sufficient time must be waited for all unstable isotopes to decay, before the doped semiconductor can be safely handled and used. Furthermore, in order to optimize the doped crystal quality, a thermal annealing is necessary to remove defects caused by the interaction of fast neutrons, present in the irradiation beam, with crystal impurities. Usually, different temperature, duration and atmospheric conditions annealing steps are required [65, 66].

1.2 Microcalorimeter structure and operation

In an NTD-Ge microcalorimeter the temperature increase caused by the absorption of an x-ray photon is measured by a thermistor consisting of a germanium crystal doped with the NTD technique previously described with a volume of the order of 10^4 μm^3. The sensitive thermistor (a resistor whose resistance varies with temperature) is connected to a suitable electronic read-out circuit, based on a very low noise high gain input amplifier, that allows to measure the dynamic resistance which, by proper calibration, can be directly correlated to the device temperature and thus to the absorbed photon energy.

The weak thermal link to the cold bath is needed to cool the detector (absorber+thermometer) to the operating temperature (< 100 mK) and thus be ready to detect the next photon. The temperature recovery time is tipically of the order of few hundreds of microseconds.

1.2.1 The absorber

At x-ray energies (0.1÷100 keV) the photoelectric effect is the main photon absorption process in high Z materials. The primary photoelectron and secondary electrons interact with the crystal atoms initially by further ionization and electrons excitation into bound states, and successively by energy transfer from electrons to phonons (thermalization).

The photoelectric effect cross section at a given photon energy E depends on the absorbing material mass attenuation coefficient $\mu/\rho(E)$, in which μ is its linear attenuation coefficient at energy E and ρ is its density. The larger is μ/ρ, the more absorbing is the material.

The mass attenuation coefficient, in the regime dominated by the photoelectric effect, can be calculated by [67]:

$$\frac{\mu}{\rho} = \sum_i w_i \left(\frac{\mu}{\rho}\right)_i \tag{1.9}$$

$$\left(\frac{\mu}{\rho}\right)_i = \frac{(\sigma_{pe})_i}{uA_i} \tag{1.10}$$

where:

w_i is the weight fraction of the ith atomic element in the molecule;
$\left(\frac{\mu}{\rho}\right)_i$ is the mass attenuation coefficient of the ith atomic element in the molecule;
σ_{pe} is the photoelectric cross section of the ith atomic element in the molecule;
u is the atomic mass unit ($1.660 \cdot 10^{-24}$ g);
A_i is the Atomic mass number of the ith atomic element in the molecule.

The photoelectric cross section depends on photon energy, and on the atomic number Z by [68]:

$$\sigma_{pe} \sim \frac{Z^4}{(h\nu)^3} \qquad \text{(low energy, } h\nu < 0.9E_{el}\text{)} \tag{1.11}$$

$$\sigma_{pe} \sim \frac{Z^5}{h\nu} \qquad \text{(high energy, } h\nu > 0.9E_{el}\text{)} \tag{1.12}$$

In (1.11) and (1.12) $E_{el} = m_e c^2$=511 keV.

Calculated values of σ_{pe} for Z=1 to Z=92 and for the energy range 1 ÷ 1500 keV have been published by J. H. Scofield [69].

From equations (1.11) e (1.12) it is evident that high-Z elements have a larger photoelectric cross section and thus larger attenuation coefficient. For this reason, absorbers are made of high Z materials (tin, gold, bismuth). Table 1.1 reports μ/ρ values at E=100 keV [70] for few high Z elements and lithium for comparison.

Table 1.1 - Mass attenuation coefficient for some selected elements at E=100 keV.

Element	Z	μ/ρ [cm^2/g]
Lithium	3	$1.289 \cdot 10^{-1}$
Tin	50	1.676
Gold	79	5.158
Bismuth	83	5.739

Heat capacity

Another important parameter of the absorber is its heat capacity that influences both the energy resolution and the time constant. As it is evident from equations (0.3) and (0.2), both the energy resolution and the recovery time to the temperature of the cold bath decrease with decreasing heat capacity. For this reason, microcalorimeter absorbers should have a low heat capacity C_a:

$$C_a = c_{p,v} d_a V_a \tag{1.13}$$

where:
$c_{p,v}$ is the specific heat of the material;
d_a is the material density;
V_a is the absorber volume.

On the other hand, the heat capacity cannot be arbitrarily small, otherwise, the absorption of an x-ray photon can cause an excess temperature rise and thus bring the thermistor and read-out electronics in non-linear behavior. Once the absorber material is chosen, the volume is calculated based on performance specifications.

The specific heat has electrons and a phonons contributions depending on the type of material (insulator, normal metal, superconducting metal).

<u>Normal metals</u>

For normal metals, the specific heat is given by the sum of the lattice contribution c_{ph} and the electronic one c_e. The former, according to the Debye model, is related to the total lattice energy, given by the sum of all phonon modes, and is expressed by [71]:

$$c_{ph} = 9R\left(\frac{T}{\theta_D}\right)^3 \int_0^{\frac{\theta_D}{T}} \frac{x^4 e^x}{(e^x-1)^2} dx \tag{1.14}$$

In (1.14) T is the working temperature, R is the gas constant (8.31 J/mol·K) and θ_D is the Debye temperature:

$$\theta_D = \frac{\hbar v_{ph}}{k_B}\left(\frac{3N}{4\pi V}\right)^{\frac{1}{3}} \tag{1.15}$$

where:

$\hbar$ is the reduced Plank constant ($1.055 \cdot 10^{-34}$ J·s);

v_{ph} the sound speed in the material;
k_B the Boltzmann constant ($1.38 \cdot 10^{-23}$ J·K^{-1});
N/V the number density of atoms.

When $T << \theta_D$ we have:

$$\lim_{T \to 0} c_{ph} = \frac{12\pi^4 N_A k_B}{5} \left(\frac{T}{\theta_D}\right)^3 \tag{1.16}$$

with N_A the Avogadro number ($6.022 \cdot 10^{-23}$).

The electronic contribution c_e is related only to electrons whose energy E_e is:

$$E_e \geq E_F - k_B T \tag{1.17}$$

in fact, lower energy electrons see their neighbor levels completely filled, E_F is the Fermi energy:

$$E_F = \frac{\hbar}{2m_e} \left(\frac{3\pi^2 N}{V}\right)^{\frac{2}{3}} \tag{1.18}$$

in which m_e is the electron mass ($9.109 \cdot 10^{-31}$ kg).

According to the free electron gas model, the free electron contribution to the normal metal specific heat at temperatures lower than both the Debye and the Fermi ones $T_F = E_F/k_B$ is [71]:

$$c_e = \frac{\pi^2 N_A k_B T}{2T_F} \tag{1.19}$$

The total specific heat of normal metals at very low temperatures ($T << \theta_D, T_F$) can thus be written as the sum of the two above contributions:

$$c = c_{ph} + c_e = \alpha T^3 + \gamma T \tag{1.20}$$

in which α and γ are constants depending on the material. Notice that the specific heat decreases with temperature, thus, in order to have a low heat capacity, microcalorimeters need to be operated at cryogenic temperature (T<100 mK).

Superconducting metals

Superconducting metal specific heat was studied by the Bardeen-Cooper-Schrieffer (BCS) theory [72]. This theory states that in a superconductor metal electrons are grouped in pairs, said Cooper pairs, that are all related among them; when an electric field is applied at the superconductor, all the electrons moves without encountering any resistance, and this electric current exists also after the field goes to zero. To stop the current it is necessary to heat the metal until it recoveries its normal conduction characteristics, with pairs separating into two electrons.

Cooper pairs are formed due to the electron-phonon interaction (the phonon is the collective motion of the positively charged crystal lattice). This interaction is a quantum effect.

Decreasing the metal temperature, superconductivity begins at the transition temperature T_c, depending on the material. Different metals that could be used for the absorber fabrication are superconductors at cryogenic operating temperatures of NTD Ge microcalorimeters (T<100 mK), as demonstrated by Table 1.2; others, like bismuth, remain normal conductors.

Table 1.2 - Transition temperature T_c for different superconductors.

Metal	T_c [K]
Bi	$5.3 \cdot 10^{-4}$
Os	0.65
Sn	3.72
Ta	4.48

In superconductors at temperatures below the transition, the specific heat doesn't have any contribution by electrons, that are bound in Cooper pairs; from BCS theory, then, the expression for the specific heat is:

$$c_s = \gamma T_c a e^{-\frac{bT_c}{T}} \tag{1.21}$$

where:

γ: is the coefficient of free electrons specific heat (see 1.20) at T > T_c;
a, b are material depending constants.

Useful tables reporting specific heats of several solids at low temperatures are collected in [73].

Thermal conductivity

Besides specific heat, thermal conductivity is an important property for absorbers, in which heat produced by x-ray photons have to be transferred to the thermometer as soon as possible.

In solids, heat is transported by both phonons and electrons, therefore, the thermal conductivity k will be the sum of two contributions [71, 74]:

$$k = k_{ph} + k_e \tag{1.22}$$

The electron term is the most important for pure metals, whatever the temperature is, and it's expressed by:

$$k_e = \frac{1}{3}\frac{c_e}{V_m} v_F l_e \tag{1.23}$$

where:

c_e is the free electrons specific heat contribution;
v_F is the Fermi velocity;
l_e is the mean free path of electrons;
V_m is the molar volume.

The Fermi velocity is:

$$v_F = \sqrt{\frac{2E_F}{m_e}} \tag{1.24}$$

and the mean free path of electrons is $l_e = v_F \tau$, with τ the mean collision time of electrons.

The phonon contribution at low temperatures is negligible in pure metals [75], therefore, at very low temperatures (T ~ few degrees Kelvin), according to (1.19), (1.22), and (1.23) the thermal conductivity is proportional to T (τ is nearly constant at such temperatures).

Superconductor materials have a different behavior depending on their state [71]. If $T > T_c$ the metal is in normal state, and k is proportional to T; in the superconducting regime, k is proportional to T^3 and is much smaller with respect to the normal conduction state. Several values of thermal conductivity for different materials at low temperature are reported in [76, 77].

1.2.2 The thermometer

The temperature increase of the absorber is measured by the thermometer. In the case of NTD-Ge thermistor, a suitable electric circuit reads out the resistance variation associated to its heating.

The semiconductor is doped just below the so called metal-insulator transition (MIT), at which the material behavior changes from insulating to metallic [78]; this means there is conduction also at $T = 0$ K, due to the electric transport in the doping atom (impurities) band deriving from the overlap among electron wavefunctions. The net doping concentration for this transition is the critical concentration N_c, that depends on the semiconductor and its compensation ratio K (1.8).

At cryogenic temperatures ($T \ll 10$ K), when the thermal energy $k_B T$ is less than the energy difference between adjacent localized states, for near MIT doped (concentration $N \lesssim N_c$) or low purity semiconductors, the electric conduction happens according to the variable range hopping (VRH) with Coulomb gap (CG) regime [79, 80, 81, 82] inside the hot electron model (HEM) [83, 84].

The VRH theory was firstly formulated by Mott [85], that didn't consider the electron-electron interaction in the critical regime, and successively modified by Shklovskii and Efros [86], that included the Coulomb interactions with pair sites.

In VRH, conduction electrons, by interacting with the lattice, receive by phonons the needed thermal activation energy to move by hopping, a quantum tunneling effect, from a site to another. Hopping is more probable towards sites, not necessarily the nearest neighbors, whose energies are within a narrow band around the Fermi level. In VRH the mean hopping distance can be much longer than the mean impurity spacing.

In his theory, Mott assumed a constant density of states g around the Fermi level. An electron will attempt to perform hopping at the minimum distance r and with the lowest activation energy Δ_{hop}; in polarization absence, it results:

$$P \propto e^{-\left(\frac{2r}{\xi_0} + \frac{\Delta_{hop}}{k_B T}\right)} \tag{1.25}$$

in which $\xi_0$is the localization length; the hopping probability P will be maximum at the optimum distance r^*.

The electric conductivity is proportional to P. By calculating the hopping bandwidth and using (1.25), Mott deduced the semiconductor resistivity relation (Mott's law):

$$\rho = \rho_0 e^{\left(\frac{T_0}{T}\right)^{\frac{1}{4}}} \tag{1.26}$$

where:

T is the absolute temperature;
ρ_0, T_0 are parameters depending on thermometer dimensions and doping level.

T_0 is called Mott's characteristic temperature. The average hopping length is:

$$\lambda = \xi_0 \left(\frac{T_0}{T}\right)^{\frac{1}{4}} \tag{1.27}$$

At very low temperatures, Mott's law didn't reproduce experimental data. Pollack [87] hypothesized that the density of states at energies E_s near the Fermi level reduces according to:

$$g = g(E_s, E_F)^m \tag{1.28}$$

with m an integer ≥ 0, thus modifying the Mott's law:

$$\rho = \rho_0 e^{\left(\frac{T_0}{T}\right)^{r}} \tag{1.29}$$

where

$$r = \frac{m+1}{m+4} \tag{1.30}$$

If $m = 0$ the Mott's law it's obtained.

Shklovskii and Efros [88] set $m = 2$ implying the modified Mott's law equal to:

$$\rho = \rho_0 e^{\left(\frac{T_0}{T}\right)^{\frac{1}{2}}} \tag{1.31}$$

In this case, the energy gap in the density of states at the Fermi level is named Coulomb gap [87, 88]. A more general expression for semiconductor resistivity ρ in the VRH regime, derived by numerous further studies [88, 89, 90], is given by:

$$\rho = \rho_0 T^q e^{\left(\frac{T_0}{T}\right)^{p}} \tag{1.32}$$

in which q and p are constants taking specific values in different conditions.

In the hypothesis of the parabolic shape Coulomb gap in the density of states near the Fermi energy [89], q=0, and p depends on the hopping model, in particular: p = 1/4 for the Mott model [89], and p = ½ for the Shklovskii and Efros model [88].

For practical NTD Ge microcalorimeters, considering the very low operating temperatures and usual net Ga doping (10^{16} – 10^{17} cm^{-3}), q = 0 and p = ½ can be assumed, and the expression for the resistivity becomes:

$$\rho = \rho_0 e^{\left(\frac{T_0}{T}\right)^{0.5}} \tag{1.33}$$

The exponent p actually depends on the specific NTD Ge crystal used, and best fits of experimental data are sometimes obtained by allowing it to vary [82].

In presence of an applied electric field on the NTD Ge thermistor, the thermometer resistivity deviates from the model (1.33). The discrepancy can be explained by including the hot electron model. This model assumes that, at very low temperatures, the thermal coupling between electrons is stronger than the electron-lattice one; this is because, at cryogenic temperatures, the number of phonons that are able to interact with electrons depends on available states for both phonons and electrons, and electron state number reduces with the temperature.

At very low temperatures electrons can interact so weakly with the lattice that temperature exchange is very small; heat diffuses among electrons more rapidly than in the lattice, and the former temperature becomes higher than the lattice one.

So, the thermometer can be modeled as two different systems, the electronic one and the lattice system, connected by the thermal conductivity $G_{e,l}$ (Figure 1.1).

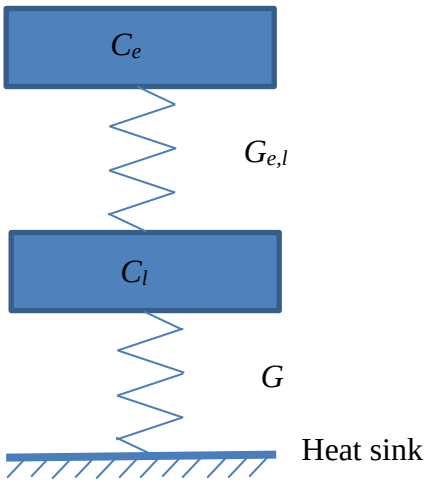

Figure 1.1 - Thermal model of a semiconductor thermistor in the hot electron model.

In Figure 1.1, C_e and C_l indicate the heat capacities of electrons and lattice, respectively; G is the thermal conductivity between the lattice and the heat sink. The thermal conductivity $G_{e,l}$ between the electrons and the lattice can be expressed as [84]:

$$G_{e,l} = G_{0e,l} T_e^{\beta_e} \tag{1.34}$$

where:

T_e is the electron temperature;
$G_{0e,l}$, β_e are constants depending on the specific device.

When the semiconductor is inserted in an electric circuit (Figure 1.2), we can assume that the electric bias power P is initially transferred to the electrons and then to the lattice through the heat link between the two systems:

$$G_{e,l} = \frac{dP}{dT_e} \tag{1.35}$$

In equilibrium conditions, in which only P is applied and there is no external signal input (phonons from the absorber), by substituting (1.34) in (1.35) and solving, we get:

$$T_e^{\beta_e+1} - T_l^{\beta_e+1} = \frac{\beta_e+1}{G_{0e,l}} P \tag{1.36}$$

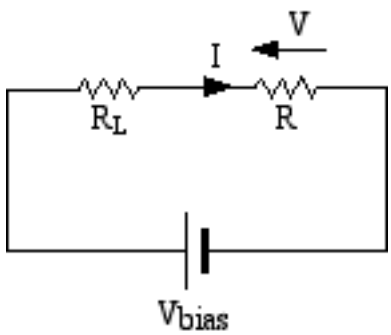

Figure 1.2 - Bias circuit for the microcalorimeter thermometer.

in which T_l is the lattice temperature, and P depends on T_e through the resistance of the thermistor.

The thermal conductance G between the lattice and the cold bath can also be expressed as:

$$G = G_0 T_l^{\beta} \tag{1.37}$$

in which G_0 and β are constants. The inverse of G, that is the thermal resistance between the thermistor lattice and the heat sink, is called Kapitza resistance R_k [91]:

$$R_k = \frac{1}{G} = \frac{1}{G_0 T_l^{\beta}} \tag{1.38}$$

By developing the same procedure as for (1.36), for T_l holds:

$$\left(T_l^{\beta+1} - T_s^{\beta+1}\right) = \frac{\beta+1}{G_0} P \tag{1.39}$$

in which T_s is the heat sink temperature.

By (1.36) and (1.39) both electrons and lattice equilibrium temperatures can be calculated.

If external heat signals are applied (e.g. detection of a photon by the absorber and associated heat transfer to the thermistor), the thermometer temperature changes, and the bias power too (Figure 1.2), in fact:

$$P = R(T_e)I^2 = \frac{V^2}{R(T_e)} \tag{1.40}$$

where:

$R(T_e)$ is the thermometer resistance, related to the electron temperature;
I is the bias current;
V is the bias voltage.

An important parameter for thermometers is the sensitivity, that is defined as:

$$\alpha \equiv \frac{T}{R}\frac{dR}{dT} \tag{1.41}$$

and expresses how the system responds to temperature change.

The bias power change ΔP due to thermometer heating is well described through the electrothermal feedback (ETF). By solving the circuit in Figure 1.2, and by using (1.41), the expression for ΔP can be written:

$$\Delta P = -\frac{P}{T_e}\frac{R-R_L}{R+R_L}\alpha\Delta T_e \tag{1.42}$$

it's worth to be noted ΔP depends on $R(T_e)$ and ΔT_e.

By defining the electrothermal feedback thermal conductivity:

$$G_{ETF} \equiv \frac{P}{T_e}\frac{R-R_L}{R+R_L}\alpha \tag{1.43}$$

from (1.42) we can write:

$$\Delta P = -G_{ETF}\Delta T_e \tag{1.44}$$

Let's now consider the almost ideal case in which the absorber is in so tight contact with the thermometer that the thermal resistance between them is negligible.

When external heat signals arrive from the absorber, the thermometer lattice temperature increases by ΔT_l; in the most general case, i.e. when the electron heat capacity C_e can't be neglected, solving system equations to evaluate both electron and lattice temperature increases ΔT_e and ΔT_l with respect to the equilibrium condition become [84]:

$$C_e\frac{d(\Delta T_e)}{dT} + G_{e,l}(T_e)\Delta T_e = G_{e,l}(T_l)\Delta T_l - G_{ETF}\Delta T_e \tag{1.45}$$

$$C_l \frac{d(\Delta T_l)}{dT} + G\Delta T_l = W + G_{e,l}(T_e)\Delta T_e - G_{e,l}(T_l)\Delta T_l \tag{1.46}$$

in (1.46) W represents the external signal power.

If there is a finite thermal conductance G_a between the absorber (with heat capacity C_a) and the thermometer, and we can assume that the absorber transfers its heat to the thermometer lattice, the related thermal model schematic is reported in Figure 1.3. The correspondent analytical study is developed in [84].

By measurements performed by several researchers on NTD Ge, the electron-lattice decoupling becomes relevant, depending on doping, at temperatures below about 30 mK [92], and in equation (1.34) we have $\beta_e \approx 5$ [93]. In the temperature range 30 – 40 mK the Kapitza thermal resistance is more relevant with respect to the electron-phonon one; at temperatures below 30 mK both thermal resistances are of the same order of magnitude [94].

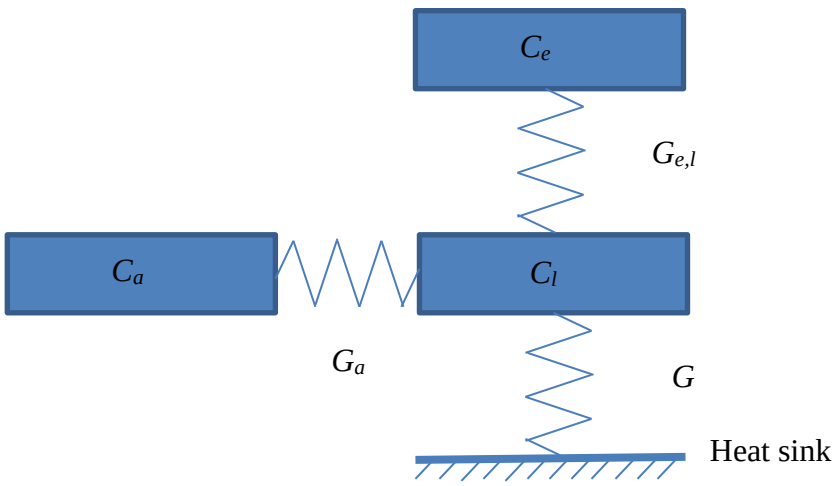

Figure 1.3 - Thermal model schematic with finite thermal conductance G_a between the absorber and the thermometer.

Energy resolution

The microcalorimeter energy resolution ΔE_{FWHM} is limited by the thermodynamic noise [48, 95]. The phonon average energy at the temperature T_0 is:

$$E_{ph} = k_B T_0 \tag{1.47}$$

and the system energy is:

$$E = C_{tot} T_0 \tag{1.48}$$

Then, the phonon number N results:

$$N = \frac{E}{E_{ph}} = \frac{C_{tot}}{k_B} \tag{1.49}$$

By assuming phonons obey the Poisson's distribution, and introducing the Fano factor F ($0< F<1$) to include possible correlation effects among different energy fluctuation causes, the energy resolution ΔE_{FWHM} is expressed by:

$$\Delta E_{FWHM} \cong 2.36\, E\sqrt{\frac{F}{N}} \tag{1.50}$$

By substituting (1.49) in (1.50) and rearranging factors we obtain:

$$\Delta E_{FWHM} \cong 2.36\, \xi\sqrt{k_B T_0^2 C_{tot}} \tag{1.51}$$

where ξ, with a value of the order of one, depends on the microcalorimeter structure; for practical purposes it can be approximated to the unit.

In cryogenic microcalorimeters featuring few tens eV energy resolution, both Johnson and 1/F noises can be neglected [95]. The photon shot noise due to IR radiation from hot surfaces in the cryogenic system is also considered negligible since thermal filters are designed to properly minimize it.

1.2.3 The weak thermal link

In microcalorimeters, it's necessary to allow thermometer heat disposal after the detection of a signal, in order to allow the detector to be prompt to detect another thermal pulse. This is accomplished by connecting the detector to a heat sink via a weak thermal link represented by the thermal conductance G in Figure 1.3. The heat sink is a system with a large (compared to the rest of the microcalorimeter) heat capacity kept at a constant temperature T_{sink} (in present microcalorimeters below 100 mK). The thermal link has to be weak enough to decouple the thermometer from the heat sink and to let the former reach its maximum temperature when an external signal is detected, but, on the other hand, it has to allow the thermometer to recover its reference state in unperturbed conditions in a reasonable time.

The complete thermal model including the weak thermal link is constituted by (1.45) and (1.46). The time constant for the heat transfer is:

$$\tau = \frac{C_{tot}}{G} \tag{1.52}$$

Typical G and τ values for practical microcalorimeters are in the order of 1 nW/K, and 1 ms, respectively [48].

The weak thermal link in NTD Ge microcalorimeters can be implemented by different technical solutions. One consists in placing the thermometer on a thin substrate that is in touch with the heat sink on a reduced area [96]; this method can require both microlithographic and microfabrication processes. The contact surface and interface define the thermal link conductance.

A simpler implementation of this technique is to glue the thermometer directly to the thermal sink [97]. The thermal conductance value is given by the glue thickness, area and thermal conductivity.

Another technique uses metallic, usually aluminum, wires glued by epoxy resin to the thermometer to provide the thermal conductivity towards the cold bath; in this case the wire number, length and transverse section set the thermal conductance.

1.3 Array readout

The direct readout of single pixels in M x N arrays is not a practical solution due to the M x N signal wires and associated readout circuits required to acquire independent pixel output signals. According to the modern technological trend, at high pixel numbers (about 1000 or more [98]) this approach would complicate very much the array structure with serious fabrication difficulties, would increase the heat load, and severely lift the fabrication costs.

Multiplexing is the solution to this problem; according to its definition, it consists in the sharing of the same transmission channel among different devices.

Different multiplexing techniques can be applied for the NTD Ge microcalorimeter array readout; the most mature and widely deployed one also for TESs microcalorimeters [99] is time division multiplexing (TDM), in which each pixel is read by applying a reading signal during a time slot, equal for each pixel; the whole array has to be scanned at a reading signal rate able to guarantee that each x-ray signal pulse is sampled a large number of times over its duration. In very large arrays the TDM reading is executed, e.g., by rows, while columns are read in parallel by using as many complete reading channels as many pixels are in a column [99].

Another multiplexing solution (called Hydra) was developed for the NASA's Constellation-X mission [100]; this technique allows to increase the focal plane pixel number without increasing the number of temperature sensors (TES in this case) and associated power and signal wires. In fact, the whole array is divided in groups of N pixels, one of which is a complete device (absorber and thermometer), while the others consist only of the absorbers, each of them connected to the thermometer of the first pixel by different length metal (Au) paths and thus different thermal conductance to the heat sink. With this structure, different current pulse shapes are generated by the TES when x-ray photons hit different pixels in the group. This allows to identify the photon arrival position. This technique is very demanding in design, and implies relevant fabrication difficulties.

1.4 Present device performances

The over 30-years research on NTD Ge x-ray microcalorimeters allowed to achieve the design and fabrication of very performing devices, mainly, but not only, for astrophysics applications.

Starting from the early devices [101] up to now, the energy resolution gained more than one order of magnitude, and detectors passed from single sensors to arrays to perform imaging.

Single pixel microcalorimeters with tin absorber fabricated by E. Silver et al. [47] featuring 3.1 eV FWHM energy resolution @ 6 keV have to be mentioned. Similarly, an energy resolution of about 50 eV FWHM was measured at energy as high as 60 keV [49, 102]. According to these authors, the measured energy resolution was limited by noise in the readout electronics, and the intrinsic capability of that device could have been 30 eV at the same energy.

Bidimensional NTD-Ge microcalorimeter array prototypes were built by mechanically stacking linear arrays, each supported by flying wires, that bring electric signals and constitute the weak thermal link to a sapphire substrate connected to the refrigerator cold plate [45]. This approach was also proposed for demanding applications, as the Constellation X focal plane [103].

More recently, a full planar technology for bidimensional NTD Ge sensor array fabrication was proposed, in which all pixels were contemporarily produced on the same substrate by applying well established microelectronic planar technology steps [6].

As a further example, an array of NTD Ge microcalorimeters was fabricated for X-ray spectroscopy applications [104]. Each of the 16 pixels in the array consisted of an NTD Ge thermistor

glued to a 300 x 300 x 7 (thickness) μm^3 tin absorber. The device had 2.5 ÷ 6 eV resolution in the energy range 0.2 ÷ 10 keV. The whole spectroscopic system was also composed by the thermoionic electron source and an X-ray optics.

Table 1.3 summarizes the state of the art of NTD Ge microcalorimeters.

Table 1.3 - State of the art of NTD Ge microcalorimeters

Type	Resolution	Reference
Single pixel	3.1 eV @ 6 keV	[47]
Single pixel	50 eV @ 60 keV	[49, 102]
Array (16 pixels)	2.5 ÷ 6 eV @ 0.2 ÷ 10 keV	[104]

1.5 Main applications

NTD Ge microcalorimeters have been investigated for several research applications including: high energy astrophysics (balloon-borne and satellite-borne mission concepts), laboratory x-ray micro-analysis, and particle physics, in particular for the neutrino mass determination and the dark matter search.

In the previous par. 1.3 some examples were provided for the developments related to potential applications of NTD-Ge microcalorimeters in high energy astrophysics ([105, 106, 107, 108, 109]), and laboratory micro-analysis [104]. In the following paragraphs the use of NTD Ge microcalorimeters in particle physics will be addressed.

1.5.1 Neutrino mass determination

The electron neutrino (indicated with the symbol ν_e), more simply called neutrino, is a neutral lepton, that is a subatomic elementary particle, without electric charge and with spin equal to ½. It was firstly theorized by Wolfang Pauli in 1930 to explain the missing energy and momentum in the beta decay, and successively it was discovered by Clyde Cowan and Frederick Reines in 1956 [110].

In 1998 neutrino oscillations (flavor change) were discovered [111], and this stated almost two of the three neutrino flavors (electron, muon and tau) have non-zero mass, whose measurement is a very challenging experiment [112].

A very promising technique for the neutrino mass evaluation, together its other properties, is the neutrino-less double beta decay (DBD) [113]; in fact, by evaluating the neutrino-less DBD life time, the neutrino effective mass $\langle m_\nu \rangle$ can be calculated and, from this, the absolute mass.

The DBD [114] is a nuclear phenomenon for which, in a nucleus, two neutrons emit two electrons; this reaction can be expressed as:

$$ {}^{A}_{z}N \quad = {}_{z+2}^{A}N \quad + 2\beta \tag{1.53} $$

This reaction can be developed either with the emission of two neutrinos (indicated by 2νββ) or without neutrino emission; in this case the phenomenon is said neutrino-less double beta decay and it's indicated by 0νββ.

The DBD can verify if one of the following conditions are fulfilled:

- the single decay isn't energetically allowed;
- the single decay is energetically allowed but strongly inhibited by a large associated spin change needed; in this case, the DBD is more probable

Only elements with an even number of protons and neutrons can develop the DBD. Several experiments were performed with different isotopes, by using scintillation or ionization detectors, with poor energy resolution (4 ÷ 8 keV @ 2 ÷ 2.5 MeV) [115, 116]. The most precise measurement previously obtained for the effective neutrino mass is 0.44 eV [116].

In order to upgrade results on neutrino mass evaluation, a large experiment, named Cryogenic Underground Observatory for Rare Events (CUORE) was implemented. It's located at Laboratori Nazionali del Gran Sasso of the Istituto Nazionale di Fisica Nucleare (INFN), underground laboratories built under the Gran Sasso's massif (near the city of L'Aquila, Italy).

The CUORE detector consists of 988 TeO_2 bolometers, having a total mass of 741 kg, structured in 19 towers, each of them composed by 4 columns, arranged in cylindrical configuration; each bolometer is made by a 5 x 5 x 5 cm^3 TeO_2 crystal glued to an NTD Ge thermistor [117].

The deployed nuclear reaction is:

$$ {}^{130}_{52}Te \quad = {}^{130}_{54}Xe \quad + 2\beta \tag{1.54} $$

The main advantages of this experiment with respect to previous ones are [96]:

${}^{130}_{52}Te$ has 34.5% abundance in natural Te thus increasing the experiment sensitivity;
very low operation temperature (10 mK);
high energy resolution due to NTD Ge thermistors ($\Delta E_{FWHM} = 7.7$ keV @ 2615 keV) [118].

The experiment construction was completed in August 2016 and first data were acquired in spring 2017. The full experiment CUORE was preceded by two smaller experiments, for testing purposes:

- CUORICINO, a system built with the same CUORE technology (5 x 5 x 5 cm^3 TeO_2 crystal with a NTD Ge sensors glued to absorbers), but consisting of only 62 bolometers placed in one tower only; the total mass was 40.8 kg. CUORICINO acquired data from 2003 to 2008 [119].

CUORE-0, derived by CUORICINO, using the same structure implemented for it, but after an improvement in the detector fabrication processes; CUORE-0, with a ΔE_{FWHM}=4.9 keV @ 2615 keV resolution, operated from March 2013 to March 2015 [120].

1.5.2 Dark matter search

According to most recent theories, the Universe is composed by about 27% dark matter (DM), that is non-baryonic, and possibly made of particles like axions or weakly interacting massive particles (WIMPS) [121].

The dark matter search is, presently, a very attracting research field in physics, in particular oriented towards particles with masses around some GeV/c^2. DM particles interact with normal matter and loose energy, so they can be detected by ionization, scintillation, semiconductor devices, but it is necessary to employ sensors with some tens eV sensitivity. Cryogenic microcalorimeters are most suitable detectors, and in particular NTD Ge sensors can be advantageously applied.

A DM detection system was developed inside the EDELWEISS collaboration [122]. It's composed by a high purity Ge crystal, weighting 33.4 g, on which a 2 x 2 x 0.5 mm^3 NTD Ge thermometer is glued; the weak thermal link is obtained by gold wires connecting the thermometer to the detector copper housing. The detector operates at 17 mK inside a dry dilution cryostat, and the detector energy resolution is 17.7 eV, well below the requested threshold.

Chapter 2

ABSORBER DESIGN FOR HIGH ENERGY NTD-GE MICROCALORIMETERS

2.1 Absorbers design methodology

Energy band, energy resolution, and quantum efficiency are the basic parameters defining the microcalorimeter performances. In addition, the use of arrays allows for imaging capabilities at the focal plane of an x-ray astrophysica telescope, whose resolution and field of view depend on the pixel size, and number of pixels, respectively.

The construction of high performance large format NTD-Ge microcalorimer arrays can strongly benefit from the use of well consolidated planar microelectronics technology allowing to obtain multiple devices with almost equal performances due to parallel development of each process for all units in the same substrate. This implies more uniformity, less dimensional tolerances (almost equal adhesion between absorber and thermometer), reduced fabrication times and lower costs for complete devices compared to one-by-one processed devices. On the contrary, by using previously employed micro fabrication techniques, where microcalorimeter arrays are built by assembling discrete detectors, absorbers constituted by thin foils are manually glued to the respective thermometer, with hardly predictable and reproducible sensor performances.

In this framework, the main goal of this research activity is the deployment of microlithographic thick film deposition processes for the fabrication of absorbers for a prototype NTD-Ge hard x-ray microcalorimeter detector ($20 \leq E \leq 100$ keV) for space applications.

A careful design is preliminarily needed, based on suitable specifications. In this activity, the design parameters of hard x-ray NTD Ge microcalorimeter arrays have been derived by both a past proposed mission B-MINE [106], and a balloon-borne experiment concept (MISTER-X) for the observation of hard x-ray emission from the solar corona. In particular, the following parameters have been preliminarily defined:

1) energy band;
2) energy resolution;
3) quantum efficiency *QE*;
4) pixel size;
5) array size and fill factor;

<u>Energy band</u>

The energy band of the absorber will be $20 \leq E \leq 80$ keV to cover with high spectral resolution an unexplored energy region in Astrophysics. The low energy threshold is driven by the spectrum accessible with experiments flying on stratospheric balloon, while the high energy threshold is driven by technical limitations in focusing x-rays by grazing incidence. This energy range, in particular, would allow to record hard x-ray emission from the solar corona as proposed in the MISTER-X experiment concept previously discussed.

Energy resolution

In order to maximize the science return in the observation of the hard components of the solar corona, as needed by MISTER-X, and to get significantly better performances with respect to presently existing hard x-ray detectors for Astrophysics, the goal energy resolution was set to $\Delta E_{FWHM} = 40$ eV @ 60 keV.

Quantum efficiency (QE)

The scientific goal to detect hard x-ray features from the solar corona determines a requirement of $QE > 0.3$ at 60 keV for each single pixel in the array while a lower value can be accepted at higher energies. This *QE* value, quite similar to B-MINE specifications, has been identified as a good compromise with the requirement on energy resolution (the higher the mass the higher the thermal capacity is and the lower the energy resolution).

Pixel size, array size

The pixel size, number of pixels and fill factor needed for the MISTER-X concept has to guarantee a partial coverage of the solar corona. In this activity, we decided to fabricate only a prototype of 4 x 4 absorbers array to develop the technology. Once the fabrication process has been developed and optimized it should be possible to scale to a larger number of pixels.

Array fill factor

In microcalorimeter arrays fabrication, gaps between side pixels have to be minimized to avoid photon detection losses. Due to limitations in the technological processes, a suitable gap between neighbor pixels is needed to avoid thermal shorts, thus the effective area S_a will be less than the total detector area S_{tot}, and the fill factor can be defined as $F_f = S_a/S_{tot}$. To avoid strong reduction in the whole microcalorimeter *QE* we set a requirement of $F_f \geq 80\%$.

Preliminary absorber design specifications are reported in Table 2.1.

Table 2.1 - Preliminary absorber design specifications

Energy band	$20 \leq E \leq 100$ keV
ΔE_{FWHM}	40 eV
QE	0.3 @ 60 keV
Pixel number	4 x 4
F_f	$\geq 80\%$

2.2 Material choice

According to the requirements on energy band and quantum efficiency, only high *Z* materials can be used for absorber fabrication, in fact, the use of light materials would require very large thicknesses (hundreds of microns or more), very difficult to fabricate by planar technologies.

To identify the best absorber material a detailed analysis was preliminarily performed by comparing x-ray absorption characteristics of several materials [123, 124, 125, 126, 127]: bismuth (Bi), tantalum (Ta), tin (Sn), osmium (Os).

As discussed in section 1.2.1, the attenuation law for a monoenergetic photon beam traversing a layer of matter is expressed by:

$$\frac{I}{I_0} = exp\left(-\frac{\mu}{\rho}\rho t\right) = exp(-\mu t) \tag{2.1}$$

Then the quantum efficiency QE can be expressed by:

$$QE = 1 - exp(-\mu t). \tag{2.2}$$

The layer thickness needed to obtain an assigned quantum efficiency can be calculated by:

$$t = \frac{1}{\mu} ln \frac{1}{1-QE} \tag{2.3}$$

By using values from the NIST standard reference database #126 [127], x-ray absorption characteristics for bismuth, tantalum, tin and osmium were evaluated. Figure 2.1 shows the quantum efficiencies for photon energies up to 110 keV of a layer 20 μm thick of the above mentioned absorbing materials. Figure 2.2 shows the layer thickness needed to obtain a *QE* = 0.3 for the same materials.

From Figure 2.1 and Figure 2.2, osmium appears the most advantageous material in terms of QE, however, with such material it's very hard to obtain layers of a few microns thickness [128].

At the high side of the energy band (90 – 100 keV), the required thickness of Tin to obtain QE = 03 would be > 200 μm which would be hard to produce by deposition processes, according to the planar technology.

Pure rhenium is also difficult to deposit, due to low process efficiency and poor coating quality [129], furthermore, it is a very expensive material.

Gold has also been investigated as absorber material [130], however, being a normal metal, the heat capacity at low temperature is very high (C_{gold} = 7.14 J/K·m^3 @ 0.1 K) implying that high energy resolution cannot be achieved when a few microns pixel thickness is needed to get high QE.

Finally, bismuth and tantalum remained as good candidate materials for absorbers fabrication.

Bismuth was our first choice for the absorber prototype fabrication due to its very low heat capacity, high growth thickness by electroplating, and moderate cost [73, 131, 132].

In Table 2.2 the main physical and chemical bismuth properties are reported [133, 134]. This element belongs to the Va group in the Mendeleev table; it's a brittle, hard and coarsely crystalline solid metal, at room temperature, with rhombohedral crystalline structure; it doesn't tarnish in air at room temperature, and is the most diamagnetic among all metals [134]. Bismuth is enough resistant to acids: it isn't attacked by hydrochloric acid (HCl), only slightly by hot sulfuric acid (H_2SO_4), but it dissolves in either pure or diluted nitric acid (HNO_3).

Figure 2.3 shows theoretical QE curves of bismuth absorbers with different thickness in a wide energy range, based on X-ray absorption data in [135].

Very interesting is the very low bismuth specific heat at cryogenic temperatures, advantageous for microcalorimeter applications (Table 2.2); for comparison that of gold at the same temperature is c_{gold} = 7.14 $J \cdot K^{-1} \cdot m^{-3}$. By calculating the heat capacities for two different absorbers, the first made of bismuth and the other one made of gold, with the same surface area of 100 x 100 μm^2, and the same QE = 0.3 at E = 100 keV we get $C_{bismuth} = 2.38 \cdot 10^{-15}$ $J \cdot K^{-1}$ and $C_{gold} = 2.56 \cdot 10^{-13}$ $J \cdot K^{-}1$. The gold heat capacity is two orders of magnitude greater even if the thickness of gold is lower than that one of Bismuth due to different linear attenuation coefficients, namely t_{gold} = 35.8 μm and $t_{bismuth}$ = 63.8 μm.

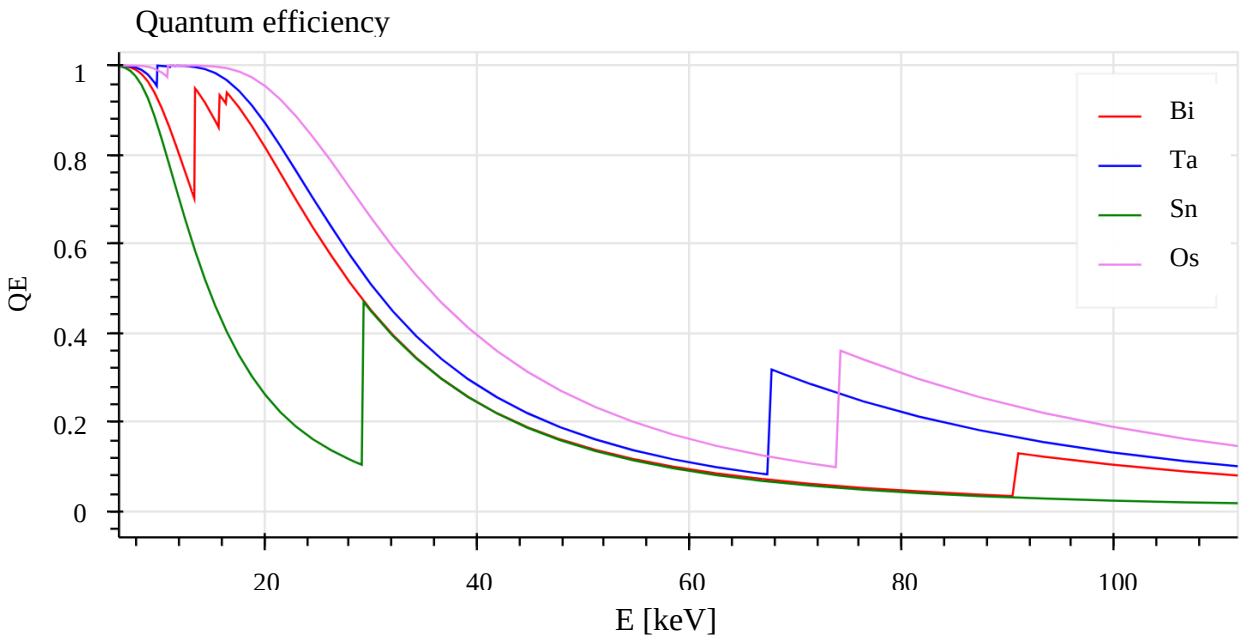

Figure 2.1 - Quantum efficiency as a function of energy for a 20 μm thick layer of different high Z absorbing materials, namely: Bismuth, Tantalum, Tin, and Osmium.

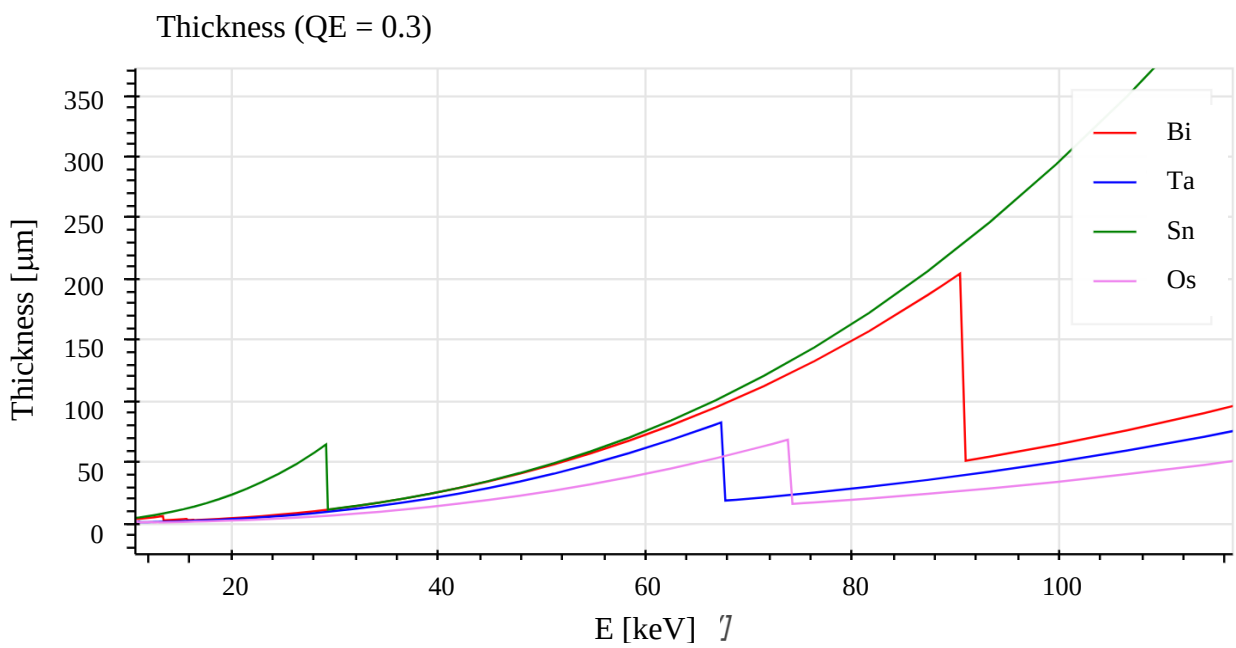

Figure 2.2 - Layer thicknesses needed to get a QE = 0.3 as a function of photon energy, for four different high Z absorbing materials, namely: Bismuth, Tantalum, Tin, and Osmium.

Table 2.2 Main physical and chemical properties of bismuth [133, 134]

Property	Value
Atomic number	83
Atomic weight	208.98
Density	9,747 $g \cdot cm^{-3}$
Melting point	271.3 °C
Boiling point	1560 °C
Oxidation states	-3, +3, +5
Specific heat (T=100 mK)	$3.74 \cdot 10^{-2}$ $J \cdot K^{-1} \cdot m^{-3}$
Heat conductivity (T=100 mK)	$1.32 \cdot 10^{-1}$ $W \cdot K^{-1} \cdot m^{-1}$

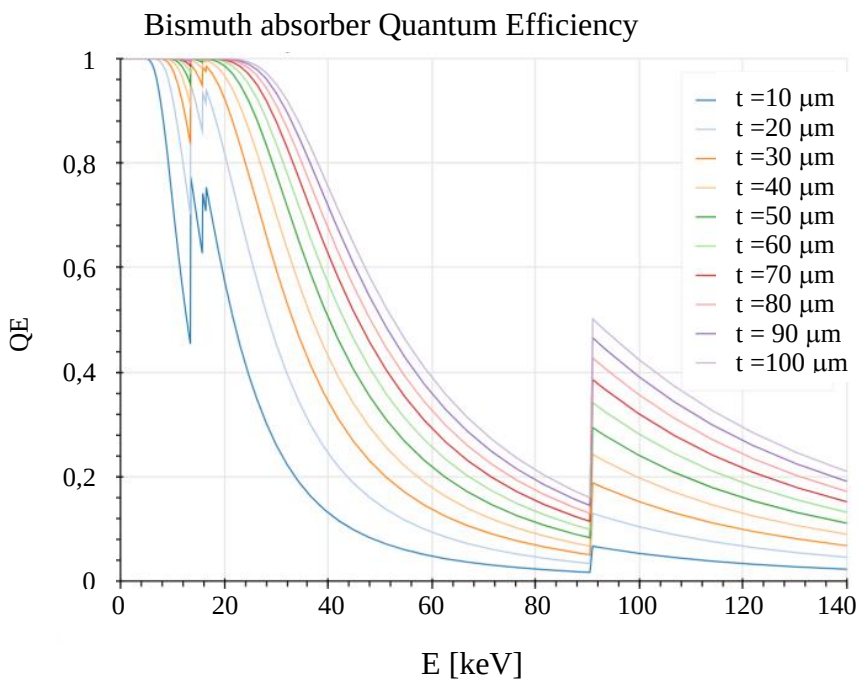

Figure 2.3 - Theoretical QE of bismuth absorbers with different thicknesses.

2.3 Absorber design

Based on previously discussed microcalorimeter requirements, we have to determine the pixel size for the first investigated absorber material, Bismuth. Figure 2.4 shows the adopted decision flow chart.

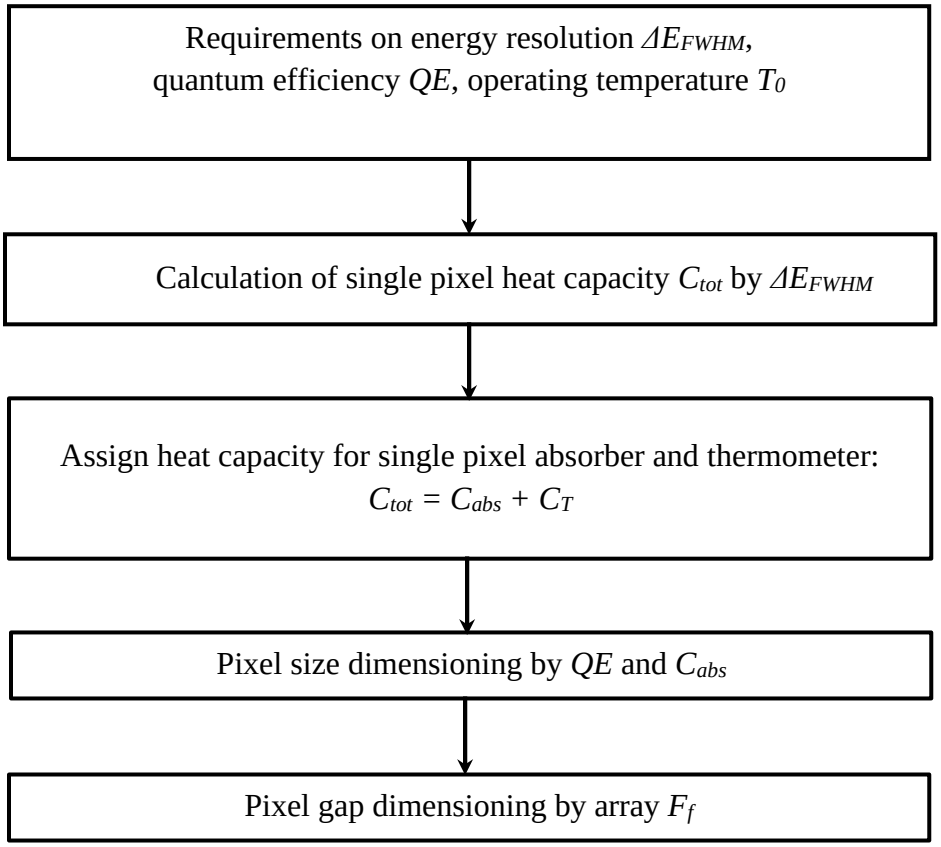

Figure 2.4 - Absorber dimensioning process flow chart.

From the energy resolution requirement ΔE_{FWHM} = 40 eV (6.4e-18 J), by using equation (0.3), that is here reported:

$$\Delta E_{FWHM} \cong 2.355\xi\sqrt{k_B T_0^2 C_{tot}} \tag{2.4}$$

in which the coefficient ξ was set equal to 1, the total maximum heat capacity of the detector (absorber+thermistor) C_{tot} was calculated at the operating temperature T_0 = 50 mK:

$$C_{tot} = \frac{\Delta E_{FWHM}^2}{5.546 k_B T^2} = 2.144 \cdot 10^{-10}\ J/K \tag{2.5}$$

where $k_B = 1.381 \cdot 10^{-23}$ J/K is the Boltzmann constant.

Then, in order to calculate C_{abs}, we have conservatively assumed an equal share of the heat capacity between absorber and thermistor:

$$C_{abs} = 0.5 C_{tot} = 1.072 \cdot 10^{-10}\ \ J/K \tag{2.6}$$

In order to determine the absorber volume V_{abs} from the heat capacity, we need the specific heat:

$$C_{abs} = c \quad d_{abs} V_{abs} \tag{2.7}$$

where:

c is the bismuth specific heat;

$d_{abs} = 9.78$ gcm^{-3} is the bismuth density.

Bismuth is a superconducting metal with a transition temperature $T_C = 5.3 \cdot 10^{-4}$ K, therefore, at the operating temperature of the absorber (T ~ 50 mK) it behaves as a normal metal and the specific heat can be calculated by the Debye – Sommerfeld equation, holding for temperature near 0 K:

$$c_v = \gamma T + \alpha T^3 \tag{2.8}$$

in which the term γT represents the electronic contribution and αT^3 is the lattice contribution. For bismuth at temperature $T \leq 2$ K, the coefficients γ and α take the following values [73]:

$$\gamma = 3.2 \cdot 10^{-7}\ Jg^{-1}K^{-2} \tag{2.9}$$
$$a = 5.66 \cdot 10^{-6}\ Jg^{-1}K^{-4} \tag{2.10}$$

By substituting (2.9) and (2.10) in (2.8) we get: $c = 1.671 \cdot 10^{-8}$ J g^{-1}K^{-1}.

Similarly, the specific heat for NTD Ge at the same temperature can be calculated from data in [92]: $c \sim 52.5 \cdot 10^{-9}$ JK^{-2}cm^{-3}.

The absorber volume can be expressed as:

$$V_{abs} = Sh \tag{2.11}$$

in which S is the surface area of the absorber, and h its thicknessBy requiring a QE = 0.3 @ 60 keV the minimum absorber thickness is h = 60 μm, uming to grow pure crystalline material.

By (2.7) and (2.11), the surface area can now be calculated:

$$S = 1.1 \cdot 10^7\ \mu m^2 \tag{2.12}$$

In a square array, also pixels are squares with side L:

$$L = \sqrt{S} = 3306\ \mu m \tag{2.13}$$

This is the maximum theoretical absorber size to obtain the target energy resolution; but it has to be considered an upper limit, due to:

1) absorber fabrication tolerances related to technological process could make bismuth pixels larger than designed;

2) the 60 μm evaluated thickness could be insufficient to guarantee the requested *QE*, due to imperfections in the grown material; in this case, it would be necessary to increase *h*, and, with the above calculated area, this would raise the heat capacity, reducing the energy resolution;
3) smaller pixels would allow to increase their number for future large format x-ray imaging arrays for astrophysics and laboratory applications.

For these reasons, and considering that the research group of XACT-OAPa and DiFC already fabricated microlithographic masks for the thermometer fabrication with similar pitch sizes, we choose to initially design square pixels with $200 \leq L < 400\ \mu m$. With this choice, the maximum heat capacity of each pixel is:

$$C_{abs} = 1.6 \cdot 10^{-12}\ J/K \tag{2.14}$$

Finally, to satisfy the fill factor requirement, we assumed an array pitch p_a equal to L * 1.1. The resulting fill factor F_f is:

$$F_f = \frac{L^2}{(1.1L)^2} = 0.83 = 83\% \tag{2.15}$$

and the resulting gap between neighbor pixels is: $20 \leq g \leq 40$ μm. Table 2.3 summarizes the design parameters of the first investigated absorber array.

Table 2.3 - Absorber design parameters

Topology	Square pixel 4 x 4 array
Material	Bismuth
Pixel thickness	60 μm
Pixel surface area	200 x 200 to about 400 x 400 μm^2
Pixel gap	20 to 40 μm

Chapter 3

ABSORBER FABRICATION

3.1 Bismuth layer growth techniques

Pure bismuth and bismuth alloy films have presently several applications, such as thermoelectric conversion [136], reference electrode fabrication for heavy metal detection [137] and large magneto-resistance devices [138]. Several techniques are available to deposit bismuth films:

1) Resistive boat physical vapor deposition (PVD) [139];
2) Electron beam PVD [139];
3) DC sputtering [140];
4) RF sputtering [140];
5) Pulsed DC sputtering [141];
6) Pulsed laser deposition [142];
7) Molecular beam epitaxy (MBE) [143];
8) Electroplating [144].

All these techniques produce bismuth layers with different properties, particularly with respect to crystallographic structure and morphology. Techniques 1) to 7), usually characterized by very low deposition rates of few nm/s [145], are best suited for thin film deposition (thickness less than 1 μm) and require complex and expensive equipment.

On the other hand, electroplating is appropriate to grow very thick (tens of microns) bismuth layers in practical times (some hours), and deposited film properties can be controlled by acting on different process parameters.

Since we need to grow thick bismuth layers, electroplating fabrication technology was chosen. Basic principles and technical deployment of such technique will be described in the next paragraph.

3.2 The electroplating process

Electroplating [146] is an electrochemical technology based on the reduction process of metal cations from a suitable solution (electrodeposition bath) to metal.

This process is industrially employed to coat metal elements with another metal with specific physical and chemical characteristics for protective and/or decorative purposes: typical examples are represented by anti-corrosion coatings of mechanical items and by silver or gold plating of jewelry.

The schematic description of such process is depicted in Figure 3.1.

By the application of a suitable electric potential, ions of the plating material travel in the electroplating bath, from an electrode called “anode”, in which the oxidation process takes place, to the receiving electrode, called “cathode”, constituted by the substrate on which the film has to be deposited and on which the reduction process occurs. The metal ions can alternatively be directly drawn from the solution, in which case the anode is inert. The cathode is called working electrode (WE), and the anode is referred to as counter electrode (CE) or auxiliary electrode (AE).

Positive ions going toward the cathode are called cations, and negative ones are said anions.

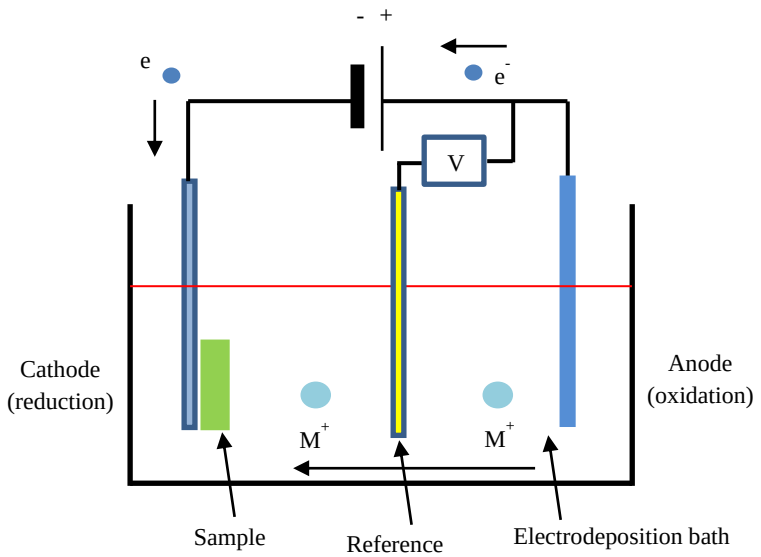

Figure 3.1 - Schematic of the electroplating process.

Cations travel in the electrolytic bath not only due to the electric field generated by the power supply but also by diffusion and convection.

The negatively charged cathode attracts cations by electrostatic forces, forming a narrow positively charged layer, where a strong electrical field is present, in the solution. These two layers (the negative charge in the cathode and the positive one in the bath) are called electric double layer, and its existence was firstly conjectured by Helmholtz in 1850's. In this model [147], however, all the potential drop near the electrode happens within the extension of an ion radius (outer Helmholtz plane, about 5 Å from the cathode surface), and solution ion diffusion, mixing, possibility of surface adsorption, and dipole moment interactions are not considered.

A successive model, developed by Stern, introduced the "outer" or "diffuse" layer, constituted by another negative charge layer, less compact than the previous, electrostatically attracted by the positive part of the double layer toward the cathode; the outer layer extends itself up to about 50 - 100 Å from the cathode surface.

When cations arrive very near the cathode, at about 50 – 100 Å distance, they enter the diffuse layer, then arrive at the double layer, where they are dehydrated, and undergo the electroreduction. In this way adatoms (atoms lying on the surface of crystals) are generated, that diffuse in the cathode surface to originate a new material phase (electro-crystallization) to create nucleation sites and growth for the specie to be electroplated.

Electroplating is based on the two Faraday's laws [148, 149], relating the quantity of matter transported in an electrochemical process with the transferred electrical charge, that can be expressed as follows:

$$Q = \int_0^t i dt \tag{3.1}$$

$$w = \frac{MQ}{96500n} \tag{3.2}$$

in which:
Q: electrical charge in coulombs;
i: current in amperes;
t: time in seconds;
w: material weight;
n: number of transferred electrons per atom;
M: molecular weight of the transported substance.

In (3.2) the Faraday constant 96485,3 (C/mol), usually rounded to 96500, is the electrical charge needed to transfer a mole of substance with oxidation state 1 ($n = 1$).

Generally, during an electrochemical deposition, not all the transferred charge is due to moved atoms, due to concurrent side reactions. The electrical efficiency η_E is expressed as:

$$\eta_E = \frac{Q_M}{Q} = \frac{96500nw}{MQ} \tag{3.3}$$

in which Q_M is the electrical charge related to the main reaction, whilst Q is the total one.

In electrochemical processes, the liquid bath is an ionic conductor and, besides potential drops at electrode/liquid interfaces, the Ohm's law holds, and the voltage drop V across the electrolyte between electrodes is:

$$V = iR \tag{3.4}$$

in which R is the electric resistance of the liquid in which both cation and anion current flow.

In an electrochemical process the directly measurable quantities are the cell voltage, that is the voltage measurable between WE and CE, and the related current.

Another important quantity is the electrode potential, defined as the nearly discontinuous potential difference, not directly measurable, between the electrode surface and the region in the solution adjacent to the electrode itself.

The electrode potential mainly depends on specie molecules interested by the electronic transfer.

After above considerations, the potential distribution in the electrochemical cell can be represented as in Figure 3.2, where x is the space coordinate for the electrode geometry and V represents the electric potential.

Starting from the cathode, the first potential increase (up to E_A) happens when the cathode/solution interface is traversed; then there is an iR ramp, due to the solution resistance, and another step E_B, related to the liquid/anode interface.

To develop well-controlled processes, it is necessary to precisely measure the applied WE-CE current. Moreover, since the deposition reaction is primary governed by the WE potential, a method to measure this quantity is needed; this is obtained by placing in the electrochemical cell a third electrode, the reference electrode (RE). Generally, this is constituted by a metal probe surrounded by a well-known and invariant solution forming a highly reversible electron transfer couple with the probe. This is practically obtained by enclosing the probe and the solution in a glass tube with a small opening at the lower end, in which a porous membrane prevents this liquid from mixing with the electrochemical bath.

The RE is not traversed by the process current, so the RE-WE voltage measurement is not influenced by voltage drops due to this current, and using the knowledge of the RE potential, it is possible to derive the WE potential.

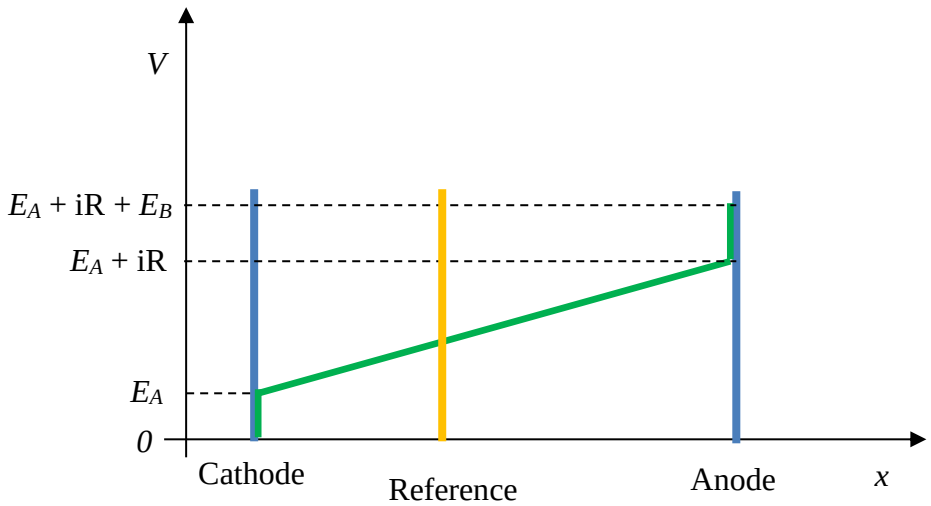

Figure 3.2 - Potential distribution in the electrochemical cell in Figure 3.1

A typical electrodeposition reaction is:

$$M_{1,solut}^{n+} + ne^- \rightarrow M_{dep} \tag{3.5}$$

in which:

$M_{1,soluz}^{n+}$: *n*-valence positive metal ion;
M_{dep}: cathode surface deposited metal atom.

The electrode potential *E* associated with (3.5) in the equilibrium condition, when no current passes, is given, related to the E_o potential (standard redox potential) of a reference electrode, by the Nernst equation:

$$E_{i=0} = E_0 + \frac{RT}{nF} ln[M_1^{n+}] \tag{3.6}$$

in which:
R: universal gas constant;
T: absolute temperature;
F: Faraday's constant;
$[M_1^{n+}]$: metal ion concentration.

The Nernst equation for the complete electrochemical process is:

$$E_{i=0} = E_0 + \frac{RT}{nF} ln \frac{[M_1^{n+}]}{[M_2^{n+}]} \tag{3.7}$$

in which $[M_2^{n+}]$ is the concentration of the anode reaction product.

When the current flows, the electrode potential changes with respect to the equilibrium by an amount η, called activation overvoltage, which depends by the current itself.

By applying an increase ΔE to the electrode potential to the advantage of the reduction reaction, the resulting current is constituted by the cathodic component, due to the reduction process, and the anodic one, given by the oxidation one; both depend exponentially by ΔE.

To implement an electroplating process, a power supply, a voltmeter to measure the WE-RE voltage difference, and a current meter for reading the WE-CE current are required.

Due to the need of very precise process control, more and more sophisticated instrumentations were developed during time.

Presently, electrodeposition processes are developed by using potentiostats, that are high-precision, multi-function (potentiometry, galvanometry, impedance spectroscopy, etc.), multichannel (they can control more than one cell at a time) instruments, in which the voltage difference between the WE and the RE is measured and controlled and the current flowing between the WE and the CE is measured.

3.3 Bismuth electroplating

In order to manufacture thick, high-energy X-ray absorber arrays, it was preliminarily necessary to develop a suitable electroplating process.

Before starting the experimental activity for bismuth electroplating, a wide literature review was performed in order to evaluate and compare various processes with respect to experimental conditions (chemical compound availability, necessary equipment) and obtainable results.

Several electroplating recipes were developed by many research teams to obtain high quality bismuth layers, whose physical characteristics were best suited to different applications. The most interesting processes, representing the current state of the art in bismuth electroplating, are summarized in Table 3.1, that includes the most important parameters related to the referenced experiments.

Among them, n.1 and n.2 were chosen for starting the experimental deposition activities because of the reported properties of the deposited films. The first step to proceed towards the absorber fabrication was the implementation of a suitable bismuth electroplating process, able to produce uniform, compact, high thickness layers (60 μm or more), as requested by the absorber design.

By controlling process parameters (applied electric potential, circulating charge, bath composition, fluid-dynamic conditions, bath temperature), it is possible to tune the properties of the electrodeposited layer such as thickness, composition and morphology. It is noteworthy to mention that the choice of the applied potential, according to thermodynamic equilibria of metal/metal cations in bath solution, is crucial to avoid side reduction processes that are detrimental for both the electrodeposition efficiency and the film quality, in particular in case of hydrogen bubbling.

Several experiments were executed to explore the parameter space (solution pH, deposition voltage, deposition time, bath stirring and temperature); obtained results were compared to define an optimized process.

Table 3.1- Bismuth electroplating recipes.

N.	Bath	pH	Temperature (K)	Current density (mA/cm^2)	Other parameters	Reference
1	$Bi(NO_3)_3 \cdot 5H_2O$ KOH Glycerol Tartaric acid Nitric acid	≈0.6	298	1 – 5	Magnetic stirring. Seed layer thicknesses 20 – 100 nm.	[150]
2	$Bi(NO_3)_3 \cdot 5H_2O$ DMSO	n.a.	298	0.5 – 5	n.a.	[151]
3	$BiOCH_3COO$ EDTA-4Na CH_3COOH CH_3COONa	4.1	298	10 - 100	28 kHz sonicated bath (smoothed and dense films).	[152]
4	$Bi(NO_3)_3 \cdot 5H_2O$ CH_3COONa Acetic acid Nitric acid	n.a.	n.a.	n.a.	Plating potential ≤0.4 V.	[153]

Sample preparation

Electroplating processes were performed using ad-hoc fabricated substrates. Microscope glass slides were cleaved in six samples each, with size 25 x 12.5 x 1 mm^3. They were cleaned using the following procedure, performed in the class 10000 clean room of the INAF-OAPA XACT Laboratory:

1) wash with a mild detergent;
2) rinse with de-ionized water;
3) degrease in trichloroethylene (TCE) with sonication and successive rinsing with TCE;
4) immersion in acetone;
5) wash with DDW (double-distilled water) with a mild detergent;
6) rinse with DDW;
7) final rinse with absolute ethanol;
8) dry with dry nitrogen;

The glass slides were then coated by a double metal layer on their top surface by electron-beam thermal evaporation technique using a Varian VT-114 system, operated inside the same clean room (Figure 3.3: center: evaporation system; right: control rack). A 20 nm layer of titanium was initially deposited, followed by 20 nm of gold to form the final electroplating substrate (Figure 3.4).

A thick, adhesive copper tape was applied on a small area of the gold coating of the substrates to have a robust electric contact to which apply the WE clamp. A narrow, thick Teflon film was wrapped around each substrate to define the deposition area (the one not covered by the Teflon) and to protect the copper tape from the electrodeposition solution.

In order to evaluate suitable deposition potential ranges, 20x10x1 mm^3 fluorine-doped tin oxide (FTO) samples were used, without any additional metal coating; copper tape and Teflon films were applied as described.

Experimental set-up and electroplating solution

The electroplating processes were performed at the Electrochemical Material Science Laboratory of the Dipartimento di Ingegneria of the Università di Palermo. The experimental setup employed to optimize the electroplating process consists of a three electrodes electrochemical cell connected to a Bio-Logic SA potentiostat. The WE is the metallic substrate where the bismuth layer is electrodeposited, an Ag/AgCl with KCl 3M is the reference electrode, and a DSA (dimensionally stable anode) is the CE. The Ag/AgCl reference electrode is constituted by a silver wire, coated with a silver chloride layer, immersed in a potassium chloride solution contained in an ampoule with a porous layer opening, able to allow the contact between the electrode and the bath solution. The electroplating cell is placed on a stirring hot plate.

Figure 3.3 - Varian VT-114 e-beam evaporation system.

Figure 3.4 - Electroplating substrate.

The compositions of electroplating solution n.1 and n.2 (see Table 3.1) are reported in Table 3.2 and Table 3.3.

The first solution requires a very careful preparation; at first glycerol, DDW, tartaric acid and bismuth nitrate pentahydrate are mixed in a suitable beaker, in the above order. Then the nitric acid is added, and the obtained solution is stirred on the hot plate at 25 – 30 °C; the solution is completed with the potassium hydroxide, and it needs some hours stirring at 500 rpm at the same temperature to appear clear and transparent, when is ready to be used. All the reagents are weighted by a laboratory scale with 100 μg accuracy. In this solution the nitric acid is used to dissolve the bismuth salt in water, and potassium hydroxide regulates the solution pH value, as the bismuth deposition happens for $0<pH\leq0.9$. Since pH is very sensitive to both small HNO_3 and KOH quantity variations, and to the environment temperature, it is necessary to check the solution acidity right before starting the electroplating processes and, if necessary, to correct it. The pH measurements were performed by a Hanna laboratory pH-meter.

Table 3.2 - Acid bismuth electroplating solution (n.1) composition.

Bismuth nitrate pentahydrate	$Bi(NO_3)_3 \cdot 5H_2O$	3.75 g	Honeywell Fluka
Potassium hydroxide	KOH	3.81 g	Sigma Aldrich
Nitric acid	HNO_3	5.7 ml	J. T. Baker
Glycerol	$CH_2OHCHOHCH_2OH$	6.25 g	Chem Lab
Tartaric acid	$HOOC\ (CHOH)_2\ COOH$	2.5 g	Chem Lab
DDW	H_2O	50 ml	---

Table 3.3 - Bismuth electroplating solution composition containing DMSO (n.2).

Bismuth nitrate pentahydrate	$Bi(NO_3)_3 \cdot 5H_2O$	2.5 g	Honeywell Fluka
Dimethyl sulphoxide (DMSO)	$(CH_3)_2SO$	55 g	Sigma Aldrich

The solution n.2, is otherwise very easy to prepare, and no pH control is needed; stirring is performed at about 500 rpm at room temperature for 1 – 2 hours.

<u>Preliminary deposition experiments</u>

a) Electroplating with solution n.1

To start the experimental study of bismuth electroplating with the solution n.1 (Table 3.2), the suitable electrode potential range according to the thermodynamic stability region of bismuth in aqueous solution was firstly evaluated by the Pourbaix diagram [154] and then investigated by cyclic cyclovoltammetry [155].

Pourbaix diagrams plot the stable phases of an aqueous electrochemical system with respect to the electric potential and the solution pH. Different lines in Pourbaix diagrams represent redox and acid-base reactions, and indicate conditions in which two species have equal activities.

Horizontal lines are referred to oxidation of metallic materials, that are independent from the pH; vertical lines represent pure acid-base reactions, that are independent from the potential.

The Pourbaix diagram for bismuth is reported in Figure 3.5. It can be stated that, for pH values reported in Table 3.2, bismuth deposition starts at about 0 V. This can be asserted by considering the curve n. 9 in the diagram for the Bi^{3+} + $3e^-$ reaction at the pH values between 0.1 and 0.6, and evaluating, using the Pourbaix equations in [154], the potential $E_0 = 0.215 + 0.0197 \log[Bi^{3+}]$, in which the concentration $[Bi^{3+}]$ = 75 g/L for the same solution. As previously mentioned, it is important to avoid hydrogen evolution, and this can be obtained by choosing potentials not below the "a" dashed line in the diagram.

Cyclic voltammetry is a potentiodynamic method used in analytical chemistry and industrial processes in order to obtain analytical, thermodynamic, kinetic and mechanistic information about the chemical system under investigation. The WE potential measured with respect to the reference electrode is cyclically scanned in the range from the starting potential to a value called switching potential, and the current flowing between the electrodes is continuously measured. The number of cycles is a process parameter.

A cyclic voltammetry was performed using the same Bio-Logic SA potentiostat, in the same setup already described; an Au coated sample (as described in Sample preparation) was used as WE. The sweep rate was -2 mV/s and the electrode potential was scanned starting from OCP (Open Circuit Potential) towards negative potentials. The lower potential was about -0.1 V with respect to the Ag/AgCl reference electrode, higher with respect to the reduction potential of H^+/H_2 (-0.2 V at this pH), to avoid the hydrogen evolution.

The cyclovoltammetry diagram (Figure 3.6) shows that the cathodic current starts at ~ 0 V: this cathodic current can be related to the reduction of Bi^{3+} to Bi leading to the deposition of bismuth layer on gold substrate. This potential is in agreement with that reported in the Pourbaix diagram.

Several experiments were executed to explore potential range (Figure 3.6), to find the best value allowing smooth and compact layer depositions, to study the growth characteristics of large area bismuth layers (morphology, composition, adherence to the substrate, geometrical features, deposition rate, electrical properties). Explored process parameters are summarized in Table 3.4, including, for comparison purposes, also experiments performed with the n.2 solution.

After the electroplating process, the samples were gently washed in DDW to remove residual acid solution and they were let to dry in ambient air. Heating was avoided to prevent excess surface oxidation.

b) Electroplating experiments with solution n.2

The same procedure used for solution n.1 was followed for solution n.2; in order to identify the best potential range, a cyclovoltammetry was executed with the following parameters:

- sweep rate: 2 mV/s;
- starting potential: -1 V;
- switching potential: +1.5 V
- cycles: 3.

The WE consisted of fluorine doped tin oxide (FTO); the cyclovoltammetry diagram is shown in Figure 3.7.

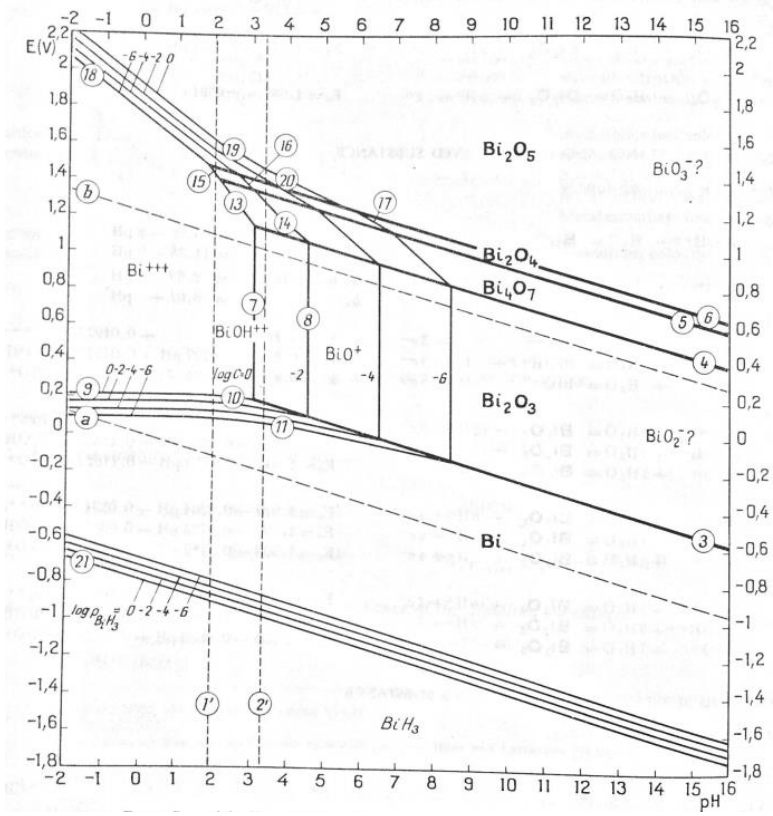

Figure 3.5 - Pourbaix diagram for bismuth [154]

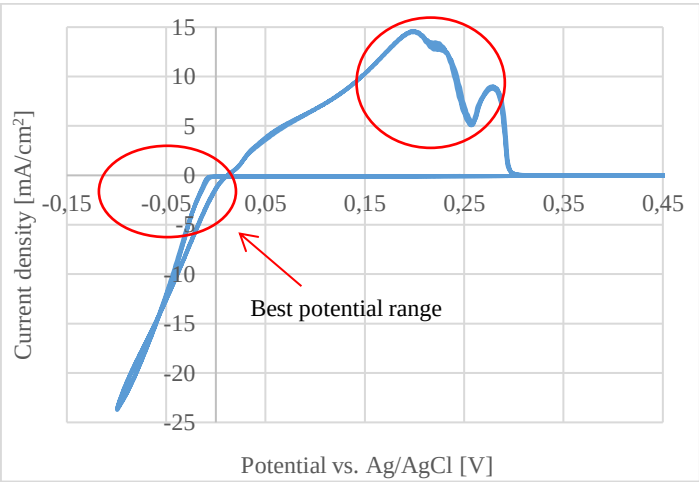

Figure 3.6 - Three cycle cyclovoltammetry diagram for bismuth deposition with the solution n.1.

To deposit bismuth with this solution it was decided to set potentials in the range -0.8÷-0.2 V, for which current starts flowing, allowing the bismuth deposition, and hydrogen development is avoided.

Several experiments were performed with different parameters varying in the ranges shown in Table 3.4; as previously mentioned, a significant difference with respect to solution n.1 was that pH control was not necessary.

Table 3.4 - Summary of continuous bismuth layer growth experiments.

	Solution n. 1	**Solution n. 2**
Electroplating voltage range (V)	-0.2 ÷ -0.02	-0.8 ÷ -0.2
Current density (mA/cm^2)	-21.6 ÷ -4.28	-18.94 ÷ -1.68
pH range	0.05 ÷ 0.26	NO
Deposition time (h:min)	0:30 ÷ 6:00	1:10 ÷ 6:15
Bath heating (°C)	YES/NO	NO
Bath stirring	YES/NO	YES/NO

Some initial simple tests, like optical microscope inspection, scotch test and sample weighting by laboratory scale, were performed to have an immediate evidence of basic deposited layer characteristics, to evaluate the process quality and the suitability for absorber manufacturing.

Grown bismuth films were observed with a Leica MZ12 optical microscope in order to evaluate features like the uniformity of the layer surface, the eventual presence of cracks and other visible defects, and the presence of lateral dendrites.

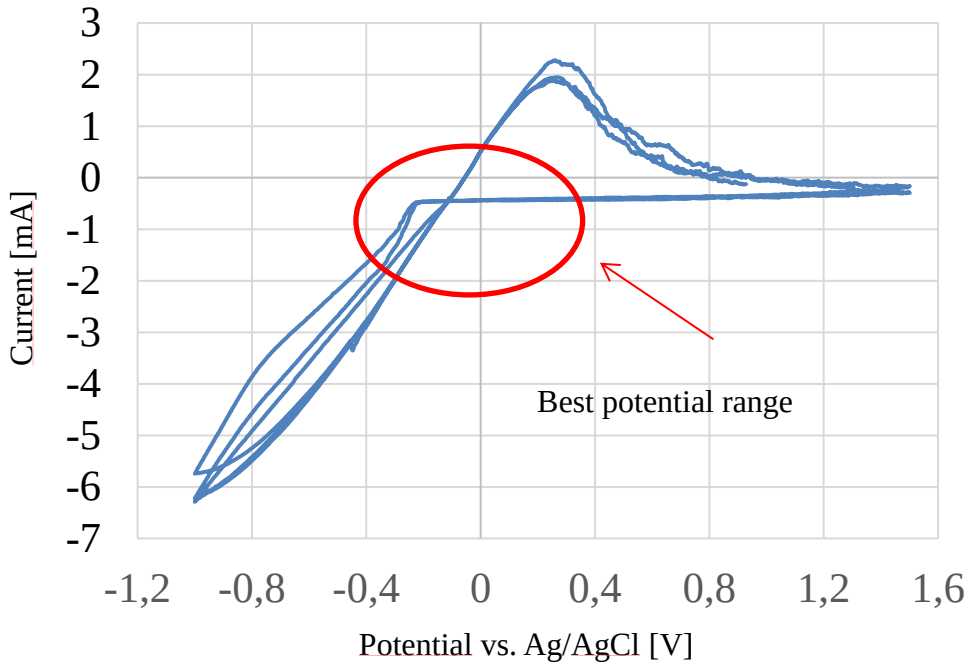

Figure 3.7 - Cyclovoltammetry diagram for the solution n.2.

The scotch test is a very simple method that was adopted to verify the grown bismuth layer adhesion with the substrate gold surface. Bismuth films have also been characterized with respect to their morphological, compositional, electrical properties. This activity will be reported in detail in the next chapter 4.

Comparison between the two recipes

A comparison between morphological properties of bismuth layers deposited using the two solutions were performed to define the best process for x-ray absorber growth.

a) Solution n.1

In Figure 3.8 the comparison between some representative depositions, grown with different E_s, is shown. The deposition time is 30 min and bath was stirred at 300 rpm, without heating.

Used samples, and relative E_s, were: #10-2 (-20 mV) #1K (-50 mV); #1I (-100 mV); #1F (-200 mV).

Two main comments can be done:

- as expected, current densities increase (in module) at greater deposition potentials;
- at fixed voltages E_s, each curve has a small negative derivative, and the absolute value of the current density grows. This is particularly evident for higher potentials.

The increasing step in the E_s =-200 mV curve was due to a sudden vibration of the whole deposition system, that probably caused a temporary displacement of the electrodes; after the system returned in its static condition the deposition current, through a long transition, returned to its regular trend. Constant or slowly decreasing curves indicate a process with a constant deposition rate, suggesting that there has not been material detachment or strong current densities due to irregularly grown structures.

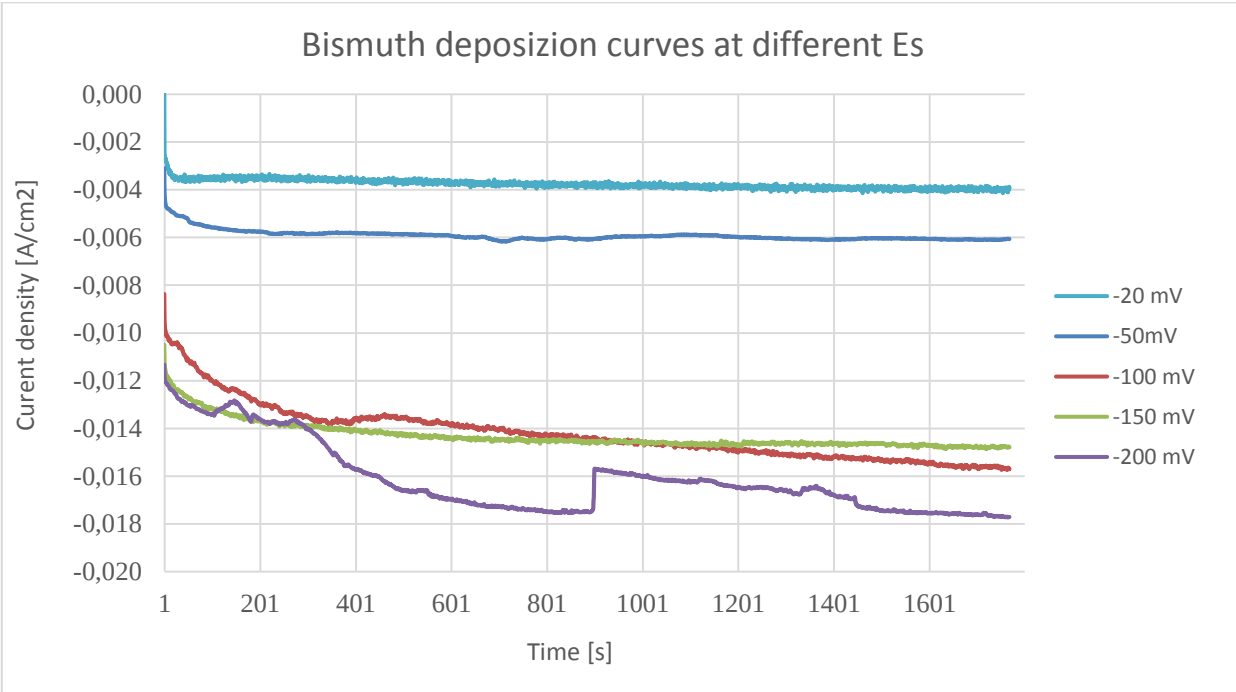

Figure 3.8 - Comparison between different time profile of the current density in electroplating processes performed with solution n.1 for different values of E_s.

In Figure 3.9 the plot of transferred charge per surface unit versus time is shown; of course, charge density is greater for larger E_s is, as it is related to the current density by (3.1).

The deposited thickness z, in the hypothesis that the electric efficiency of the process $\eta_E = 1$, can be also calculated by (see 3.2):

$$z = \frac{MQ}{96500ndA} \tag{3.8}$$

in which:

Q: transferred charge;
A: deposition surface area;
$M = 208.98$ g/mol;
d: bismuth density (9.78 g/cm^3);
A: deposition surface area;
and n=3 (number of transferred electrons per atom) for bismuth.

The charge Q is measured by the potentiostat.
For the same parameter processes, both current and charge values increase with the sample area.

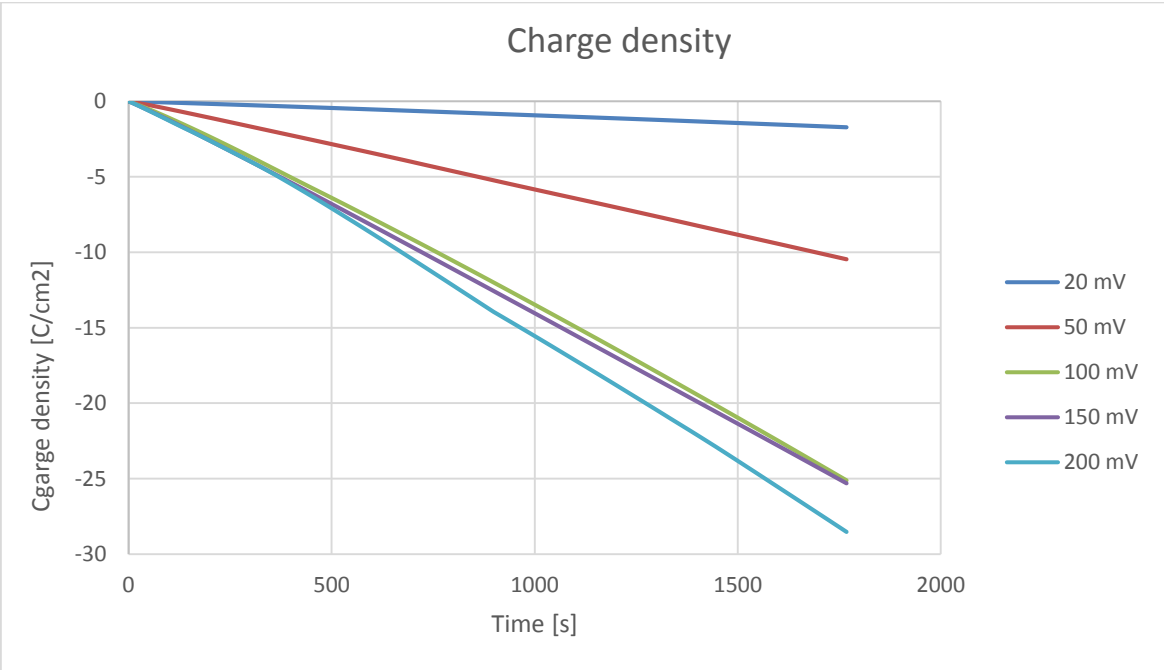

Figure 3.9 - Transferred charge density for the same processes in Figure 3.8.

Characterization tests showed that bismuth layers produced by solution n.1 have more uniform morphology and compactness, together with stronger substrate adhesion, for the following process parameters:

- pH in the range 0.1 ÷ 0.26;
- lower deposition potentials in the tested range (Table 3.4), in particular at *V=-20 mV*;
- bath temperature: 25 ÷ 30 °C;
- bath stirred at 150 ÷ 300 rpm.

Deposition current densities in the range 1 ÷ 10 mA/cm^2 are acceptable, while higher values generally produce less smooth morphologies.

Several thin films (some micron) were deposited with process duration ranging from 30 min to 1h 10 min in order to study the growth process; then very thick layers (up to 66 μm) were grown for times up to 6 h to reach thicknesses requested by the absorber design and to verify the obtained morphology and quality.

Growth rate of about 8 ÷ 10 μm/h for E_s = -20 mV, and about 20 μm/h for E_s = -50 mV were calculated.

By observing the morphology of deposited layers, it was deduced that best process temperature is 25 °C or little more, up to about 30 °C.

To evaluate the constancy of the bismuth ion concentration during the deposition, bath ion depletion during processes were calculated, resulting in 0.5%/h ion consumption; this allows for long depositions (6 ÷ 10 h) to produce very high thickness layers.

It is worth mentioning that this solution, after several hours without stirring, starts forming a white precipitate; in such cases, it was not further used for the electrodeposition and a new solution was prepared.

b) Solution n.2

In Figure 3.10 the current density curves with respect to deposition time are shown for the most relevant experiments performed with solution n.2. The samples used are 10-1, 12-1, 1C, 2B; the bath was neither stirred nor heated.

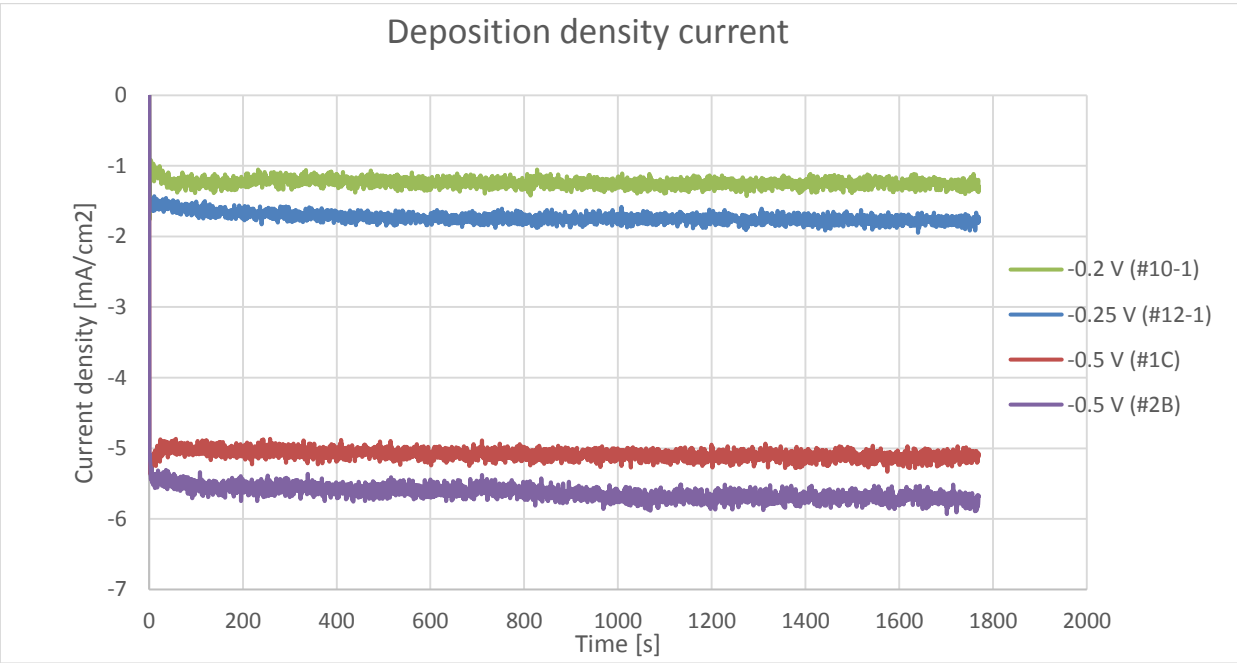

Figure 3.10- Current density - deposition time curves for representative electroplating processes performed with solution n.2.

The transferred charge densities with respect to the deposition time for the same samples are shown in Figure 3.11.

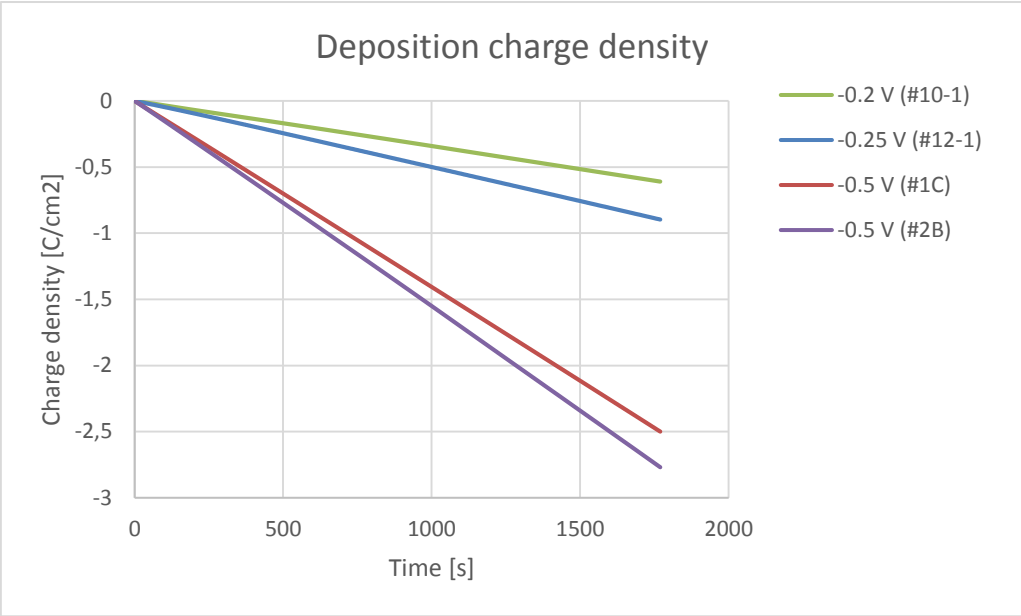

Figure 3.11 - Transferred charge density - process time curves for samples in Figure 3.10.

With this solution, the best results related to morphology and film adhesion were obtained with the following parameters:

- deposition potentials in the range -0.5 ÷ -0.2 V;
- bath temperature: 25 ÷ 30 °C;
- absence of stirring.

The main features of bismuth layers deposited using solution n.2 are the following:

- surfaces have coarser aspects with respect to samples grown with the other solution;
- deposited bismuth contains more percentage of other elements (in particular C and O) with respect to the metal deposited with solution n.1, as revealed by EDX analysis (as detailed in chapter 4);
- very long (some mm) and thick dendrites are present, in particular for $|E_s| \leq -0.5\,V$.

The last point implies that solution n. 2 cannot be used for array fabrication, as thermal short circuits, connecting neighbor pixels, would be produced. The acid solution (solution n. 1) was then chosen to fabricate bismuth absorbers, and baseline process conditions were fixed as reported in the Table 3.5.

Table 3.5 - Best bismuth layer growth process parameters.

Solution n.1			
pH	E_s (mV)	Stirring (rpm)	Bath temperature (°C)
0.1 ÷ 0.26	-50 ÷ -20	150 ÷ 300	25 ÷ 30

After having selected the process, a continuous, large, 60 μm thick film was deposited [156] as a demonstrator for very thick absorber array manufacturing.

The substrate was of the same type used in the previous experiments (glass slide/20 nm Ti/ 20 nm Au), as well as the equipment. To have a very smooth deposition a low potential (E_s = -20 mV) was chosen; considering the achieved deposition rates, the necessary electroplating time was estimated to be 6 h to obtain a layer of bismuth about 60 μm thick.

The solution n.1 was prepared at about 25 °C (room temperature), by the previously described procedure. Its acidity was measured and resulted a pH = 0.13. The copper adhesive tape and the Teflon tape were applied as previously described.

The substrate was then weighted using the precision scale, before the deposition, and its weight resulted: W_b = 0.7342 g.

The electroplating proceeded regularly and smoothly for all its duration; the starting and ending currents were I_s = -3.5 mA and -5.8 mA, respectively; the total transferred charge, as measured by the potentiostat, was Q_t = -31.76 mAh.

The current density with respect to deposition time for this process is shown in Figure 3.12.

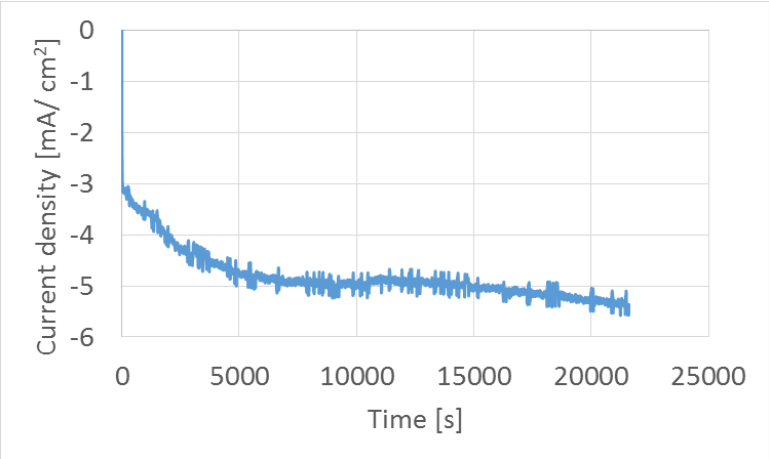

Figure 3.12- Current density - deposition time curve for the 60 μm layer deposition.

After the process end the sample was gently rinsed with DDW and let to dry at room temperature; then it was weighted again, still with copper and Teflon coatings: W_a = 0.8070 g.

The absorber was then characterized, and the results will be described in the next chapter.

3.4 Absorber array microlithographic mask fabrication

After that the deposition of very thick bismuth layers was demonstrated, the efforts were aimed at producing absorber arrays.

Bismuth patterned growth was obtained by masking the substrate with a photosensitive dielectric (photoresist) with patterned openings. The electroplating deposition in this configuration happens exclusively in correspondence with the openings, where the substrate gold is exposed and electroplating current can flow.

Firstly, in order to reach such result, the microlithographic process [157] to obtain the necessary patterns by the photomask lithography [157] had to be developed.

In the photomask lithography technique, an optical mask[1] is used to transfer the mask itself to a substrate coated with photoresist, making use of a suitable light beam. The whole procedure is detailed in Appendix A3.

In order to develop a suitable microlithographic process for absorber fabrication [6, 7], the MA-P1225 positive photoresist was chosen due to its thickness – spinning speed diagram: a 3000 rpm speed for 30 s nominally produces a 2.5 μm thick film; the relatively thick walls help to confine the bismuth growth during the initial phase of the deposition.

In the XACT microtechnology laboratory clean room, the whole microlithographic process was developed by using a 3" x 3" iron dioxide coated glass mask with several test patterns, each of them characterized by different shape (square, circle and triangle), sizes, tilting and gaps; the procedure described below was followed with the parameters reported in Table 3.6:

a) Photoresist coating

Samples prepared as in par. 3.4 were coated with a 2 μm thick MA-P1225 undiluted photoresist layer with a Kemat Technology KW 4A spin coater at 2000 rpm (Table 3.6) for 60 s; A visual inspection confirmed the absence of pinholes.

b) Photoresist baking

Coated samples were baked in oven at 90 °C for 10 minutes in air.

c) Photoresist exposure

The photoresist exposure was performed using a Suss MA6 mask aligner in hard contact mode at 10 mW/cm^2 UV intensity for 30 s (Table 3.6).

d) Photoresist development

Photoresist was developed with MAD 331 developer at room temperature for 60 s.; samples were gently washed with deionized water and blown dry with nitrogen.

Table 3.6 - Best patterning parameters.

Parameter	Value
Spinning speed	2000 rpm
Exposure intensity	10 mW/cm^2
Exposure time	30 s
Development time	60 s

The photoresist surface resulted regular and without pinholes; pattern elements showed well-defined shape, with correct sizes, and vertical photoresist walls; upper corners resulted slightly rounded.

To proceed towards the bismuth absorber array fabrication, a layout was designed containing different 4x4 array patterns, each of them with 400 μm pitch, whose different pad sizes and gaps range in the range 200x200 μm^2 to 375x375 μm^2, and 200 μm to 25 μm, respectively.

[1] An optical mask is a glass or quartz plate coated with an UV opaque layer, such as chromium or iron dioxide, etched according to a pattern; it is transparent to the UV radiation in these etched areas and opaque everywhere else.

Different patterns were designed according to the array design requirements (see chapter 2). The Arrays with different gaps were designed specifically to evaluate the minimum separation compatible with the bismuth lateral growth, in order to maximize the detector quantum efficiencies due to the array fill factor. Some auxiliary patterns were also added: a large 1 mm x 1 mm square to allow the deposited bismuth layer thickness measurement by optical microprofilometry, several long rectangles with different width and four circles to evaluate the uniformity and symmetry of bismuth growth.

The pattern was transferred to a 3” x 3” glass plate coated with iron dioxide by direct laser writing at Dipartimento di Ingegneria of the Università di Palermo, with the following procedure.

At first the mask plate was cleaned following a multi-step procedure:

- degrease in trichloroethilene (TCE);
- rinse in acetone;
- final rinse with absolute ethanol.

Then a microlithographic procedure, very similar to that reported in Par. 4.6, was executed with the addition of a further step for iron oxide chemical etching. The complete procedure is described below for sake of clarity:

a) spin coating with MA-P1225 photoresist using a Kemat Technology KW 4A spin coater at 4000 rpm for 60 s;
b) photoresist baking in oven at T = 90 °C for 5 min;
c) photoresist patterning by high-resolution direct laser writing;
d) photoresist developing with ma-D 331 developer for 1 min at room temperature and successive rinsing in deionized water;
e) iron dioxide wet etching, performed with a solution based on iron (II) chloride.

The optical inspection of the whole layout evidenced the correct opening of all designed features. A microscope photo of the patterned mask is shown in Figure 3.13.

3.5 Absorber array fabrication

Substrates prepared as in par. 3.4 were employed for the bismuth array fabrication.

The previously described test mask was specifically designed to study high thickness bismuth growth in small areas, and in particular:

- to evaluate both shape and area stability during accretion of bismuth;
- to estimate the bismuth layer morphology for different thicknesses;
- to estimate the growth uniformity of single structures related to the overall pattern.

The test mask patterns were transferred on substrates using the same microlithographic process described in Par. 4.6, points a) to d) of the list. The samples where then inspected with the optical microscope to check for defects in photoresist patterns.

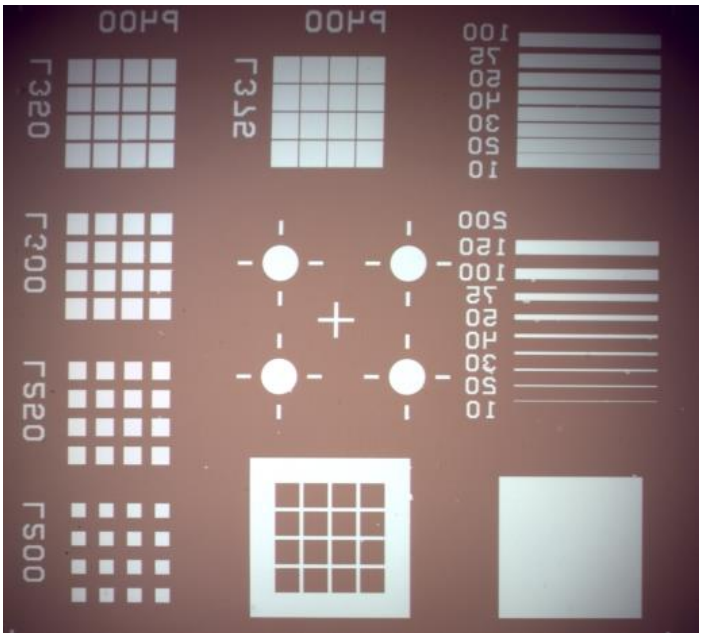

Figure 3.13 - Optical microscope photo of the patterned photolithographic mask.

The electroplating was then performed with the same equipment reported in par. 3.5 using the solution n. 1 at *pH* = 0.12, with the process parameters reported in Table 3.7.

Table 3.7 - Bismuth electroplating parameters for samples with the test patterns.

Sample	Poterntial E_s (mV)	Deposition time (hh:mm)	Bath stirring (rpm)	Bath heating (°C)
2D	-50	1	300	NO
2K	-50	1	150	NO

After the deposition, each sample was gently rinsed with DDW and let to dry at room temperature.

The current - time diagram for the electroplating of sample 2D is shown in Figure 3.14; in this case, it wasn't possible to normalize with respect to deposited area due to the high number of features and their different enlargement with respect to the pattern size caused by the lateral growth of bismuth structures. Current values are lower than those shown in Figure 3.12, due to the reduced deposition area of all patterned features with respect to the large surface of the sample considered in that picture.

The regularity of the current trend and the low noise of the curve indicate the good process quality.

Both optical microscope and SEM observations on growth structures evidenced that their surface areas increase with the layer height, and the stirring speed influences their shapes.

A low magnification SEM photo of some structures grown in sample 2D is reported in Figure 3.15.

After these preliminary tests, absorber array were fabricated in accordance with the design described in chapter 2. Array patterns recorded in the mask were transferred on substrates following the previously described microlithographic process; the optical inspection evidenced no defects in the produced samples. The electroplating process was then performed using the solution n.1. All samples, after the deposition, were gently rinsed with DDW and let to dry at room temperature.

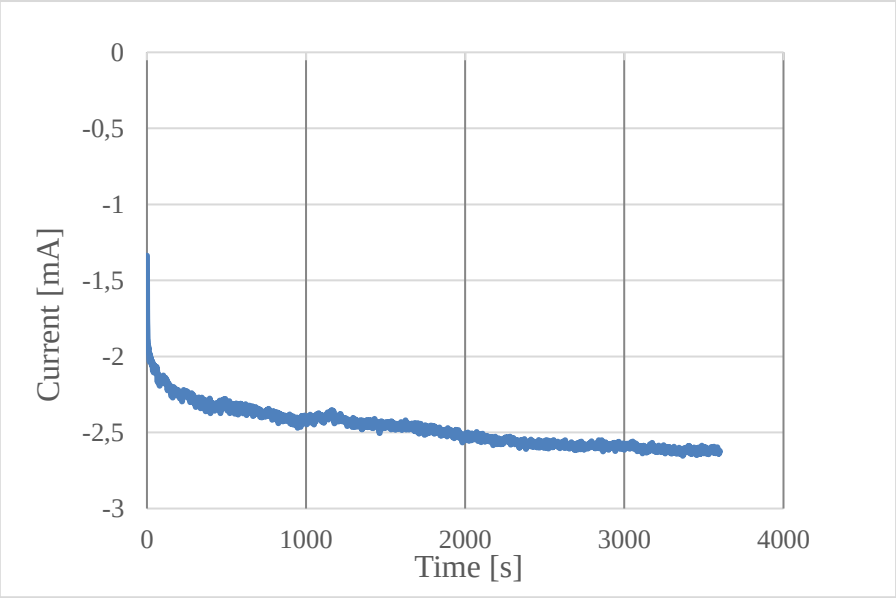

Figure 3.14 - Current - time diagram for 2D sample.

Several samples were produced in order to study array characteristics as a function of the electroplating parameters; Table 3.8 reports a list of the most relevant experiments and the relative parameters. It was not possible to evaluate the area for 1H, 2G and 2F samples due to bismuth lateral growth.

An optical microscope image of the sample 2F absorber array is reported in Figure 3.16; the pixel size is about 360 x 360 μm^2, the gaps are ~40 μm wide.

Table 3.8 - Process parameters for the most relevant experiments on bismuth array electroplating.

Sample	Solution	pH	Area (cm^2)	Potential E_s (V)	Deposition time (hh:mm)	Bath stirring (rpm)	Bath heating (°C)
10-2	n.1	0.13	1.1	-0.02	6	300	NO
1H	n.1	0.16	---	-0.05	3	300	NO
2G	n.1	0.15	---	-0.05	1	150	NO
2F	n.1	0.15	---	-0.1	1	300	NO
10-1	n.2	n.a.	0.91	-0.2	1:10	300	NO
2B	n.2	n.a.	0.787	-0.5	3	NO	NO

The picture demonstrates a quite good geometrical layout of the 4x4 bismuth absorber array. In the next chapter 4 the characterization of fabricated arrays is described.

3.6 Samples for Electrochemical Impedence Spectroscopy (EIS)

In order to better characterize the electrodeposition process with solution n. 1 the electrochemical impedance spectroscopy technique was employed.

To allow the development of this experimental activity, the sample 2A, with the same structure used for the other substrates for the electroplating process, was employed; Sample and bath parameters for the sample 2A EIS are described in Table 3.9.

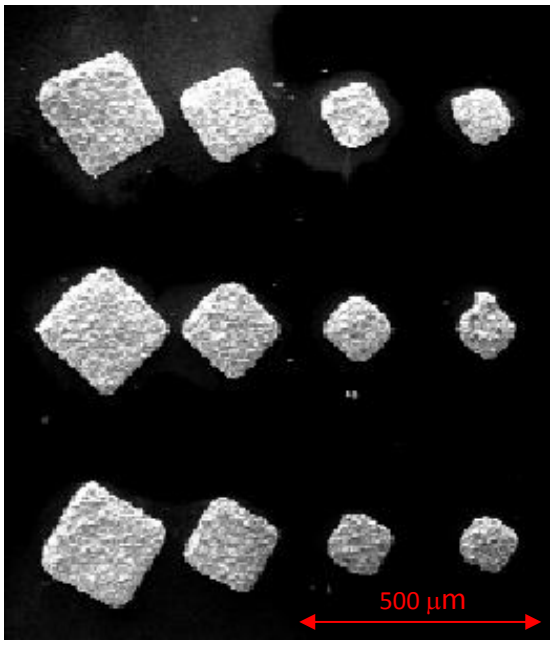

Figure 3.15 - Low magnification SEM photo of some 3D bismuth structures grown in 2D sample (Table 3.7).

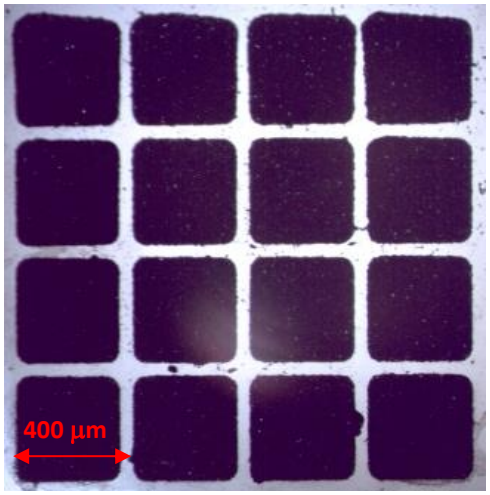

Figure 3.16 - Sample 2F, electroplated bismuth absorber array.

Table 3.9 - Sample and bath parameters for 2A EIS sample.

Sample	Solution	pH	Area (cm^2)	Potential E_s (V)	Bath stirring (rpm)	Bath heating (°C)
2A	n.1	0,17	1,56	-0.05	300	NO

Details on the technique theory and obtained results will be given in chapter 4.

Chapter 4.

ABSORBER CHARACTERIZATION

4.1 Scanning electron microscope observation

Several samples were examined by SEM (scanning electron microscopy) at both high- and low-magnification, to analyze the bismuth layer morphology, the geometry and size of the grown crystals, the presence of microscopic defects. In addition the thickness was measured.

Measurements were performed at Dipartimento di Ingegneria of the Università di Palermo using two a Phenom ProX and a FEI Quanta 200.

Several SEM images of grown bismuth samples, both continuous layers and arrays, are shown in par. 4.6.

4.2 Energy dispersive X-ray spectroscopy

Energy dispersive X-ray spectroscopy (EDX or EDS) [158] is a chemical analytical technique based on X-ray emission by sample surface atoms when irradiated by electron beams. This technique is usually implemented in SEMs.

An electron in the inner shell of an atom can be extracted when hit by another electron with sufficient energy. An electron in an outer shell occupies the hole left in the inner shell and emits an x-ray photon whose energy is equal to the difference between the two energy levels.This energy is a signature of the chemical element and a study of the emitted X-rays and the measurement of the ratio between intensities provides information on the elemental composition of a material sample. The technique can be applied to very small volumes (some μm^3).

Aim of these tests was to obtain information on the deposited layer composition and on the presence of byproducts of the deposition process. Results will be shown in par 4.6.

4.3 Electrical bismuth layer characterization

We used a four point probe method to characterize the electrical properties of the bismuth layer. A test current is injected through pins A and B and the voltage drop is measured between pins A’ and B’ using a high input impedance voltmeter, as represented in Figure 4.1.

According to Ohm’s law the resistivity is:

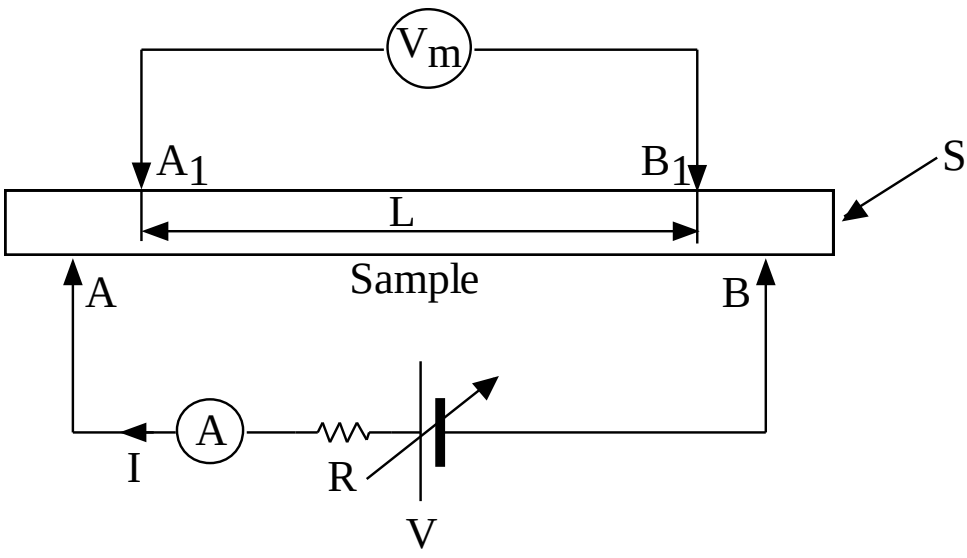

Figure 4.1 - Four point probe method theoretical schematic.

$$\rho = \frac{SV_m}{LI} \tag{4.1}$$

where L is the distance between A1 and B1, V_m is the measured voltage drop, $S = at$ $(a, t \ll L)$ is the cross section of the layer; *a* and *t* are the sample width and thickness, respectively. In practical measurements all the four probes are placed on the same side of the sample (generally fabricated on a substrate), and they are equally spaced from each other; still, usually the sample dimensions don't satisfy the condition $a \ll L$.

In this case, including also the current spreading, the resistivity can be calculated by [159]:

$$\rho = \frac{2\pi LV_m}{I} \tag{4.2}$$

This formula requires spacings among side-by-side measurement tips (A-A1, A1-B1, B1-B) is equal for all couples; (4.2) is most precise when sample dimensions are very large (ideally →∞), and each probe is distant from the sample boundaries by an amount not too small (e.g. some millimeters). The advantages of this method are:

- the low influence of probe contact resistances on measurements;
- the easy implementation;

For practical applications, in which above conditions are not generally fully verified, the method can still be used by introducing a correction factor *f* depending on specific cases as in (4.3); details on its evaluation are reported in [159].

$$\rho = \frac{2\pi LV_m}{I} f \tag{4.3}$$

For thin layers and if $t < L/2$ the correction factor results: $f = \left(\frac{1}{2ln2}\right)\frac{t}{L}$ [159].

4.4 Electrochemical impedance spectroscopy for bismuth layers

The electrochemical impedance spectroscopy (EIS) is an efficient, non-intrusive technique able to provide kinetic information on electrochemical processes [160].

It's based on the perturbation by small amplitude sine voltage waves of the d.c. potential difference applied to the electrochemical cell WE and CE. Varying the frequency of the perturbing signal allows to build an impedance spectrum of the system and to study phenomena occurring at different frequencies.

It's also possible to develop electric equivalent circuits for different processes [160, 161]. Their schematic components are related to phenomena providing information on the growth mechanism, as non faradaic current due to double layer charging/discharging, current flowing in the solution, faradaic current due to charge transfer, adsorption, diffusion that take place during the process itself.

Different electrochemical processes can be modeled by electrical equivalent schematics.

In the general process, the double layer (par. 3.2) is electrically represented by the parallel of the double layer capacitor and the faradic impedance, whose structure depends on the reaction nature (Figure 4.2); if $\bar{Z} = 1/\bar{Y}$ is the double layer impedance, in which $\bar{Y}$ is the electrical admittance, $\overline{Z_f} = 1/\overline{Y_f}$ is the faradic impedance, and C_{dl} is the double layer capacitance, it results:

$$\bar{Y} = \overline{Y_f} + i\omega C_{dl} \tag{4.4}$$

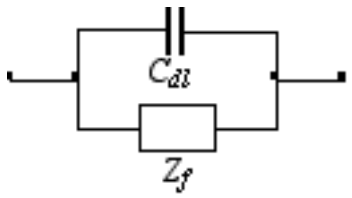

Figure 4.2 - Double layer equivalent circuit.

The solution between the WE and the RE is schematized by a resistor R_s, in series with the double layer impedance; the complete impedance (Figure 4.3) expression for the generic electrochemical reaction between the WE and the RE is:

$$\bar{Z}_{tot} = R_s + \frac{1}{\bar{Y}_f + i\omega C_{dl}} \tag{4.5}$$

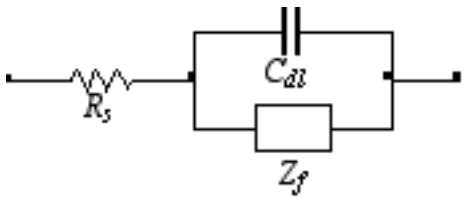

Figure 4.3 - Solution between the WE and the RE equivalent electric schematic in the general process.

If the reaction is a simple electron transfer without any diffusion or adsorption, the faradic impedance is represented by a resistance R_{ct} (charge transfer resistor) i.e. a differential resistance related to the slope of the current-potential curve at the measurement steady state potential.

Substituting $G_{ct} = R_{ct}^{-1}$, the impedance expression becomes:

$$\bar{Z}_{tot} = R_s + \frac{1}{G_{ct} + i\omega C_{dl}} \tag{4.6}$$

and the equivalent circuit, including the solution resistance R_s, is shown in Figure 4.4.

In the case of a one-step reaction with diffusion the faradic impedance is the series of two different components: the charge transfer resistor R_{ct} and the Warburg impedance $\bar{Z}_W$, related to the diffusion.

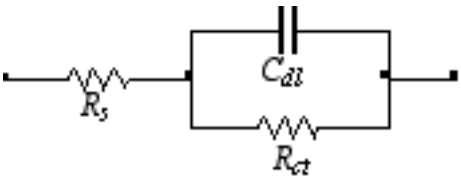

Figure 4.4 - Equivalent circuit for a simple electron transfer reaction (simplified Randles equivalent circuit).

In this case the impedance expression is given by (4.7) with $\bar{Y}_f = \frac{1}{R_{ct} + \bar{Z}_W}$, and the complete equivalent network (Randles equivalent circuit) is shown in Figure 4.5.

$$\bar{Z}_{tot} = R_s + \frac{1}{\bar{Y}_f + i\omega C_{dl}} \tag{4.7}$$

Figure 4.6 is the equivalent circuit of a one step reaction with absorption. The faradic impedance is constituted by the series of the charge transfer resistor and the capacitor C:

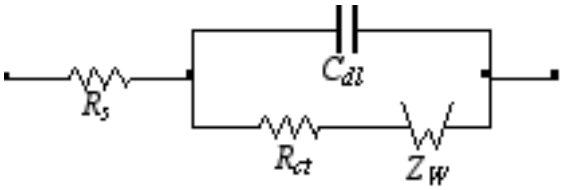

Figure 4.5 - Randles equivalent circuit for the one-step reaction with diffusion.

$$\bar{Y}_f = \frac{1}{R_{ct} + (i\omega C)^{-1}} \tag{4.8}$$

$$\bar{Z}_{tot} = R_s + \frac{1}{\bar{Y}_f + i\omega C_{dl}} \tag{4.9}$$

The related electric equivalent schematic is reported in Figure 4.6.

A more general case is represented by a process constituted by a one step reaction with both adsorption and diffusion; the complete expression of the faradic impedance is:

$$\bar{Z}_f = \frac{1}{\bar{Y}_f} = R_{ct} + \bar{Z}_W + \frac{1}{i\omega C} \tag{4.10}$$

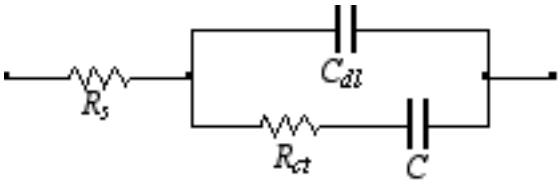

Figure 4.6 - Equivalent electric schematic for the one-step reaction with absorption.

in which:
$\bar{Z}_W$: Warburg impedance;
C: absorption capacitance,

and the impedance $\bar{Z}_{tot}$ is given by (4.5) in which $\bar{Y}_f$ is the reciprocal of (4.10); the related electrical equivalent model is shown in Figure 4.7.

The bismuth electroplating using solution n.1 is a reaction described by Figure 4.7 model.

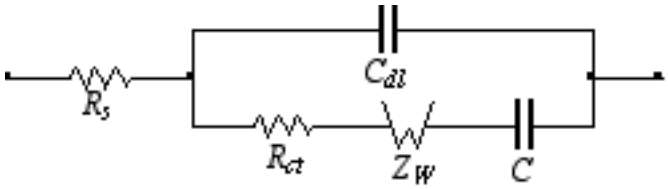

Figure 4.7 - Electrical equivalent schematic of the one step reaction with both adsorption and diffusion.

Impedances of all the above equivalent networks can be graphically represented using Bode's and Nyquist's plots.

The first show the impedance module $\overline{|Z|}$ logarithm with respect to the frequency logarithm , and the impedance phase $\sphericalangle Z$ with respect to the frequency logarithm respectively.

The Nyquist's diagram represents the impedance imaginary part $Im(\bar{Z})$ as a function of the real part $Re(\bar{Z})$ and the frequency (or angular frequency) as a parameter. In electrochemistry $-Im(\bar{Z})$ is usually plotted in the Nyquist's diagram.

The various components represented in the equivalent electrical circuits can be identified analyzing the Bode diagram. Horizontal lines are related to resistors, lines with slope -1 (-45° angle) are due to capacitors, and lines with slope -0.5 (-26.56°) are related to the Warburg component, representing the diffusion process.

A typical amplitude Bode's plot for a general electrochemical process with involved several phenomena is shown in Figure 4.8 where lines indicated by 1, 2 and 3 represent, respectively, an absorption, a diffusion, and the double layer capacity.

Some component values in above equivalent circuits can be directly evaluated by Nyquist's diagrams; an example is reported in Figure 4.9 for the simple electron transfer reaction (see Figure 4.4.).

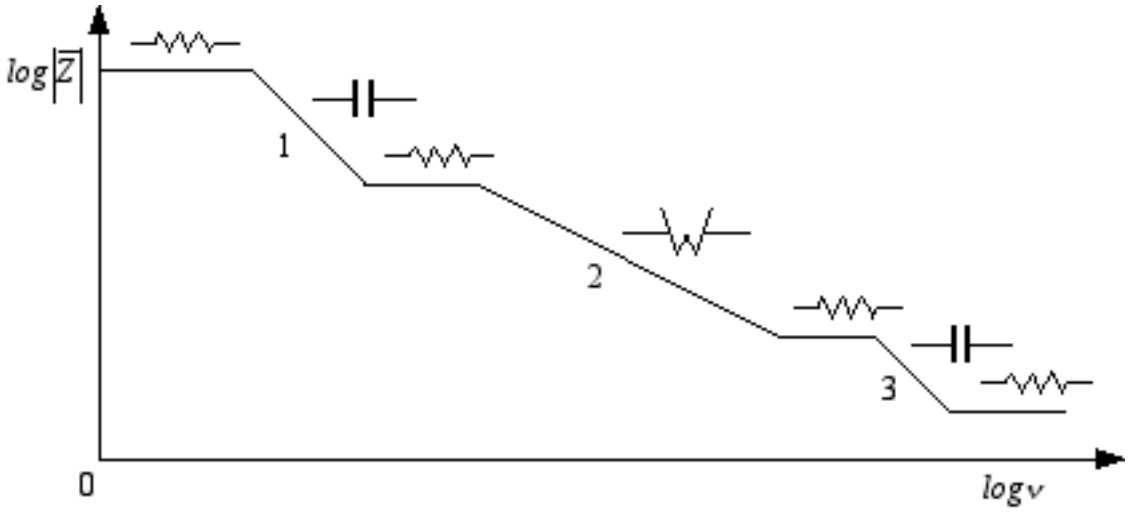

Figure 4.8 - Typical module Bode's plot for a general electrochemical process.

The R_s value is given by the left intercept of the semi-circumference (ideally $\omega \to \infty$) with $Re(\bar{Z})$ axis, while the semi-circumference diameter is R_{ct}.

For more complex reactions Nyquist's diagrams are more complicated; in general the semi-circumference is substituted by a less than 180° arc that, at low frequencies, instead of approaching the $Re(\bar{Z})$ axis, is connected to a straight line with a positive slope, and $|Im(\bar{Z})|$ increases when $\omega \to 0$; or, in other processes, more than one arc can appear in the diagram.

In such circumstances electrical component values can be evaluated by plotting the Nyquist's diagram by experimental data, then by recognizing different feature composing it, and obtaining the related information by each of them.

The other component values in equivalent circuits can be then calculated by analytical expressions; for example, measured $\bar{Z}_{tot} = \bar{Z}^*_{tot}$ at $\omega = \omega *$, and evaluating R_s and R_{ct} from(4.6) the double layer capacitance C_{dl} can be obtained.

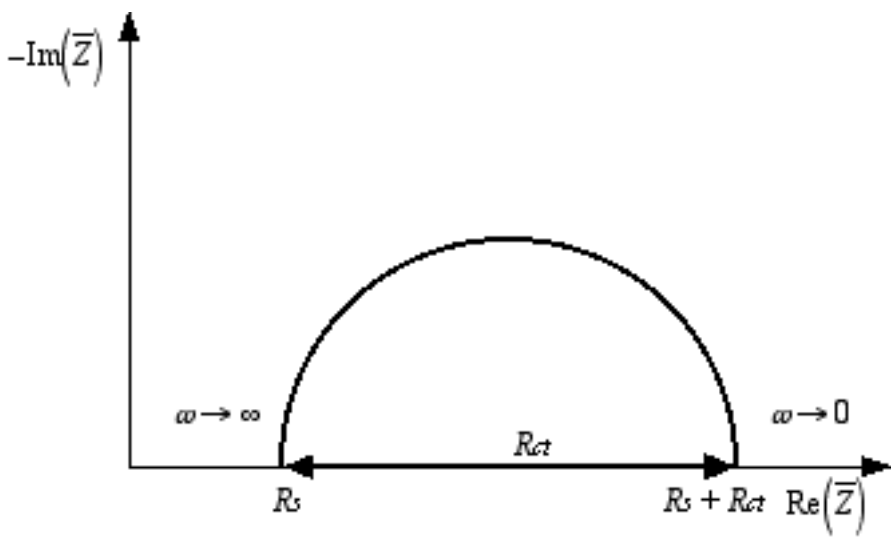

Figure 4.9 - Evaluation of R_s and R_{ct} values by Nyquist's diagram.

The bismuth sample characterization by the EIS technique was performed at the Electrochemical Material Science Laboratory of the Dipartimento di Ingegneria of the Università di Palermo using a Parstat 2263 potentiostat in the three electrode configuration.

4.5 Other absorber characterization methods

For x-rays absorption purposes the height and profile of the layer are of great importance. The height must be uniform all over the detector to ensure a space uniform performance. In order to measure the layer height and uniformity we employed the following techniques:

- sample weighting before and after deposition;
- confocal sensor microprofilometer measurements.

1) Sample weighting before and after deposition

Substrates coated with both the copper and the teflon film were weighted with a precision (100μg) scale before electroplating; after electroplating, rinsed with bidistilled water and dried at room temperature a second weight measurement was done to evaluate the amount P_{dep} of deposited material.

This allows to evaluate the bismuth layer thickness independently of the electrical efficiency of the process:

$$z_\eta = \frac{P_{dep}}{dA} \tag{4.11}$$

where:
d: bismuth density (9.78 gcm^{-3});
A: deposition area.

The deposited thickness *z*, in the hypothesis that the electric efficiency of the process $\eta_E = 1$, can be also calculated by (see (3.2):

$$z = \frac{MQ}{96500ndA} \tag{4.12}$$

in which $M = 208.98$ $gmol^{-1}$ and *n*=3 (number of transferred electrons per interested atom) for bismuth. The charge *Q* is measured by the potentiostat and therefore the electrical efficiency of the process can also be calculated:

$$\eta_E = \frac{z_\eta}{z} \tag{4.13}$$

2) Confocal sensor microprofilometer measurements

Another, more precise, technique to evaluate deposited layer heights is based on the use of an optical microprofilometer, shown in Figure 4.1 (schematic) and in Figure 4.11 (photos).

The equipment, installed in the XACT laboratory class 1000 clean room, finalized to x-ray equipment and components assembling, testing and storage, is constituted by:

- the variable pressure, static pressurization system (Figure 4.10 and Figure 4.11a);
- the optical, contactless confocal sensor Micro-Epsilon ConfocalDT IFS2405-10 (Figure 4.10 and A in Figure 4.11b) with Micro-Epsilon IFC 2421 controller;
- the computer-controlled, motorized x-y-z micropositioning system (B in Figure 4.11);
- the control computer (C in Figure 4.11).

Also, a proprietary developed post-elaboration software allows to refer all measurement to a reference plan and to reduce noise by smoothing curves.

All constituent parts will be now briefly described.

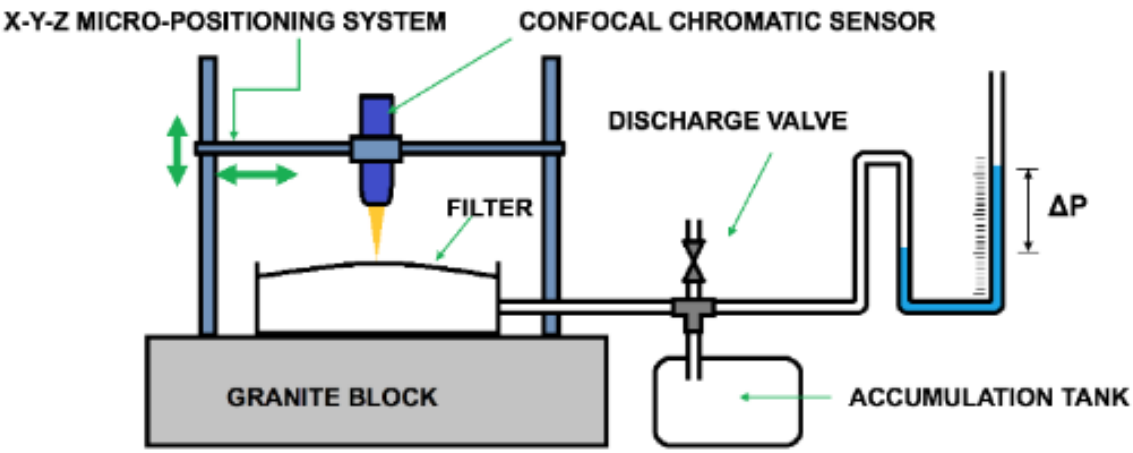

Figure 4.10 – Schematic of the optical microprofilometer.

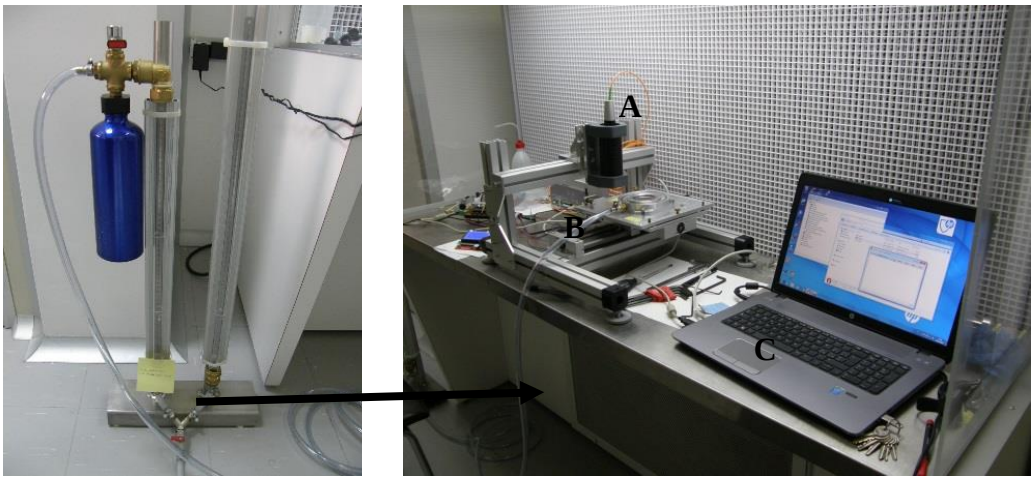

a) b)

Figure 4.11 - Optical microprofilometer system at XACT INAF-OAPa laboratory; a) static pressurization system; b) confocal sensor (A), micropositioning system (B), and control computer (C). Sensor controller, computer-to-motor interfaces and power supplies are at the left of B.

Optical, contactless confocal sensor Micro-Epsilon ConfocalDT IFS2405-10 with Micro-Epsilon IFC 2421 controller [162, 163].

This system is based on a high precision distance sensor and it was developed for both static and dynamic surface profile evaluation. The confocal sensor receives LED emitted white light in the controller by a multimode core optical fiber, and its optical lenses focus the different chromatic light components at different distances on the measuring surface. Reflected light components are sent, by the same optical path (lenses plus fiber), to the controller, in which the related spectral analysis in executed, and obtained data are processed to calculate distances from the sensor to the sampled surface points, allowing profile reconstruction.

Main Confocal DT IFS2405-10 sensor technical features are reported in Table 4.1.

Table 4.1 - Main ConfocalDT IFS2405-10 sensor technical features.

Measuring range	10 mm
Probe optical resolution	60 nm
Light spot diameter	16 μm
Sampling rate	Up to 6.5 kHz

The block schematic of the controller is reported in Figure 4.12 [162].

The system firmware in the controller allows setting several parameters (e.g. measurement configuration, exposure time, signal quality), in order to optimize measurement results with respect to the analyzed surface (diffusing or reflecting, roughness degree, etc.).

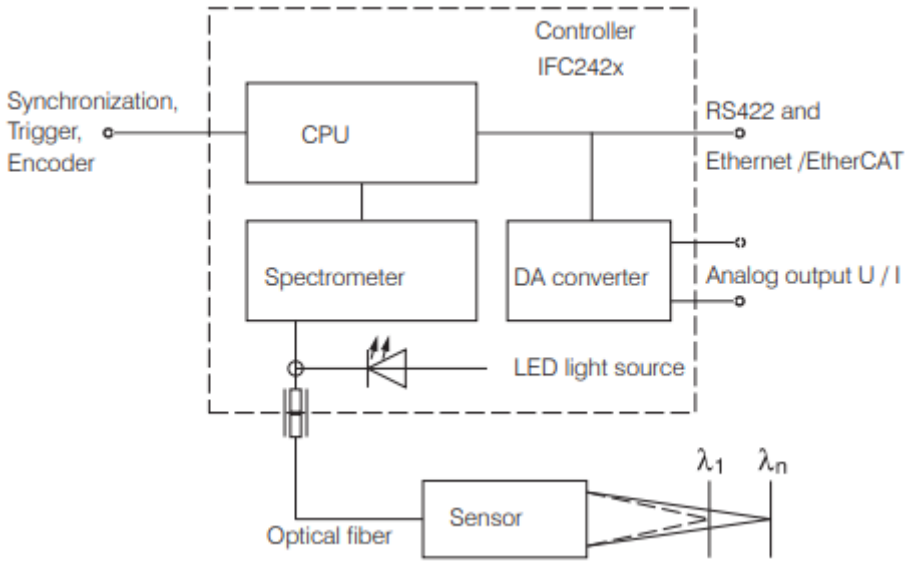

Figure 4.12 - Block schematic of the IFC 2421 controller [162].

Computer-controlled, motorized x-y-z micropositioning system

The sensor is mounted on a proprietary motorized x-y-z micropositioning system (Figure 4.13) needed both to set the measuring starting point and to scan surface in one or two dimensions to obtain its height or roughness 1D or 2D profile.

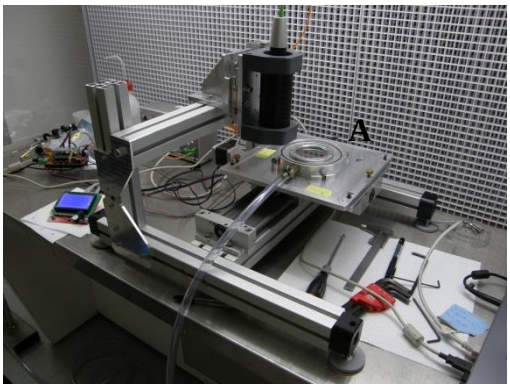

Figure 4.13 - Detail of the computer controlled, motorized x-y-z micropositioning system; A: sample holder.

4.6 Absorber characterization

Bismuth layers grown by solutions n.1 and n.2 exhibited very different features (morphologies, thicknesses, defects), so the characterization using the described techniques was needed to evaluate their properties and features, and to define the best fabrication processes, as described in chapter 3.

The acid solution produced best results and was therefore selected. In the following we will firstly show two characterizations of samples produced using the solution n.2 to demonstrate the correctness of our choice, and then both planar and array absorber characterization will be reported.

Solution n.2 sample characterization examples

Sample 2B

The process parameters for this sample are reported in Table 4.2. The deposition area is defined by the manually placed Teflon film, so it is different for each sample.

Table 4.2 - Sample 2B process parameters.

Sample	Area (cm^2)	Potential E_s (V)	Deposition time (hh:mm)	Bath stirring (rpm)	Bath heating (°C)
2B	0.787	-0.5	3	NO	NO

The optical microscope observations show a uniform surface, almost defectless, dark colored, and with about uniform height (at the observation scale); several side dendrites along borders were grown.

The scotch test evidenced no material picking, so indicating very good layer adherence to the substrate.

The initial (before the electroplating) and final sample weight (with both copper and Teflon films) were w_b = 0.7948 g and w_a = 0.8378 g; the deposited bismuth weight resulted P_{dep}=0.043 g; but it was not possible to calculate the layer height by (4.1) due to the long dendrites, bringing enough mass out of the layer.

Then SEM observations and EDX analysis were performed.

In Figure 4.14 SEM images of the sample surface, both at low (a) and high (b) magnification are reported.

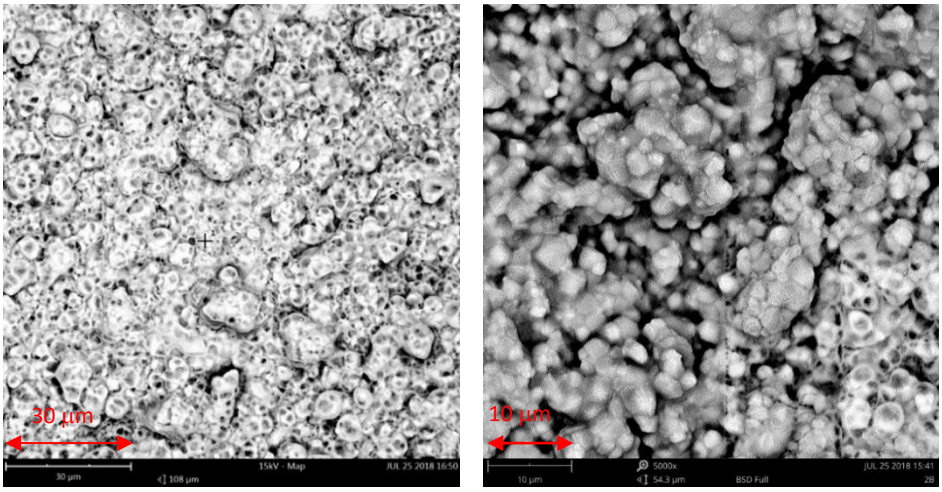

a) b)

Figure 4.14 - Low (a) and high (b) magnification SEM photos of the 2B sample surface.

The surface is generally uniform, but bismuth typical crystals are not evident.
The EDX analysis graphic is shown in Figure 4.15.

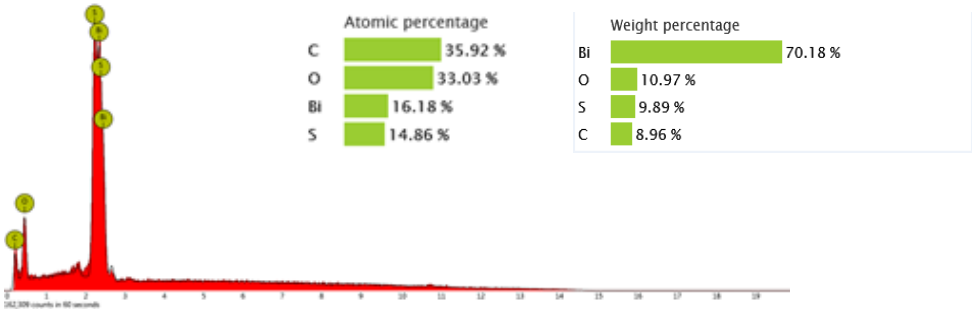

Figure 4.15 - EDX analysis for the 2B sample.

In this sample elements other than bismuth are present. Bismuth is present at 70.18% level in weight (bismuth has a high atomic mass), but carbon and oxygen are present with high atomic percentages. Probably this is the reason for the surface morphology shown in Figure 4.14.

Sample 10-1
The experimental parameters for this process are reported in Table 4.3.
The optical microscope observation showed a non-uniform bismuth layer.

Table 4.3 - Sample 10-1 process parameters.

Sample	Area (cm^2)	Potential E_s (V)	Deposition time (hh:mm)	Bath stirring (rpm)	Bath heating (°C)
10-1	0.91	-0.2	1:10	300	NO

After the process the weight increased by 0,011 g, corresponding to an approximate 12 μm layer height (overestimated since about 1 mm dendrites are present on the sides) The dendrites are smaller than in 2B sample because of lower deposition potential and shorter process time are.

The SEM observations evidenced many small vacancies, approximately round with some micron diameter, or with rectangular shape, whose length was about 5-6 μm. This can be observed in Figure 4.16 a and b. Small crystal structures are generally present.

The EDX analysis showed a large oxygen presence, reducing the bismuth quality (Figure 4.17).

These two examples synthetize the general characteristics of samples processed with solution n.2. This bismuth layers contain more spurious elements, as shown by EDX examination, with respect to solution n.1 process. Vacancies often appear in the film and lateral dendrites (also some millimeter long) are evident. The size of the dendrites increases with deposition potential and time. No dendrite are present in samples grown with the other process.

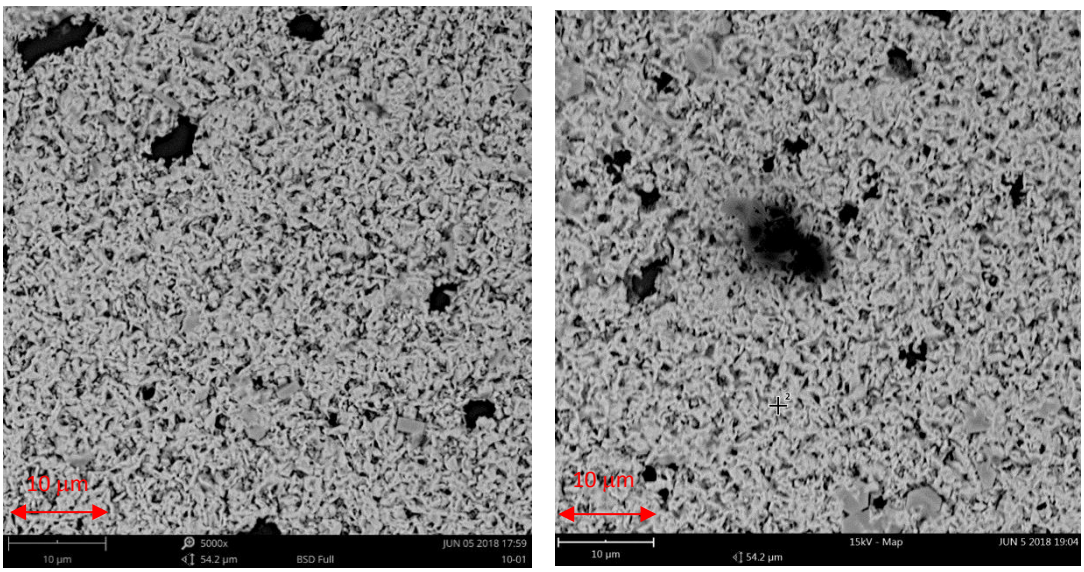

a) b)

Figure 4.16 –SEM micrographs of two different areas of sample 10-1 surface (a, b); several vacancies are evident.

The low bismuth quality and lateral dendrites, that would cause thermal shorts between array pixels, of layers produced by solution n.2 depositions made it non suitable to produce the needed bismuth absorber arrays.

Very thick bismuth layer (absorber fabrication test) characterization

The large area, very thick bismuth layer, fabricated as a test for absorber production, fabricated by the electroplating process with solution n.1 (par. 3.3), observed at the optical microscope, evidenced a fair, uniform and defect-free surface, without dendrites.

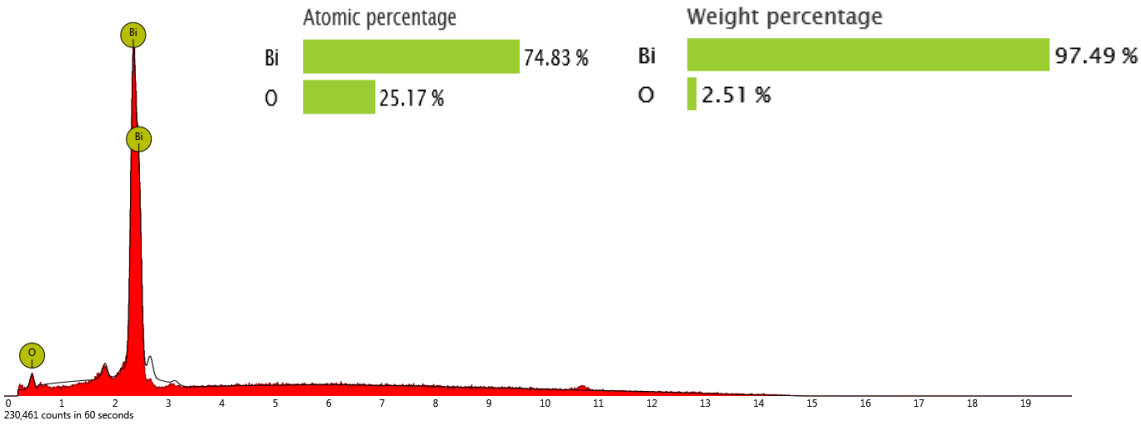

Figure 4.17 - EDX analysis for the 10-1 sample.

The process parameters are described in detail in the par. 3.3. During the deposition the current density curve with respect to time (Figure 3.12) evidenced some noise.

The initial and final weights of the sample (with both copper and teflon films) were $W_b = 0.7342$ g and $W_a = 0.8070$ g; the deposited bismuth weigh was $P_{dep} = 0.0728$ g. Assuming the nominal bismuth density, the thickness is about 67 µm.

The electroplating process resulted in more than 88% efficiency. The four point method characterization evidenced a resistivity of about $1.5.10^{-5}$ Ω·m; this value is higher than the $1.15 \cdot 10^{-6}$ Ω·m of pure crystalline material, probably due to the presence of several crystal phases. SEM observations evidenced a strongly polycrystalline structure without vacancies (Figure 4.18a,b), thus confirming our hypothesis. The bismuth crystal structure is well visible in Figure 4.18b.

The absorber lateral view, used to estimate the layer thickness, is shown in Figure 4.18c. The 66.7 µm value measured confirms the thickness estimated by the layer weight.

The EDX analysis results are reported in Figure 4.19 and show a contaminant free deposition at the instrument sensitivity level apart the two main peaks, secondary bismuth peaks can be observed.

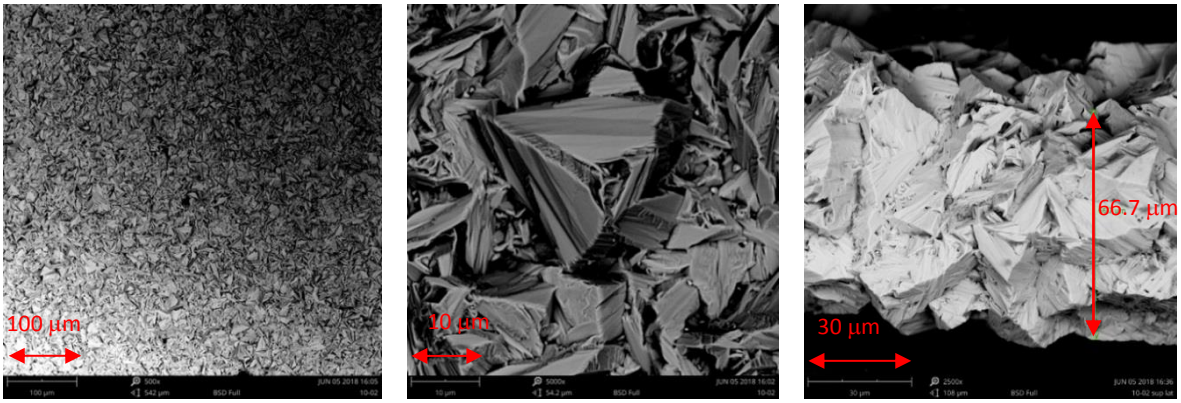

a) b) c)

Figure 4.18 - Electroplated large area bismuth absorber SEM micrographs: low magnification (a); high magnification (b); lateral view with about 67 µm measured thickness evidenced (c).

<u>Absorber array characterization</u>

Process parameters for most representative absorber array fabrication are reported in Table 4.2. The optical microscope observations (Figure 4.) evidenced what follows [164]:

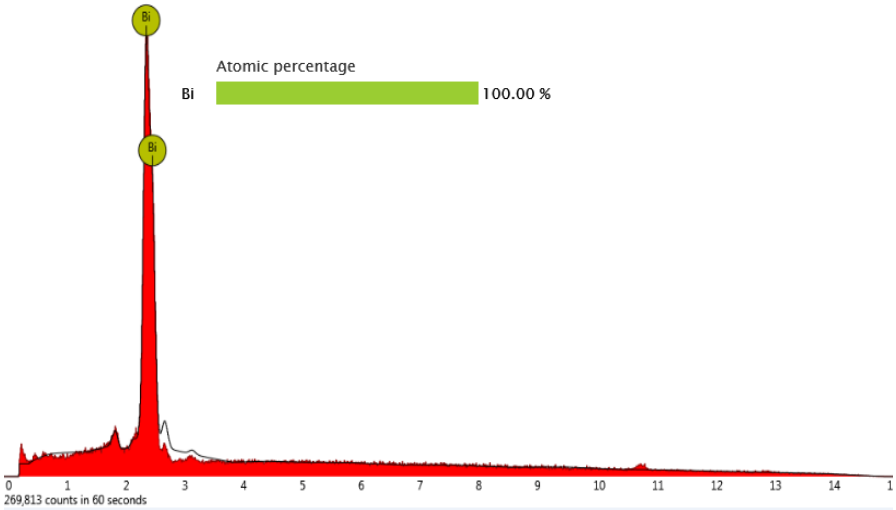

Figure 4.19 - EDX analysis of the large area bismuth absorber.

- electroplating voltage influences bismuth morphology; lower (in absolute value) voltages (e.g. -50 mV) produce smoother surfaces with respect to higher voltage (e.g. -100mV);
- about 10% enlargement on each side was estimated for each bismuth pixel with respect to the related mask layout; this is due to the lateral deposition during the metal accretion. This enlargement depends also on the process time;
- the deposition time influences also the pixel stacking during growth: the 3h deposition (Figure 4.20b) produced also the smallest lateral dendrite formation;
- the stirring speed influences also the pixel growth as it can be seen comparing Figure 4.20a and c, related to processes at 150rpm and 300rpm respectively. In Figure 4.20a pixels are almost square with right, slightly rounded, angles, but there is less uniformity in lateral growth; in Figure 4.20c upper row pixels (in the picture) show increased shape deformation near the upper-left corner, probably due to the bath stirring.

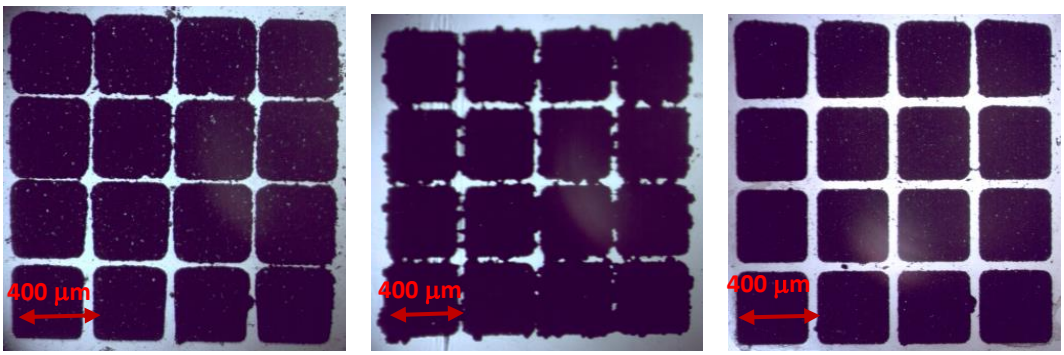

a) b) c)

Figure 4.20 - Optical microscope photos of 4x4 bismuth arrays; a) -50mV, 1h, 150rpm (sample 2G); b) -50mV, 3h, 300rpm (sample 1H); c) 100mV, 1h, 300rpm (sample 2F); the pixel size is about 360x360µm^2; about 40µm gaps in c).

The calculated fill factor for Figure 4.20c array was about 81%.

Using the optical microprofilometer the large area square (auxiliary feature) heights in the array mask pattern (bottom right square in Figure 4.1) for Table 3.8 samples were measured. Since all the features in each pattern grew during the same process their thicknesses can be considered the same.

The surface profile acquired for the 2G sample large square, after the mathematical smoothing, is reported in Figure 4.21 as an example.

The wide amplitude noise, evidenced in the plot oscillations, is due both to the high surface roughness and to irregular reflections by the crystals. The average height value is about 42 μm.

The 1H and 2F sample thicknesses resulted 55 μm and 15 μm respectively; the sample 1H thickness is about 60 μm, as specified for the high energy x-ray absorber array. This demonstrates the feasibility of microcalorimeters specified in the MISTERX project.

Absorber array characteristics can be optimized. In particular:

- evaluating the pixel size increase with their height the array fill factor can be increased;
- stirring the solution more uniformly the array pixel shape and size turn out more regular;
- using a much thicker photoresist to pattern the arrays prevents the growth of lateral dendrites .

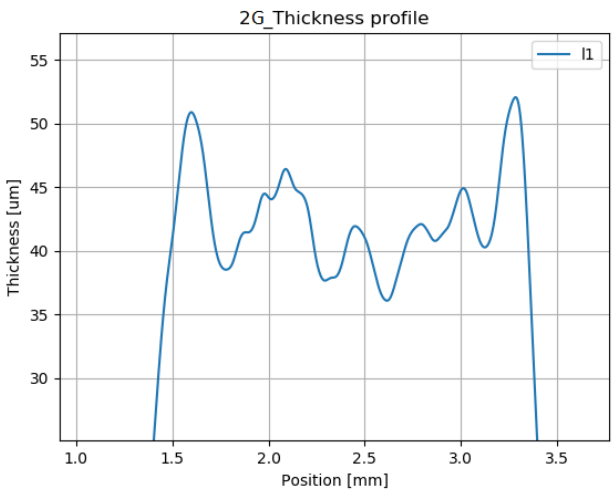

Figure 4.21 - Optical profilometer large square surface profile for the 2G sample.

4.7 Electrochemical Impedance Spectroscopy characterization

In order to study the kinetic of electrodeposition process with solution n.1, EIS spectra have been recorded at three different times during the electrodeposition at -0.05 V vs. Ag/AgCl with frequency ranging between 100 mHz and 1 MHz at each time.

EIS spectra were recorded at t = 0 min soon after the start of electrodeposition and at t = 10 min, t = 20 min and t = 30 min (end of electrodeposition). In Figure 4.22 and Figure 4.23 the EIS spectra for 2A sample in the Bode's plot representation are shown. Figure 4.22 clearly shows the decreasing of impedance module in low frequency region by increasing the deposition time. This can be explained by considering that a reduction of charge transfer resistance occurs. Modeling with a one time constant equivalent circuit R(RQ) it is possible to estimate a reduction of the charge transfer resistance from ~ 200 $\Omega \cdot cm^2$ to ~ 30 $\Omega \cdot cm^2$. This can be explained by considering a change in the kinetic of electrodeposition process since at low deposition time the bismuth is electrodeposited on gold substrate while at high deposition time the bismuth is electrodeposited on growing bismuth layer. According to this, a reduction of the kinetic constant k_0 to take into account the activation energy for

the electrodeposition process must be considered. The charge transfer resistance is a function of the kinetic constant k_0.

It is also evident that the phase angle values move to lower values by increasing the deposition time (Figure 4.23). This can be explained by considering that by increasing the bismuth layer thickness the metallic behavior of the electrode increases. Consequently, a reduction of the phase angle toward zero (pure resistive behavior) occurs. The equivalent circuit R(RQ) shows a reduction of the series resistance from ~ 18 $\Omega \cdot cm^2$ to ~ 4 $\Omega \cdot cm^2$. The series resistance accounts for the electrolyte resistance and for electrode resistance. By assuming that the electrolyte resistance doesn't change during the electrodeposition time, the reduction of series resistance is probably the consequence of a reduction of the electrode resistance due to the growth of a bismuth layer thicker than the thin gold substrate.

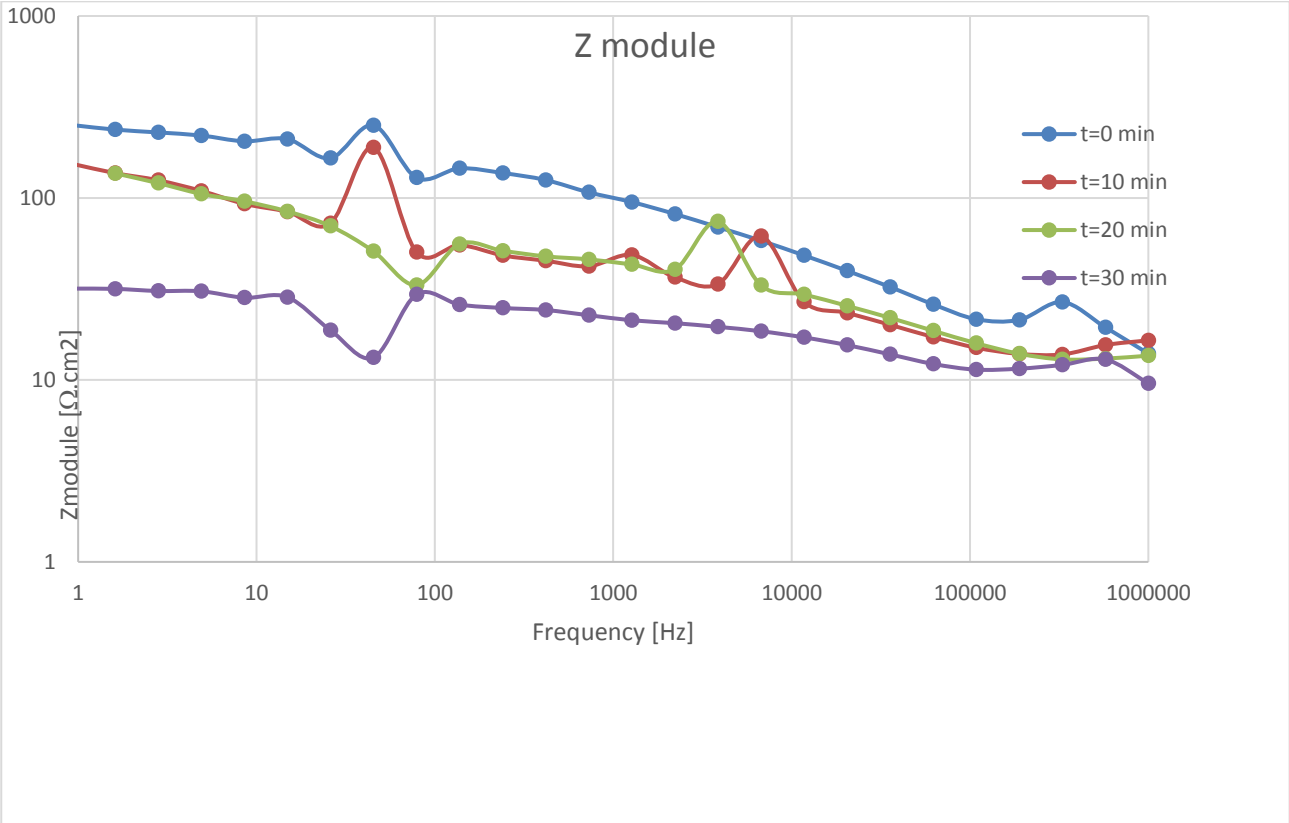

Figure 4.22 - Bode's module plot for 2A sample (EIS parameters in the text).

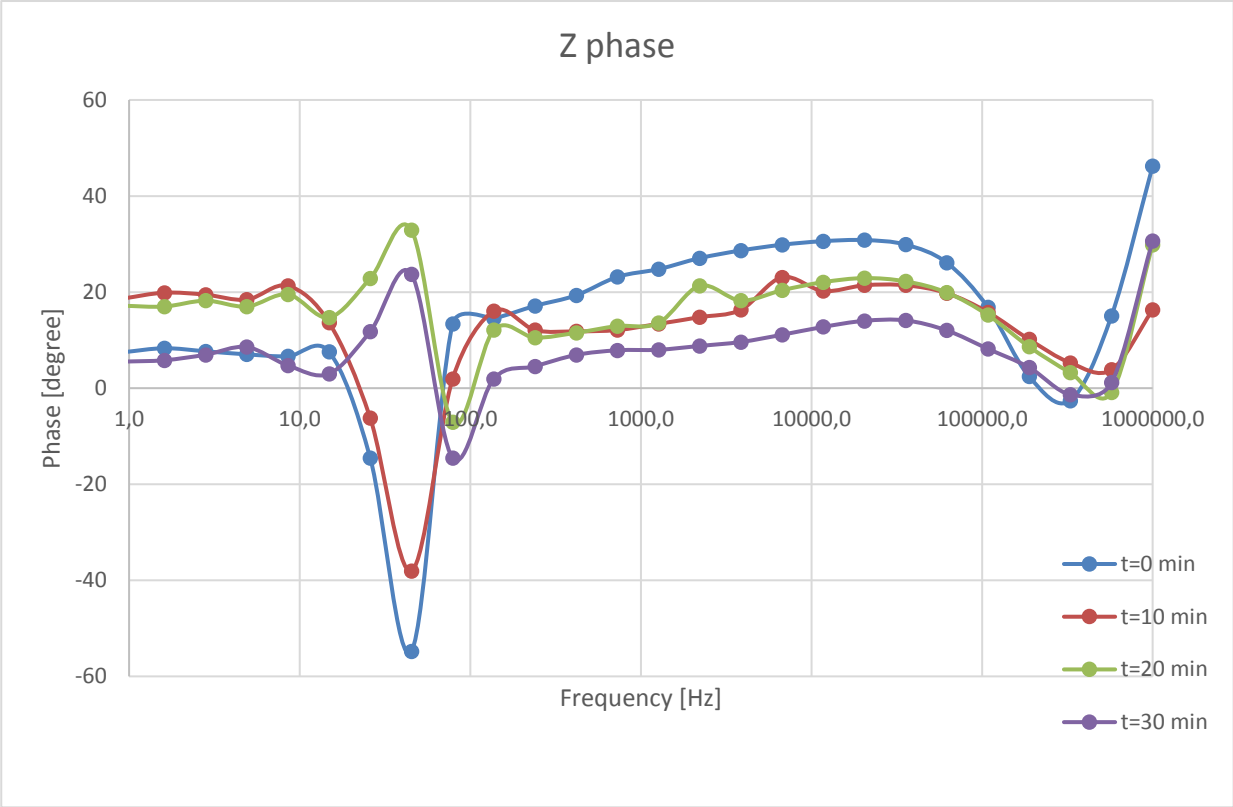

Figure 4.23 - Bode's phase plot for 2A sample (EIS parameters in the text).

4.8 Conclusions

The characterization of fabricated samples of bismuth deposited layers and absorber arrays was performed by different techniques. Some guidelines in order to optimize growth processes to fabricate absorber arrays for hard x-ray microcalorimeters were set.

Lower (in absolute value) electroplating voltages (50 mV) produce smoother surfaces with respect to higher ones .

About 10% enlargement for each side of each pixel with respect to the mask pattern dimensions was estimated, due to lateral bismuth deposition. This value depends on the deposition time.

The order in pixel growth depends on deposition time. High values (several hours) tend to produce small lateral dendrites .

The stirring speed influences the pixel growth by deforming their surface shape.

In order to optimize the array fabrication, the following rules must be applied:

- the array fill factor must be optimized by evaluating pixel enlargement due to their lateral growth in array pattern design, so to minimize gaps;
- speed and uniform stirring must be set properly to fabricate arrays with shape and size pixels within the specified parameters
- photoresist to define the pixel pattern must be thick enough to prevent heat shorts between adjacent pixels.

The electrochemical impedance spectroscopy technique was also applied to characterize the electroplating process, to trim process parameters and to produce better quality bismuth layers.

Presently, further EIS data analysis is ongoing, to best characterize and optimize the bismuth deposition process. A new electroplating cell is under fabrication, allowing more accurate control of deposition parameters and soft stirring by recirculation of the solution, in order to avoid side tilting effects during the pixel growth.

Chapter 5

CHARACTERIZATION OF FILTERS FOR MICROCALORIMETERS

5.1 Scope of the activity

Cryogenic x-ray detectors require suitable filters to be shielded by several perturbative both external and internal factors: radio-frequency (RF), microwave (MW), infrared (IR), visible (Vis), ultraviolet (UV) radiation, and molecular contamination originating inside the spacecraft. The warm surfaces inside the detector cooling system constitute a thermal load for microcalorimeters; mainly IR radiation, Vis, UV radiation is emitted by different space bodies and constitutes a relevant optical load; RF is generated by onboard telemetry systems and electronics. Moreover, secondary electrons and low energy ions generated by the impact of energetic (from few keV to hundreds of Mev) cosmic particles with the spacecraft may hit the microcalorimeters depositing an amount of energy in their sensitivity range, thus producing a signal similar to X-ray photons. Filters may partially scatter such low energy particles and thus play a role in the total detected background events.

Furthermore, thermal filters have to be characterized by very high transmission in the X-ray band, to avoid signal loss; still, they have to resist to both the strong mechanical stress and the very intense acoustic waves produced by the spacecraft launch.

Another detrimental effect for thermal filters is due to the molecular contamination, produced by the particles in the surrounding chambers sticking on them and thus causing a reduction of the low energy X-ray sensitivity.

The characterization of microcalorimeter filters is aimed to evaluate most physical (mechanical, acoustic, thermal, electromagnetic, X-ray transmission) features of these devices, to verify the compliance of fabricated items with flight requirements. In particular, related to Athena mission, specifications are set by the ESA standards [165].

As a complementary activity for microcalorimeter design and fabrication, a thermal filter characterization activity was performed, related to two different device types:

- Athena X-IFU baseline thermal filters based on thin polyimide;
- Filters based on thin silicon nitride (Si_3N_4) membranes, investigated as a possible alternative to polyimide ones both for Athena and other future high-energy space missions.

<u>Athena X-IFU baseline filters</u>

The X-IFU microcalorimeters will operate at a temperature close to 100 mK inside a sophisticated multi-stages detector cooling system (DCS). To allow the X-ray photons, focused by the large area Athena telescope, to reach the X-IFU detector at the focal plane, windows have to be opened on the cryostat thermal and structural shields. Thermal filters (TF) need to be mounted on such shields to attenuate the radiative heat load from warm surfaces, but they are required to be highly transparent in the X-ray energy range of interest. For this reason, the TFs need to be very thin and made of light materials, but at the same time they have to be resistant enough to withstand severe launch stresses and space environment radiations [13, 57].

The TFs, beside protecting the detector from IR radiative load, have to protect the detector from molecular contamination and attenuate radio frequency (RF) generated from the spacecraft telemetry and onboard electronics. The TFs also contribute together with an optical blocking filter (OBF), mounted on a filter wheel, to reduce the optical load from bright UV/Vis astrophysical sources [166]

Athena X-IFU baseline filters [167, 168, 169] are made of a thin (45 nm) polyimide membrane, coated by a 30 nm aluminum layer; the membrane is glued to a hexagonal mesh, made by SAE 304 stainless steel for all filters except for the coldest one operating at 50 mK, that is the temperature of the detector array. For the coldest filter, the niobium has been currently the selected material for the mesh to avoid any residual magnetic field that may affect the TES sensors and SQUID amplifiers. Stainless steel meshes are also plated with a 5 μm gold layer to fully absorb fluorescent iron emission lines due to background particle collisions. The complete structure is then fixed to a suitable metallic frame.

Polyimide, mainly commercially sold with the trademark KAPTON® [170], is a polymer developed by DuPont industries whose chemical name is poly (4,4'-oxydiphenylene-pyromellitimide), and its chemical formula is given in Figure 5.1.

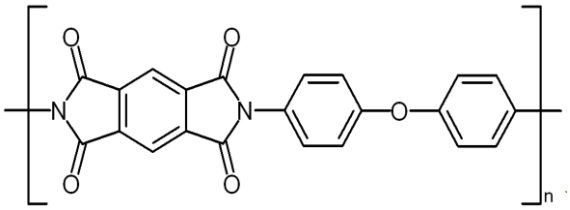

Figure 5.1 - KAPTON chemical formula.

The polyimide is used very advantageously in space applications [171, 172] due to its high performing characteristics [173]. In particular, this material shows a very high mechanical resistance in a wide temperature range (-269 ÷ 400 °C) [173] and a high X-ray transmission [174].

SAE 304 stainless steel is an austenitic Cr-Ni alloy, characterized by 200 GPa Young modulus [169], very suitable for mesh fabrication able to fully satisfy the specification on filter mechanical features (see below in this par.). Niobium is a soft and ductile metal, with 103 GPa Young modulus [169], that has no spontaneous magnetic properties. For this reason, the mesh of the coldest filter, close to the detector, will be fabricated using niobium, so the static magnetic field application on the latter is avoided [168].

The location of the thermal filters with respect to the focal plane and their associated diameter following the X-ray beam aperture from the telescope and the modulated X-ray calibration sources have been subject to repeated design change during the mission development phase A. Here, I discuss, the design of the filters presented to ESA at the Instrument Preliminary Requirement Review at the end of phase A. Such Athena X-IFU baseline filters have a circular shape, with clear aperture diameters ranging from 26 to 100 mm; their hexagonal meshes have different pitches, ranging from 2 to 5 mm, with rectangular wire cross-sections, whose dimensions are 30 mm (width) x 60 mm (thickness) for the 26 mm and 56 mm diameter filters, and 65 mm (width) x 130 mm (thickness) for the larger diameters ones. In Figure 5.2 the photo of a sample filter with a 30 mm diameter is reported.

A set of five filters, named by the operating temperature in Kelvin as TF0 (operating at 0.05 K), TF2, TF30, TF100, TF300, with 26, 56, 76, 88, and 100 mm diameter, respectively, mounted as a stack, will constitute the complete thermal filter assembly for the X-IFU system. In particular, the filters TF0 and TF2 are part of the Focal Plane Assembly (FPA) while the larger and outer filters are part of the so-called Aperture Cylinder (AC) of the Dewar (Figure 5.3). The X-ray transmission values

at specific photon energies of the stack, including molecular contamination, according to the X-IFU scientific requirements is reported in Table 5.1.

Related to IR attenuation required by the filter stack, there are mainly two design specifications:

- the radiation heat load on the cold stage from warm surfaces has to be at least two orders of magnitude less than the sum of the conductive contribution and the dissipated sensor bias power;
- the photon shot noise contribution at the detector resolution has to be less than 0.2 eV FWHM.

About RF attenuation, the specification requires that both TF2 and TF300 filters, that are installed in related Faraday cages, have to attenuate the RF radiation at least 30 dB in the range 30 MHz ÷ 18 GHz.

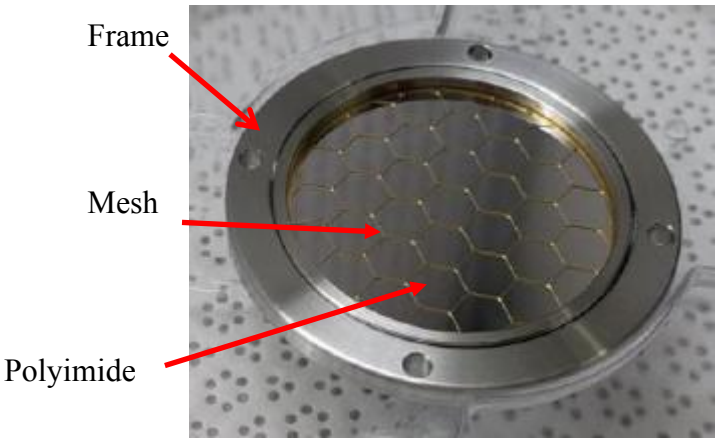

Figure 5.2 - Photo of an Athena X-IFU demonstration filter sample with 30 mm aperture diameter. The thin film is polyimide 45 nm thick coated with 30 nm of Al, and the hexagonal mesh with 5 mm pitch is SS plated with gold. Mesh wires have a section of 65 μm (width) x 130 μm (thickness)

Furthermore, the specification on mechanical features demands filters to resist:

- to the differential pressure load of 1 mbar;
- to mechanical vibrations at the launch;
- to a reasonable number of thermal cycles.

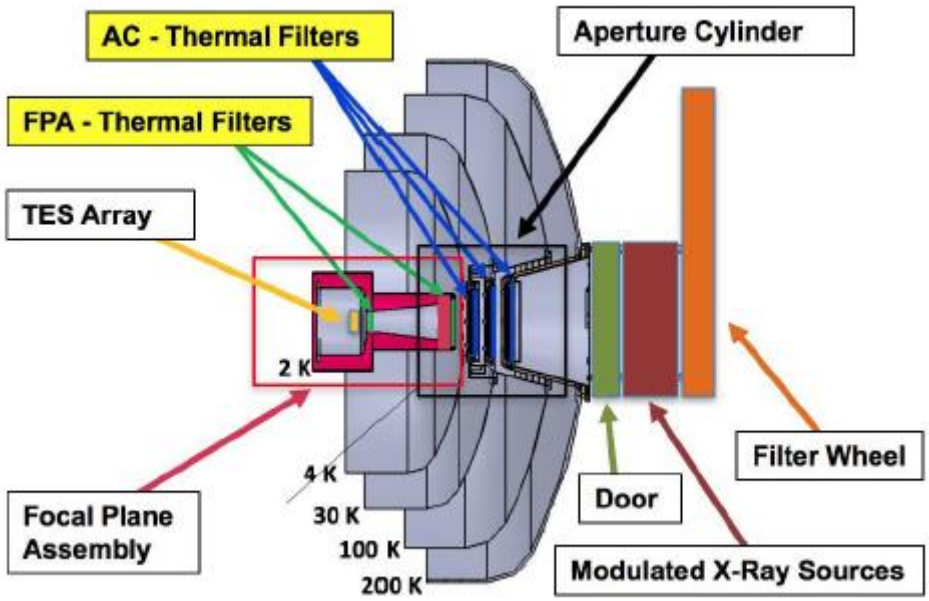

Figure 5.3 - X-IFU detector cooling system (DCS) schematic, showing the thermal filters and the aperture cylinder.

Table 5.1 - X-ray transmission values at different energies of the whole X-IFU thermal filter stack, including molecular contamination, according to the scientific requirements.

Energy (keV)	Transmission
0.35	0.21
1	0.76
7	0.9
9.5	0.9

Here, reported filter specifications and structure have to be considered as referred at the present work time, since they will be optimized changes during the Athena design development.

Silicon nitride filters

Silicon nitride filters are being developed as a possible alternative with respect to polyimide ones for future space missions.

Silicon nitride is a crystalline material that can have three different crystallographic phases, most common of which, α-Si_3N_4 and β-Si_3N_4, have trigonal and hexagonal structures, respectively. It is highly mechanically resistant in a wide temperature range, and has 310 GPa Young modulus [175].

Such filters are made of a thin (40 – 150 nm thickness) Si_3N_4 membrane coated with 15 ÷ 30 nm aluminum layers on one or both sides; two filter series were fabricated by AMETEK (Finland), according to the following structures:

C2 series - 15 nm Al/40nm Si_3N_4/15 nm Al
C3 series - 10 nm Al/20nm Si_3N_4/10 nm Al

In many samples the membrane is also supported by a silicon mesh. Filters are mounted in TO8 frames, as depicted in Figure 5.4.

Figure 5.4 - C2-1 filter mounted on a TO8 frame. The clean aperture of the filter is 8 mm.

The filter characterization activity performed so far has been mainly aimed towards the mechanical and electromagnetic property evaluation for Athena X-IFU baseline filters, while it concerned radiation damage effects for Si_3N_4 filters. In the next paragraphs, the performed characterization activity will be described in detail.

5.2 Mechanical characterization of X-IFU filters

The mechanical characterization of two TF0 and TF2 representative filters was carried out to evaluate both the filter deformation under 1 mbar static pressure and the stress causing the maximum deformation before filter failure; The tests also allow comparing the expected performances of the theoretical design with the experimental results.

This activity was performed by using an optical microprofilometer installed in a class 10000 cleanroom at the INAF-OAPa XACT laboratory (Figure 4.10 chap. 4). This system was described in detail in paragraph 4.5; for this application, the static sample pressurization system (Figure 4.11a) was employed.

Samples

The tested filters, named Athena-01-3-11-Rev-A4-Exception Nb (sample n.1) and Athena-01-3-11-Rev-A4 D57 S/N #2 (sample n.2), both with 57 mm internal diameter, are made of polypropylene stretched foil (Basf Novolen 1302L) whose thickness is 600 nm, coated with a 40 nm thick titanium layer; the polymer is supported by a SS 304 honeycomb mesh with 97% nominal transmission, with a different geometry for the two samples, as described in Table 5.2.

Table 5.2 - Mesh features for samples n.1 and n. 2.

Sample	Mesh material	Mesh pitch (mm)	Arm section (thickness x width) (μm^2)
N.1	Niobium	2	50 x 30
N.2	Stainless steel AISI 304	2	60 x 30

First, these two samples were employed to develop the static pressure characterization procedure for Athena filters, as these ones are very delicate and expensive.

Test procedure

In order to perform static pressure tests, a suitable preliminary procedure as to be followed:

1) Sample mounting on the sample holder.
   The optical profilometer can test circular, up to 100 mm internal diameter filters, and smaller, hexagonal shaped ones; in order to apply the test pressure, they are mounted on *ad hoc* filter holders, placed on the x-y-z micro-positioning system, in which the pressure sealing is guaranteed by an o-rings.
   Before starting tests, it's necessary to install the right holder, to clean the o-ring removing any dust particles, and to fix the filter to test to the holder by proper screws.

2) Pressurization system water filling.
   The pressurization system operates by providing air pressure according to the water level difference in the two A and B arms when the exit pipe is closed (Figure 5.5). The pressure resolution is 0.1 mbar, given by the 1 mm minimum water level difference that can be read.
   To perform tests, we initially decide the pressure to apply and slowly pour water to obtain the related level difference (1 mm of water difference corresponds to 0.1 mBar of pressure).
   Then the filter sealing to the holder has to be checked by observing the membrane deformation for several seconds. In case of pressure leak, the filter must be unmounted and checked together with the sample hoder and o-ring before mounting it again.

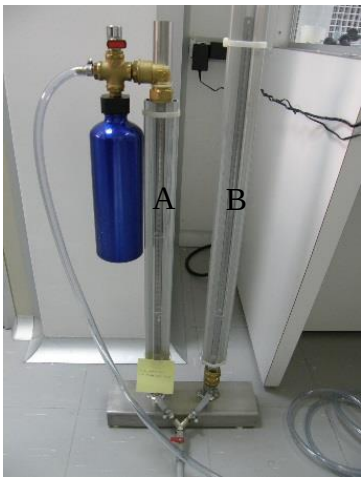

Figure 5.5 - Optical profilometer pressurization system.

3) Optical profilometer parameter setting.
   The different system parameters have to be set to obtain the best results; in particular, as filters have a highly reflecting surface, "reflecting surface" mode has to be chosen; also, translation speed has to be set as a compromise between test resolution and time; a good value is 1 mm/s.

4) Measurement start sample positioning.
   By the G-code sender module installed in the control computer, the micro-positioning system has to be actuated so the sample is placed with the laser spot hitting the measurement start point.

5) Laser spot focusing.
   Before starting measurements, the laser spot has to be focused by using the manual displacement control (z axis) of the laser holder.

6) Sample positioning at a measurement stabilization point.
   To reduce measurement errors it's useful to begin both micro-positioning system actuation and data acquisition before the real measurement starting point, in particular to reduce mechanics tolerances. So, sample has to be placed in a suitable position according to previous considerations with respect to the laser spot by G code commands.

7) Measurement line programing.
   By G code commands it's possible to decide the profile acquisition path for a simple line scan; by repeating measurements in different lines a complete data array for each filter can be obtained.

8) Measurement execution.
   To perform profile measurements, data acquisition by the micro-profilometer software interface has to be started soon after the micro-positioning system actuation; the height data are automatically acquired and stored until the end of the programmed path.

During acquisitions it's useful to check no pressure failure happens; in this case the profile acquisition has to be repeated after having mounted again the filter.

<u>Static pressure tests on samples</u>

The two interested samples were tested at static pressures in the range 1 ÷ 10 mbar; the surface profiles were acquired along the filter diameters [176].

In Figure 5.6 the deformation profiles of filters n.1 and n.2 under 9 mbar pressure are reported.

The different profiles of Figure. 5.6 are due to different Young modules for the two filter meshes (105 GPa for Nb, 210 GPa for AISI 304) and different mesh thicknesses (50 μm and 60 μm respectively); this causes a greater deformation for sample n.1. Vertical bars are given by mesh arms, and their periodicity in the mesh is verified; the arms appear as segments due to their width with respect to the measurement scale. The spikes are produced by the different laser reflections of the mesh arms and the titanium layer coating the polyimide membrane when it passes on one arm edge, as the laser spot is 16 μm size, about half-width of the arms.

These measurement results allow to state the developed procedure for static pressure tests on Athena, such procedure may be used for the testing prototype filters for the next characterization.

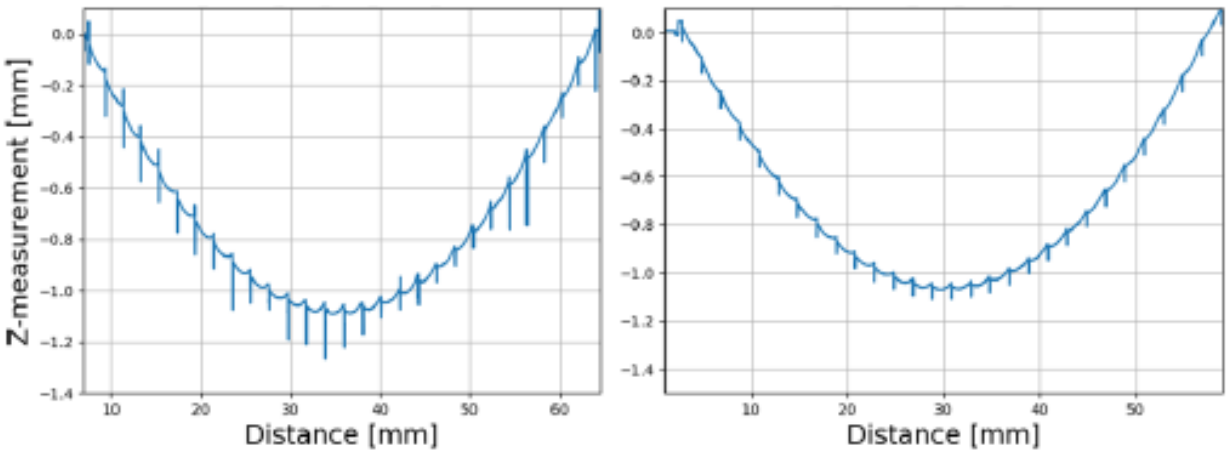

Figure 5.6 - Deformation profiles of filters n.1 (left panel) and n.2 (riight panel) under 9 mbar static pressure.

5.3 Radio frequency shielding of X-IFU filters

The aim of this activity is to evaluate the shielding effectiveness, or RF attenuation, of TF2 and TF300 filters, to verify if they satisfy the Athena RF attenuation specifications (par. 6.1).

At this purpose, three different waveguide setups are used [177], performing experiments in the lower frequency band (0.5 ÷ 3 GHz) at the OAPa-XACT laboratory, and in the upper one (2 ÷ 20 GHz) at the Dipartimento di Ingegneria of the Università degli Studi di Palermo.

Tested samples

Radio frequency attenuation tests are performed on *ad hoc* samples to distinguish the attenuation contribution of the thin aluminum layer coating the polyimide foil and the hexagonal mesh. The used samples are:

- 100 μm thick Adwill D-675 tape coated with different thickness (10 ÷ 40 nm) aluminum layer (or with no metal coating as a reference), mounted on a 100 mm diameter copper ring frame (Figure 5.7 left);
- a copper, hexagonal mesh, fabricated on a FR4 (fiberglass reinforced resin) support; the mesh features are: 4 mm pitch; 0.2 mm arm width; 35 μm arm thickness. The support is mounted on a 100 mm diameter aluminum ring, with 56 mm aperture diameter (Figure 5.7 right).

Several filter structures could be obtained by mounting on the two sides of the same 3 mm thick aluminum support the mesh and, time by time, one different thickness aluminum layer.

Test equipment

For the sample characterization in the low frequency band (0.5 ÷ 3 GHz) a 25 cm diameter waveguide, built in house and depicted in Figure 5.8, is used.

The system is made of a cylindrical metal waveguide which, at one end, is closed with an antenna installed at its center, while, on the other side, a sliding wall, that can be manually moved, supports another antenna in the same position. By moving this wall, the length of the cavity can be varied to excite resonances for different radiation modes at different frequencies in the range of interest.

Installed antennas can be coaxial or L-shaped ones. The filter to test is mounted in a suitable holder, placed at the middle of the waveguide, but that can be manually translated.

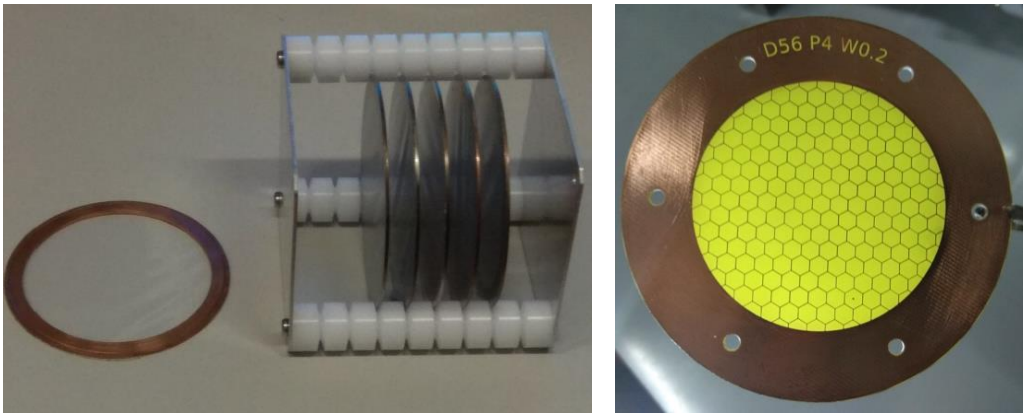

Figure 5.7 - Radio frequency attenuation test samples; a) Adwill D-675 tape coated with different thickness (10 ÷ 40 nm) aluminum layer (or no coating as a reference, on the left); b) hexagonal mesh fabricated on a FR4 support (right).

The output is sent to an Agilent N9320B spectrum analyzer, generating also the input radiation, to examine output waveforms and to detect excited resonances; transmission curves can also be traced.

Instead the tests in the high frequency band (2 ÷ 20 GHz) are performed using the setup depicted in Figure 5.9.

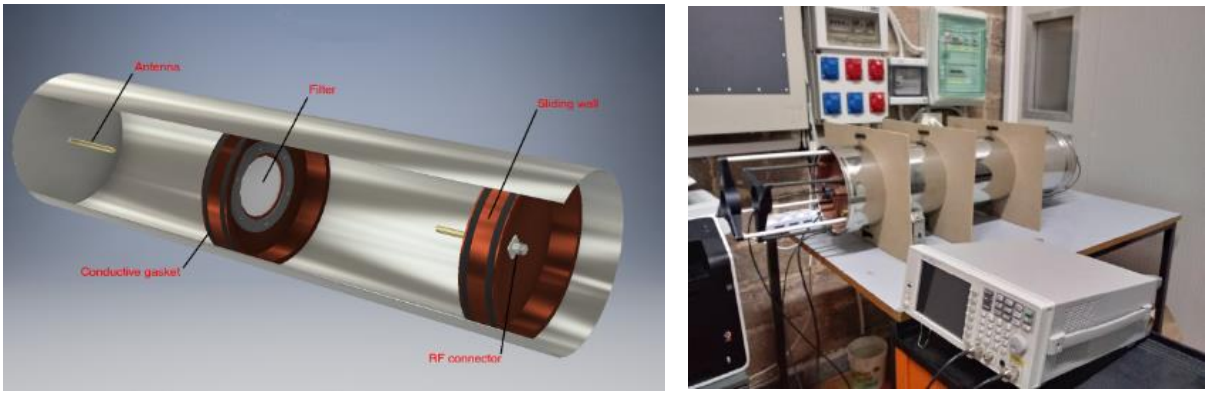

Figure 5.8 - Low frequency band (0.5 ÷ 3 GHz) test setup: schematic (left); photo (right).

Figure 5.9 - High frequency band (2 ÷ 20 GHz) test setup: schematic (left); photo (right).

This setup is based on a 10 cm diameter, metal waveguide whose length is 900 mm, with both sides open; the transmitting and receiving antennas are mounted on two aluminum sliding walls that can be manually displaced inside the waveguide, to change the internal cavity length. On the lateral surfaces of this walls conductive gaskets are mounted to ensure good electrical coupling with the waveguide. The cut-off frequencies for this one are 1.76 GHz and 2.29 GHz for TE_{11} and TM_{01} modes, respectively[2].

The antennas of the waveguide are connected to the two ports of a Keysight 5232A PNA-L microwave vector network analyzer operating in the frequency range 300 kHz ÷ 20GHz.

A third system, custom built at OAPa-XACT laboratory, is also available to perform RF attenuation measurements in an environment more similar to the two Faraday cages hosting thermal filters TF2 and TF300 in the present cryogenic Athena Dewar design. Two RF filters can be contemporarily mounted inside this setup.

The schematic of this system is reported in Figure 5.10; the photo of the setup connected to the Agilent N9320B RF generator/spectrum analyzer is shown in Figure 5.11. This system is presently deployed for testing filters in the range 0.5 ÷ 3 GHz.

Test activity

Filter testing was performed according to the mode stirring method, that is based on the excitation of several radiation modes in a cavity. Details on this method are reported in [177].

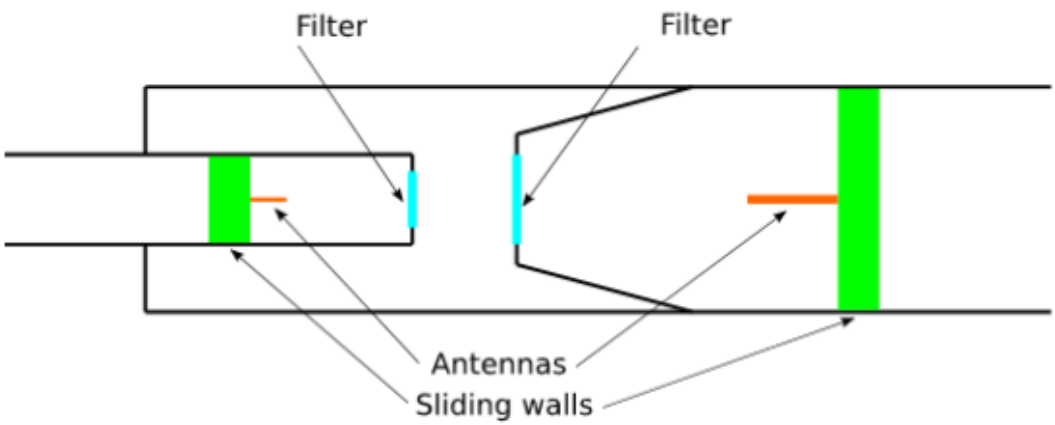

Figure 5.10 - Schematic of the system to perform RF attenuation measurements with TF2 and TF300 in an environment similar to the present X-IFU cryostat design.

[2] Transverse magnetic (TM) modes, i.e. electromagnetic waves with the magnetic field laying only on the plane normal to the chamber axis (transverse plane), and transverse electric (TE) modes, with electric field only in the transverse plane, are numbered with subscripts indicating the number of azimuthal and radial variations.

Figure 5.11- Photo of the system sketched in **Errore. L'origine riferimento non è stata trovata.**.

The mode stirring method allows to statistically evaluate the filter RF attenuation independently by the specific mounting environment, by applying several electromagnetic modes to the filters.

RF attenuation measurements were performed by the frequency stirring mode measuring the maximum power transmission through the filter.

First, only the aluminum coated filters are tested, and measurements with both blank (without any filter), only substrate (uncoated tape filter), and close configurations (with a 3 mm thick aluminum disk placed as a filter) were executed as references (Figure 5.12).

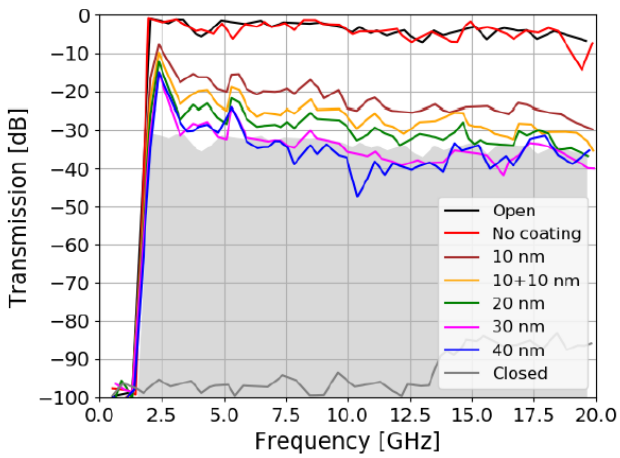

Figure 5.12 - RF attenuation measured for a set of filters with different thickness of aluminum coating (without mesh). Superimposed are the measurements performed with closed and open aperture.

In Figure 5.12 the red line represents the transmission of an only tape filter, without aluminum coating; this shows that the attenuation contribution of the tape is negligible with respect to the metal layer. The black trace, without any filter mounted, describes the attenuation produced by the cavity; this reference curve has to be subtracted to the measured transmission in order to obtain the precise attenuation for each filter. The grey, highest attenuation line, represents the transmission behavior of a 3 mm thick aluminum disk.

As the attenuation specification for TF2 and TF300 requires at least 30 dB in the range 30 MHz ÷ 18 GHz, by Figure 5.12 it can be deduced that, with no mesh, filters with 30 or 40 nm aluminum coating, verify the assigned specification above ~ 6 GHz.

The mesh attenuation contribution was evaluated by further tests performed by mounting in the cavity the mesh together with another filter. Obtained results are reported in Figure 5.13, in which the RF attenuation of the mesh alone is given by the red trace, neglecting the tape attenuation. It can be observed a greater attenuation at frequencies lower than 7 GHz, that, summed to the correspondent values given by aluminum coated tape filters, implies that, if the dimensions of the cavity constituted by the aperture cylinder and the focal plane assembly are that specified in the present design, the combination of an aluminum layer > 30 nm coupled with a metal supporting mesh fulfills the RF requirement over the full range 30 MHz ÷ 18 GHz. In fact, frequencies below about 2.5 GHz are cut off by the cavity.

Further measurements will be performed by the third system (Figure 5.10), resembling the designed Athena cavity structure, to confirm obtained results.

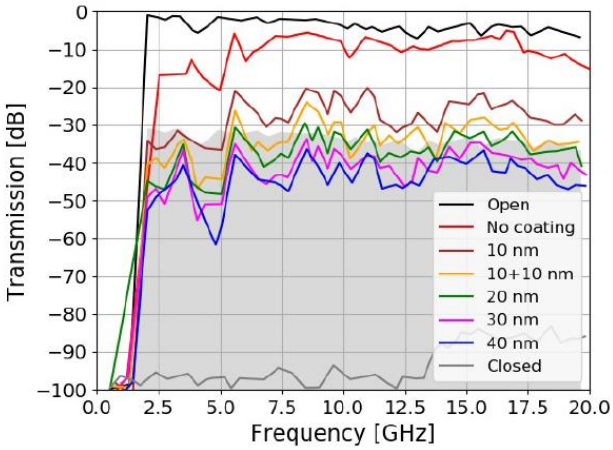

Figure 5.13 - Attenuation of the mesh alone (red curve) and together with another aluminized filter.

5.4 Radiation damage

Radiation damage is the effect (changes in structural, mechanical, electrical, optical, etc. properties) on matter due to the irradiation by energetic particles (protons, light and heavy ions, electrons, atoms, molecules). This effect is very important in space applications where energetic particles are present, whose energetic distribution includes also high energies (in the order of MeV, GeV or more).

Thermal filters are not able to effectively shield detectors by high energy particles (E > 100 keV), then it's important to know the effect of such irradiation on the mechanical, thermal, RF, and optical filter characteristics, to ensure they aren't damaged during the mission lifetime.

5.4.1 Space particle irradiation

The sun emits a complex spectrum of particles (protons, electrons, light and heavy ions) with a wide energy spread [178, 179]; a regular low energy (1eV to 10 keV) particle flux exists, that is the solar wind, moving radially from the sun with about 10 particle·cm^{-3} density, but, in some periods, called solar particle events (SPEs), high intensity emissions of high energy particles (MeV to GeV)

add to the regular flux. Furthermore, outside the solar system, galactic cosmic rays (GCRs) are emitted, likely from supernova remnants; they are constituted by about the same particles as the solar emission, and their energies span in the range 10^8 to 10^{20} eV; their flux is constant and modulated on Earth by the solar activity [180, 181]. Both sun emission and GCRs are dangerous both for human beings working in space and for onboard spacecraft electronics and solar panels.

Another source of space radiation comes from the radiation belts, that are protons and electrons trapped around planets with magnetic fields, like the Earth [180, 181]; they can damage both onboard electronics and solar panels.

For the Earth, the radiation belt is divided into two zones [181]:

- the inner one, extending from some hundreds kilometer height to about 6000 km, mainly populated by high energy protons (some tens MeV) and electrons (1 to 10 MeV);
- the outer belt, extending up to about 60000 km, is mainly rich in high energy electrons.

Due to the above described effects, many theoretical studies and several experiments, both in space and ground laboratories, were performed to evaluate consequences of particle irradiation on both thick layer and thin films of different electronics and space application materials.

As a background for the experimental characterization of filters with respect to the radiation damage, the scientific literature related to both polyimide and silicon nitride films was reviewed.

Polyimide films

Several polyimide films with different thickness were irradiated by protons, both light and heavy ions, by electrons in several facilities [182, 183, 184, 185, 186], to simulate operating conditions during space flights. The obtained samples were then analyzed by atomic force microscopy (AFM), SEM, UV-Vis-IR spectroscopy, micro-Raman scattering, X-ray photoelectron spectroscopy (XPS), and other techniques.

The investigation of the irradiating polyimide films with protons in the energy range from keV to MeV allows to conclude as follows:

- the tensile strength increases for an irradiation dose corresponding to 3 years flight time, then it decreases [187]; a similar trend holds for the elongation [187];
- the hardness increases with increasing fluence [183];
- the Vis-NIR band spectral transmittance decreases with the increasing fluence [184].

However, the fluences employed in above experiments are greater than the ESA qualification value for Athena ($1.2 \cdot 10^{10}$ cm^{-2} @ 1 MeV).

Other effects due to high mass and energy particles (light and heavy ions, atoms) were observed:

- the irradiation with so-called swift heavy ions (SHI), ions whose energy is greater than 1 MeV, deteriorates polyimide, by producing internal disorder [188] and modifying its optical properties, as evidenced by the redshift of the UV-Vis-IR transmission edge [189];
- the irradiation with oxygen atoms, at increasing fluences in the low earth orbit (LEO) range, provokes: increase of sample surface roughness, thickness reduction, both tensile strength and elongation decrease [190].

The electrons also modify the polymer, and in particular they affect the optical properties; in fact, the spectral reflectance reduces with increasing fluence in the wavelength range 500 to 1200 nm [191].

Above macroscopic effects can be microscopically explained as the particle irradiation in polyimide causes polymeric chain scission, bond breaking, cross-linking, gas release (N, O, H), and free radical production [191, 192].

Silicon nitride

Silicon nitride was very diffusely studied related to heavy ions irradiation, which are the most dangerous particles for microelectronic devices.

When high energy SHIs impact Si_3N_4 samples, they penetrate the material producing, around their tracks, fused matter pipes whose diameter is some nanometer and in which Si-N bonds are distorted [193]; this effect was explained by the thermal spike model [194]. Also, high mass, lower energy (hundreds of keV) ions produce ion tracks whose length is about 10 ÷ 20 nm [195]; as these have thicknesses comparable to those of thermal filters, it's necessary to account for their effects.

Another consequence of ionic irradiation is the surface swelling [196]; at first, the surface height steeply grows with increasing ion fluence, but, after a threshold value, it saturates at a limit value.

Moreover, ion irradiation changes optical properties of silicon nitride:

- optical transmissivity in near UV – Vis – NIR bands changes depending on the ion specie [197]; this can be explained by supposing different ions provoke various chemical lattice modifications;
- refractive index in Vis-NIR bands varies depending on ion specie, and decreases with increasing irradiation fluence; its variation can be greater than 10% [196], and this is due to chemical bond changes that reduce crystal density.

Generally speaking, all above effects are caused by the breaking of Si-N bonds in the crystal due to ion collisions; two lattice damage mechanisms were identified, the nuclear type and the electronic one, and they verify depending on ion specie and energy [193].

5.4.2 Irradiation of Si_3N_4 samples

Radiation damage characterization activity was focused on silicon nitride films mounted on TO8 frame; both C2 and C3 series samples have been irradiated. A review of sample characteristics, described in par.5.1, is reported in Table 5.3.

Table 5.3 - Irradiated sample characteristics

Serie	Layer thickness		
	Upper Al layer	Si_3N_4 layer	Lower Al layer
C2	15 nm	40 nm	15 nm
C3	10 nm	20 nm	10 nm

Tested samples were irradiated by 1 MeV protons with different fluences, according to Table 5.4, at the Van der Graaf accelerator of the Johann Wolfgang Goethe-Universität Frankfurt am Main (Figure 5.14). The maximum proton energy available at this facility is 2.5 MeV. Two types of detectors are used to detect ions: micro channel plate and silicon surface barrier.

Table 5.4 - Irradiated filters (Cx-y) and related fluences relative to the Qualification Fluence (Q.F.) specified by ESA ($1.2 \cdot 10^{10}$ cm^{-2} @ 1 MeV).

Filter	Irradiation fluence (I.F.)
C2-4/C3-12	$\backsim 1 \cdot 21 \cdot 10^{9}$ [cm^{-2}] ($\backsim$0.1 Q.F.)
C2-5/C3-13	$\backsim 1 \cdot 21 \cdot 10^{10}$ [cm^{-2}] ($\backsim$ Q.F.)
C2-2/C3-10	$\backsim 1 \cdot 25 \cdot 10^{11}$ [cm^{-2}] ($\backsim$10 Q.F.)
C2-3/C3-16	$\backsim 1 \cdot 26 \cdot 10^{12}$ [cm^{-2}] ($\backsim$100 Q.F.)
C2-7/C3-15	$\backsim 4 \cdot 5 \cdot 10^{12}$ [cm^{-2}] ($\backsim$300 Q.F.)

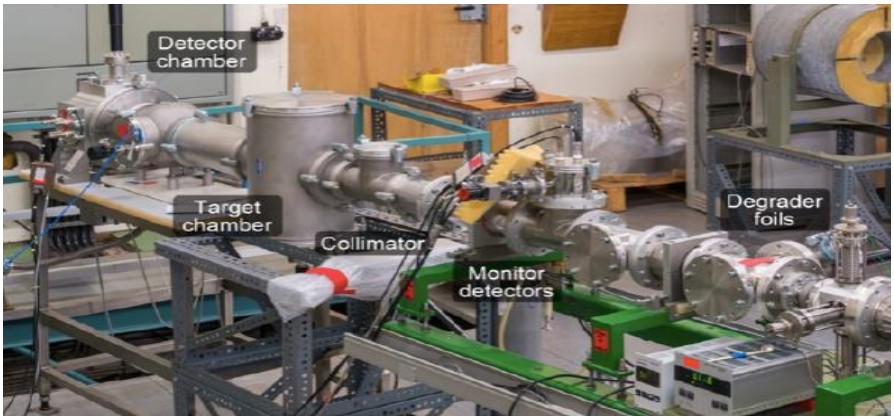

Figure 5.14 - Van der Graaf accelerator at the Johann Wolfgang Goethe-Universität Frankfurt am Main

After irradiation, the characterization activity was developed.

5.4.3 Scanning electron microscope observation

Filters in TO8 frame were observed by a FEI Quanta 200F SEM, at the Dipartimento di Ingegneria of the Università di Palermo (UNIPa). A detail of C2-3 sample placed in the SEM sample holder is illustrated in Figure 5.15.

In order to study the effect of proton irradiation on sample surfaces, two filter were analyzed: C2-1 (pristine) and C2-3 (Table 5.3). In Figure 5.16 their 100000 X magnification surface SEM images are represented, respectively.

It can be observed, apart focusing difficulties due to the extremely regular surfaces, and within resolution limits of the instrument, no morphological effects appear on irradiated sample membrane, resulting of the same aspect of the other one.

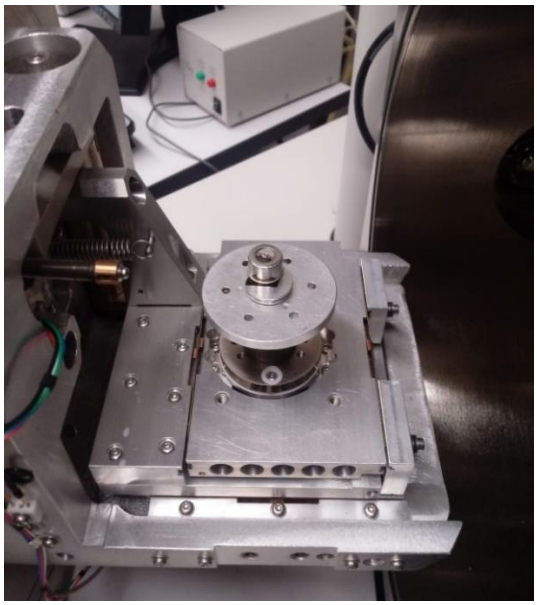

Figure 5.15 - C2-3 sample placed in the SEM holder.

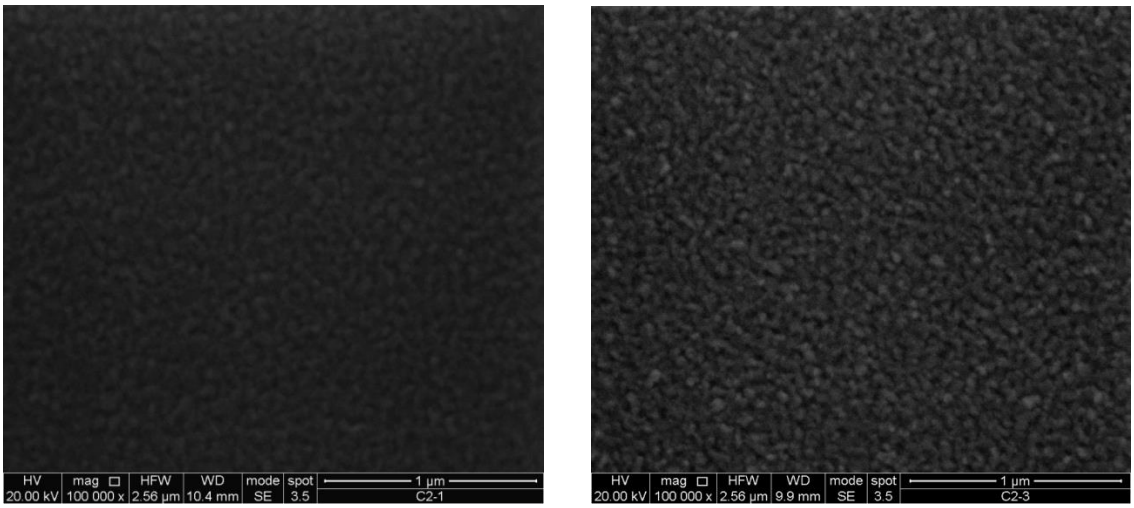

Figure 5.16- SEM images of filter surfaces: pristine C2-1 (left); 100 Q.F. irradiated C2-3 (right).

5.4.4 Atomic force microscopy observation

The same filter (C2-1 and C2-3) surfaces were also observed by a Bruker Fastscan atomic force microscope (AFM), sited at the Advanced Technologies Network (ATeN) Center of the Università di Palermo. A detail of the microscope head, with the C2-3 filter placed on the support, is reported in Figure 5.17.

Surface analyses were performed in air in soft tapping mode, by using the Bruker Fastscan A wafer A01405 n.09 tip. The silicon mesh appears below both the silicon nitride membrane and the upper aluminum layer.

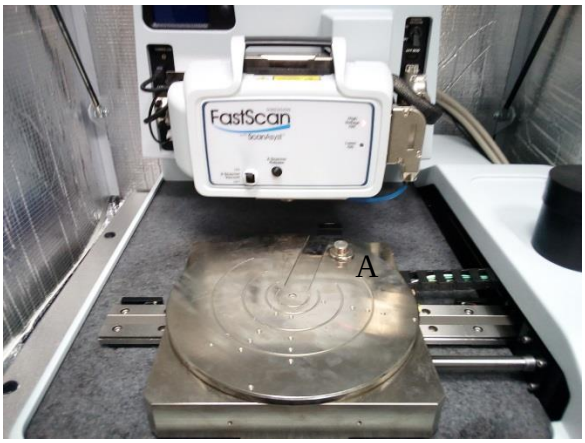

Figure 5.17 - Detail of the atomic force microscope head, with the C2-3 filter (A) placed on the sample holder.

Wide areas (8 x 8 μm^2) for each sample were scanned to acquire surface morphology features by applying parameters reported in Table 5.5; they were chosen to obtain the best scan results after having performed several preliminary tests.

The AFM images of C2-1 (pristine) and 100 Q. F. irradiated TO8-C2-3 samples are shown in Figure 5.18. The surface seem quite similar, regular, and without any defect, within the detection limit of the instrument.

In order to characterize the surface morphology of scanned samples both the height density and the RMS roughness were evaluated by the Gwyddion software [198]. The calculated sample RMS roughness values S_q [pm] are given in Table 5.6.

Table 5.5 - AFM parameters for filter scans.

Scan size	8 μm
Aspect ratio	1
X offset	0 nm
Y offset	0 nm
Scan angle	0°
Scan rate	1.05 Hz
Tip velocity	18.6 μm/s
Samples/line	1536
Lines	1536
Integral gain	0.5
Proportional gain	2.5
Amplitude setpoint	255 mV

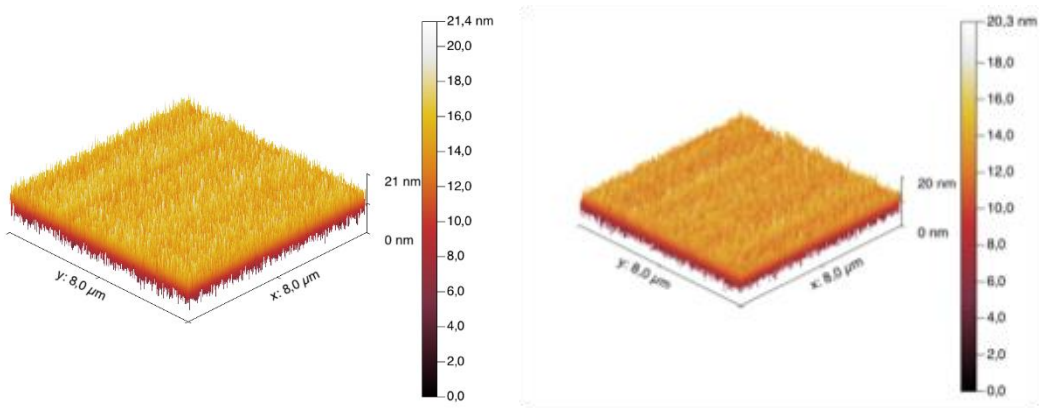

Figure 5.18 - AFM images of C2-1 pristine sample (left panel) and 100 Q. F. irradiated TO8-C2-3 (right panel).

Table 5.6 - Sample RMS roughness

Sample	S_q [pm]
C2-1	299.7
C2-3	274.7

Due to very small differences of RMS roughness values (25 pm) between pristine and irradiated filters, within the equipment resolution limit, it wasn't clear if this effect is due to tolerances in the filter fabrication process or to irradiation, that could reduce the roughness; to solve the question, another pristine sample, the C2-6, was tested.

Height distribution histograms, with related widths, are reported in the left, center, right panels of Figure 5.19.

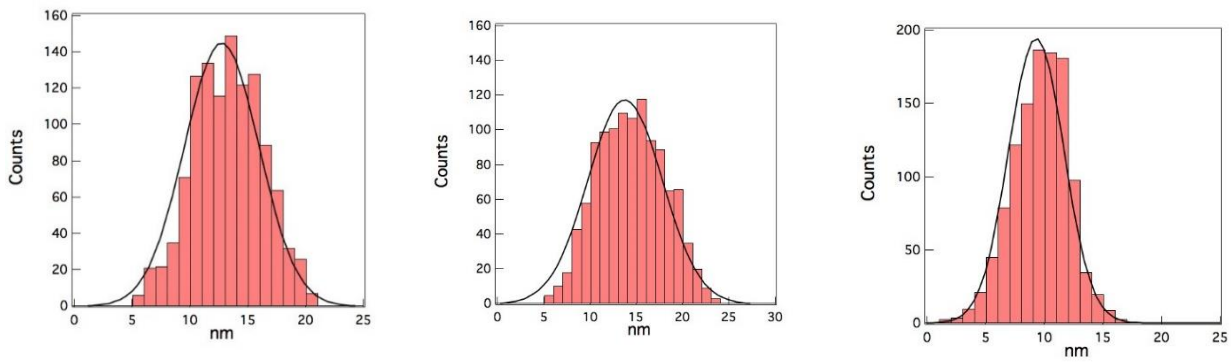

Figure 5.19 - Height distribution histograms for pristine TO8 C2-1 (left), pristine TO8 C2-6 (center), 100 Q.F. TO8 C2-3 (right); related widths are 4.57 nm, 5.68 nm, 3.33 nm, respectively.

By visually inspecting histograms in Figure 5.19, it's deduced that 100 Q.F. TO8 C2-3 height distribution shows a slightly more negative skewness [199] and a higher kurtosis [199] values with respect to pristine samples. The first feature indicates that valleys are more present with respect to peaks on the surface [200]; the second one implies less spreading in the height distribution, due to irradiation.

From this data it's possible to conclude that a small roughness reduction is due to strong irradiation, but fabrication tolerances produce similar roughness differences among pristine filters themselves.

5.4.5 UV-Vis-IR spectroscopy

The UV-Vis-IR spectroscopy characterization of several filter samples was performed using a Jasco V770 optical spectrograph at the UNIPa Dipartimento di Fisica e Chimica (DiFC).

Preliminarily both a suitable filter holder and a beam delimiter were custom designed and fabricated to ensure samples were mounted always in the same position and interested by the same spot size. Also, several tests were firstly performed to evaluate best measurement parameters, that are reported in Table 5.7; the examined samples are listed in Table 5.8.

Table 5.7 - Best UV-Vis-IR spectroscopy measurement parameters

Parameter	Value or range
Wavelength range	190 – 3200 [nm]
Wavelength scan rate	400 [nm/min]
UV-Vis bandwidth	1 [nm]
IR bandwidth	4 [nm]
Pitch	0.5 [nm]

Table 5.8 - Measured samples

Sample	Description
C2-1	Pristine
C3-9	Pristine
C2-5	1 Q. F. irradiated
C3-13	1 Q. F. irradiated
C2-2	10 Q. F. irradiated
C3-10	10 Q. F. irradiated

Each test was repeated many times to reduce noise influence by averaging obtained spectra; it was also observed that noise increased excessively at wavelength greater than 2800 nm, so it was decided to not include the 2800 – 3200 nm range of each spectrum during data elaboration to evaluate filter performances.

In order to calculate absolute filter transmission values and verify the spectrophotometer light source emission intensity trend with time, several blank spectra (with the dummy filter inserted or without any filters) were collected at the start of each sample measurement session.

Acquired spectra are reported in Figure 5.20 a to f and Figure 5.21 a to f; some main differences appear between C2 and C3 filter series, both in pristine or irradiated ones (Table 5.9).

For both series, otherwise, it was observed that:

- the minimum transmission is very low, less than 1% for both pristine and irradiated C3 series filter in the about 1250 – 1800 nm wavelength field, and about 0.7% near 1500 nm; less than 1.5% in the about 1000 - 1800 nm range for both pristine and irradiated C2 series filters, with about 0.6% minimum near 1250 nm;
- the transmission strongly increases for every filter for wavelength greater than 2500 nm.

Table 5.9 - Main filter feature differences

Serie	Sample	UV transmission peak position (nm)	UV transmission peak amplitude (%)
C2	C2-1 (pristine)	304	28.362
	C2-5 (1 Q. F.)	304	12.173
	C2-2 (10 Q. F.)	299	13.446
C3	C3-9 (pristine)	244.5	26.630
	C3-13 (1 Q. F.)	244	26.341
	C3-10 (10 Q. F.)	239	26.418

Also, by comparing C2 series transmission spectra (Figure 5.20a, c, e and Figure 5.21a, c, e) it can be seen a clear effect of 1 MeV proton irradiation on filters; less evident modifications happen for C3 series ones (Figure 5.20b, d, f and Figure 5.21b, d, f).

Other details can be evidenced:

- in Figure 5.20c the 5 nm UV peak displacement with less than 50% transmission, for 10 Q. F. C2-2 sample with respect to pristine C2-1, is shown;
- in Figure 5.20 d the 5.5 nm UV peak displacement, with about the same transmission, for 10 Q.F. C3-10 sample with respect to pristine C3-9 is shown;
- large differences derived by small irradiation fluences for C2 series, as it can be seen in Figure 5.21a, comparing pristine C2-1 and 1 Q. F. C2-5 samples;
- C2-1 and C2-5 sample UV peaks are at the same 304 nm wavelength, and less than a half transmission can be observed for C2-5 (Figure 5.21c);
- a small (0.5 nm) peak displacement can be noted (inside red circle) between C3-9 and C3-13 UV spectra in Figure 5.21d, while heights are about the same for both peaks.

IR peaks in both 10 Q. F. C2-2 (Figure 5.20e) and 1 Q. F. C2-5 (Figure 5.21e) spectra are lower with respect to pristine C2-1 sample ones.

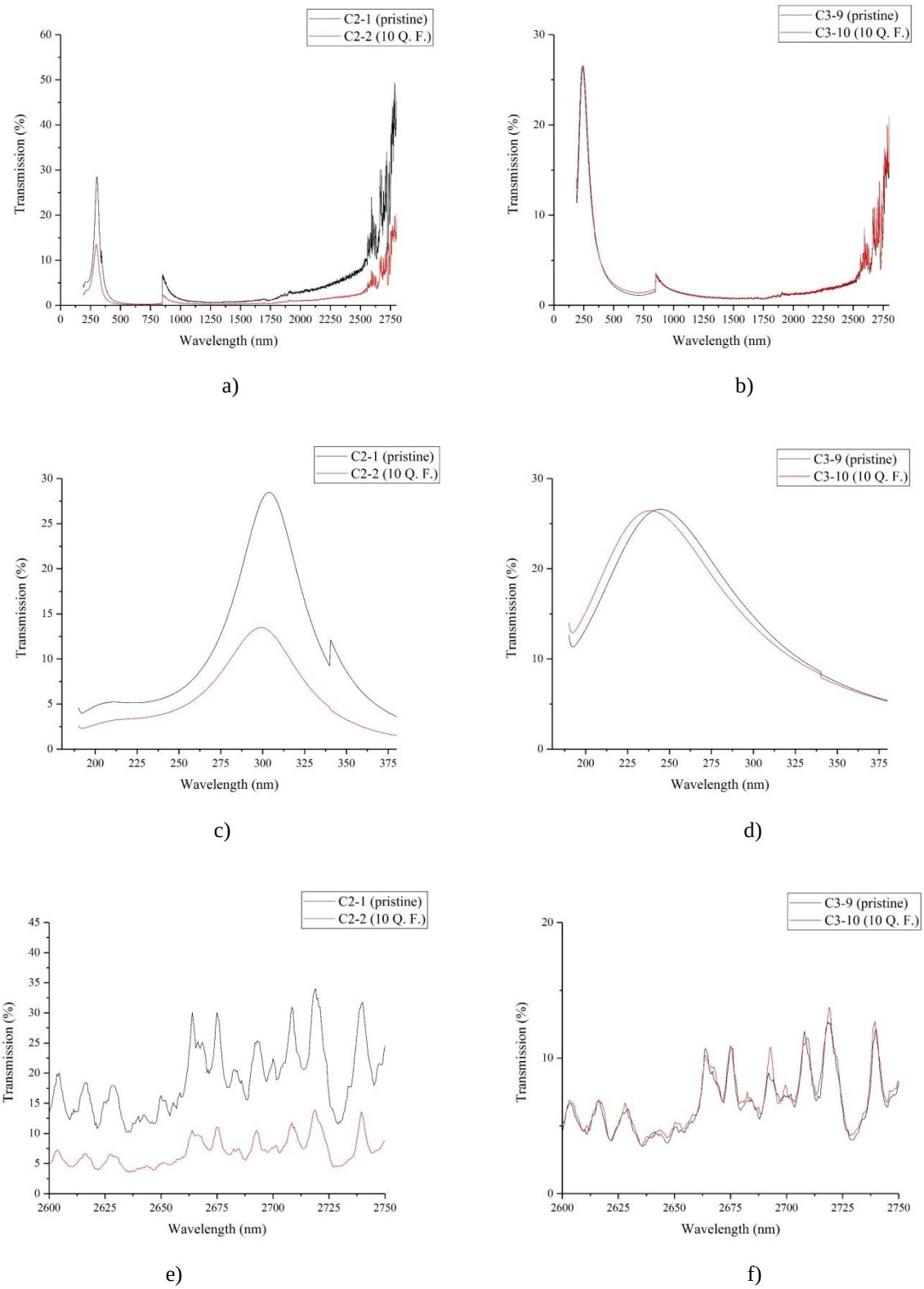

Figure 5.20 - C2-1, C2-2, C3-9 and C3-10 filter transmission spectra; a) C2-1 and C2-2 full band; C3-9 and C3-10 full band; c) detail of C2-1 and C2-2 UV spectra; d) detail of C3-9 and C3-10 UV spectra; e) detail of C2-1 and C2-2 IR spectra; f) detail of C3-9 and C3-10 IR spectra.

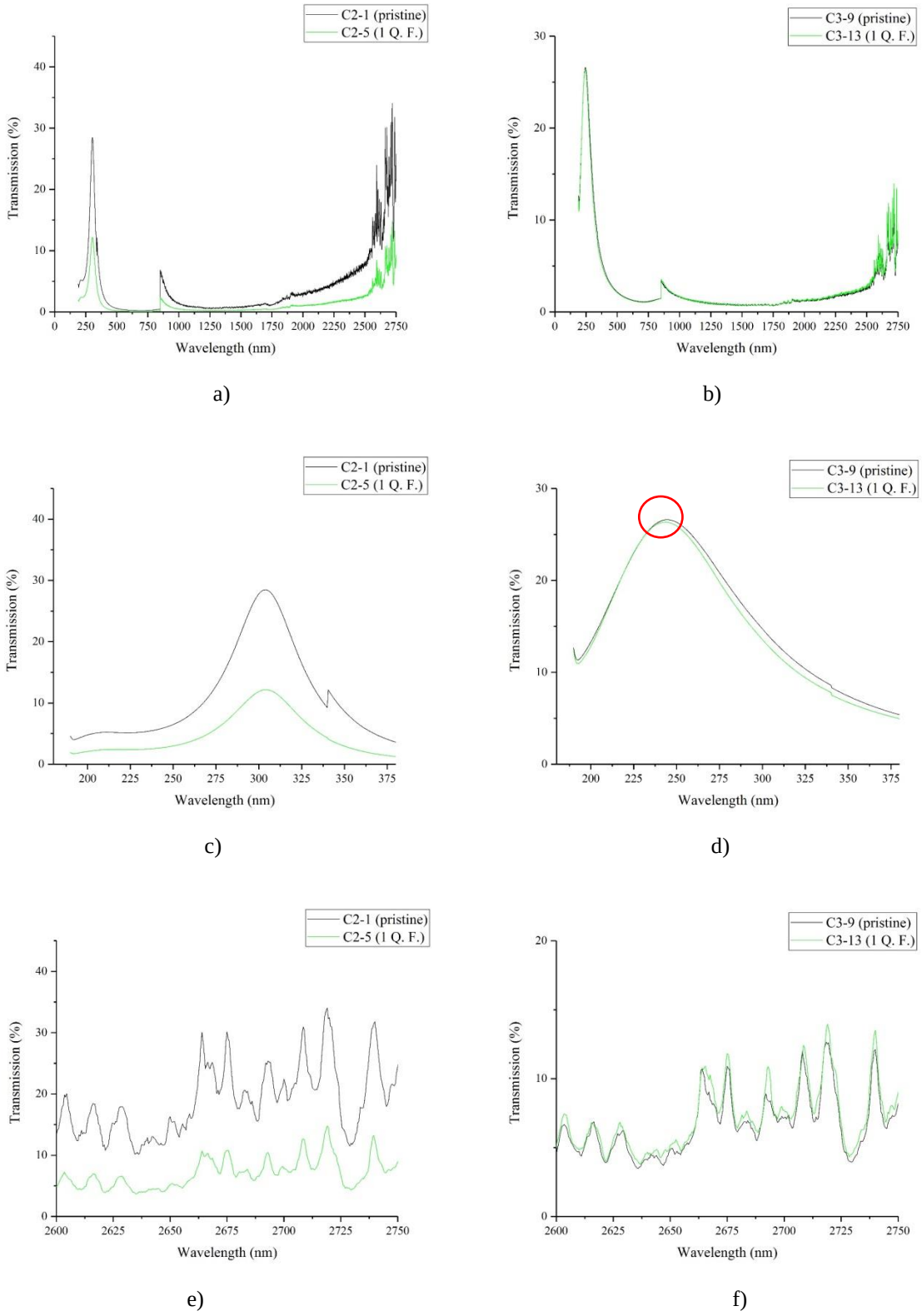

Figure 5.21- C2-1, C2-5, C3-9 and C3-13 filter transmission spectra; a) C2-1 and C2-5 full band; C3-9 and C3-13 full band; c) detail of C2-1 and C2-5 UV spectra; d) detail of C3-9 and C3-13 UV spectra; e) detail of C2-1 and C2-5 IR spectra; f) detail of C3-9 and C3-13 IR spectra.

5.4.6 X-Ray Absorption Spectroscopy

In order to evaluate the areal density of the material composition, and thickness uniformity of aluminized Si_3N_4 filters, X ray absorption spectroscopy (XAS) [201] in transmission was performed at both PTB-EUV and PTB-X-ray beamlines of BESSY II synchrotron (Berlin, Germany).

Measured samples

Measured samples with related structural characteristics are listed in Table 5.10. It can be noted C1-1 is a meshless sample; C2-2 to C2-6 ones have the aluminum coating on both silicon nitride sides, whilst C2-31 has no coating.

Table 5.10 - XAS tested samples

Sample	Si_3N_4 thickness [nm]	Aluminum thickness [nm]	Silicon mesh thickness [μm]	Open area (%)
TO8 C1-1	145	2 x 10	-	-
TO8 C2-2	40	2 x 15	15	82
TO8 C2-5	40	2 x 15	15	82
TO8 C2-6	40	2 x 15	15	82
TO8 C2-31	40	0	15	81

Facilities

The X-ray spot on the sample at PTB EUV is rectangular, with 1.2 mm width and 1 mm height; the energy range allowed in this beamline is 50 eV ÷ 1.8 keV.

Also in the PTB X-ray beamline the light source is a bending magnet, and the spot size on the sample is smaller than the previous: 0.3 x 0.3 mm^2; this beamline operates in a higher energy range (1.75 ÷ 3.6 keV).

Measurement execution and results

The energy intervals of both beamlines allow to perform measurements at main edges for filter materials, as described in Table 5.11. The measurements were performed at variable steps, strongly reducing this parameter near above edges; the transmission curves for each filter were so modeled; a comparison between pristine TO8 C2-6 and 10 Q. F. irradiated TO8 C2-2 is reported in Figure 5.22.

Table 5.11 - Main edges for filter materials

Element	Edge	Energy [eV]
Al	L	73
	L	118
	K	1560
Si	L	99
	L	149
	K	1839
N	K	402
O	K	532

From Figure 5.22 it's evident no practical differences are produced in Si_3N_4 filters related soft X-ray transmission by 1 MeV proton irradiation.

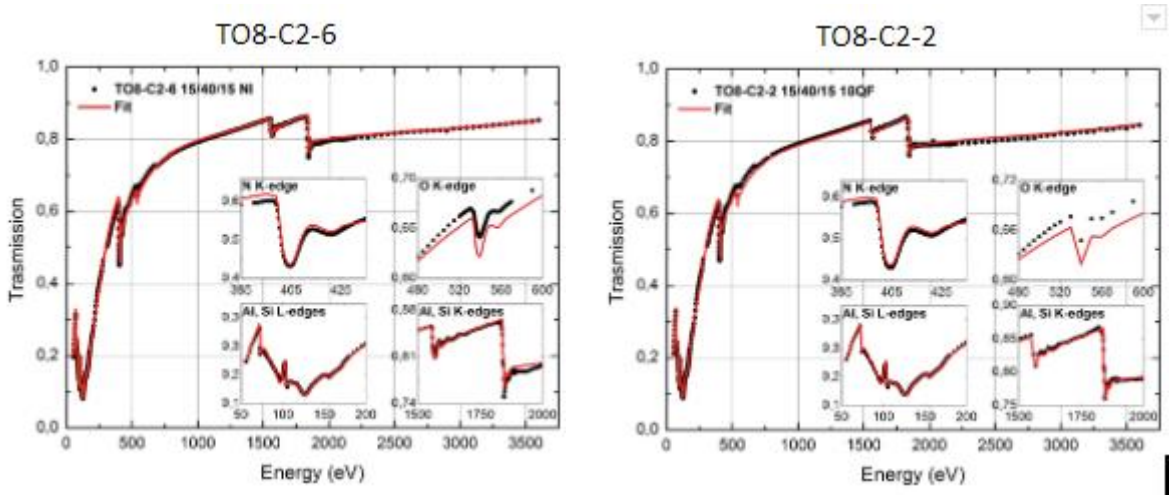

Figure 5.22- Comparison between X-ray transmission curves for pristine TO8 C2-6 (left) and 10 Q. F. irradiated TO8 C2-2 (right) filters.

5.5 Characterization conclusions

After the whole characterization activity in described fields (mechanical static deformation, RF attenuation, radiation damage), the conclusions could be stated for both polyimide and silicon nitride filters.

About the former, both the test equipment and procedure were applied, and they resulted well adequate to perform thermal filter characterization; very useful guidelines were also derived for designing thermal filter fulfilling ESA specifications.

Mechanical deformation tests under static pressure, performed on pre-assessment filters, allowed to state the filter design and test procedures are well suited for final filter characterization. Related to RF attenuation, it can be stated polyimide filters with both the 30 ÷ 40 nm thick aluminum layer and the mesh according to parameters reported in the paragraph 6.3, if mounted in a Dewar enclosure according to present Athena design, can satisfy current ESA specifications.

Referring to Si_3N_4 filters in TO8 frame, related to radiation damage tests, the comparison of measurement results obtained by different techniques applied (SEM, AFM, UV-Vis-IR spectroscopy, Raman microscopy, XAS) to characterize both pristine and irradiated filters allowed to derive useful conclusions about the irradiation effect by 1 MeV protons, with fluences also higher than the ESA qualification level. Both filter types (C2 and C3 series) were tested, in order to understand irradiation effects on both physical structures.

The first result is that, within used SEM and AFM equipment measurement limits, the surface morphology is very little smoothed by the applied irradiation, evidencing a small roughness reduction, but fabrication tolerances produce similar roughness differences among pristine filters themselves.

On the contrary, some internal structure modifications is due to proton irradiation, revealed by both UV-Vis-IR spectroscopy and Raman scattering; however, only C2 filters undergo evident changes in their optical features.

CONCLUSIONS

This thesis deals with the development of instrumentation for high energy astrophysics observations. In particular, two topics were addressed. The main topic was the development of a technique to produce thick bismuth X-ray absorbers to be employed in the fabrication of planar arrays of NTD germanium microcalorimeters sensitive to hard (up to 100 keV) X-rays. A second topic was the study of filters for shielding X-ray microcalorimeters by out of band radiation.

The work on bismuth absorbers showed that it is possible to grow very thick bismuth layers on the array of NTD germanium thermometers of X-ray microcalorimeters and a tuning of the process was carried out. This result will allow to build devices capable of observing the universe in the hard X-ray band with unprecedented energy resolution. We plan to use the guidelines developed in this work in the next fabrication processes of planar arrays of microcalorimeters.

The work on X-ray filters was mainly devoted to the study of Athena X-IFU thermal filter samples. A few filter prototypes developed for the Athena mission have been characterized with respect to mechanical robustness, optical performances and radio-frequency attenuation. The design consolidation of these filters is still in progress, yet this work has given a substantial contribution to demonstrate the compliance of the investigated technology to some mission requirements. In addition, radiation hardness has been investigated on novel filters based on silicon nitride of potential interest for future space missions.

It should be pointed out that the fabrication of fully operating hard x ray NTD Ge microcalorimeters for astrophysical applications is the long term goal of this activity. This goal requires a significant characterization activity performed at cryogenic temperature (thermometer sensitivity, read-out performance, absorber-thermometer and thermometer-bath thermal conductivity) which is demanded to future work.

APPENDIX

A.1 Main detector requirements

Detectors for X-ray radiation are featured by several parameters; most important of them are:

- *energy resolution*; it represents the detector capability to resolve photopeaks in the energy spectrum. For a monocromatic source, if the detector response presents a peak of maximum value M at energy E_0, and the peak width at M/2 is W (the full width at half maximum, FWHM), the absolute energy resolution ΔE is equal to W (eV); it's also defined the dimensionless relative energy resolution $\frac{\Delta E}{E} = \frac{W}{E_0}$;
- *energy range*; it's the energy interval in which the sensor is able to produce a signal when a photon hits it;
- *space resolution*; it's the capability to discriminate small objects that are at small distance between them, and its maximum value (best imaging) is determined by the sum of the pixel dimension and the spacing between them, called pitch;
- *quantum efficiency (QE)*; it's the fraction of incoming photons that are revealed; it's always QE < 1; it depends on both the detector operation principle and fabrication parameters;
- *detective quantum efficiency (DQE)*; it's defined as $DQE = \frac{(S/N)_{out}}{(S/N)_{in}}$, where S/N is the signal-to-noise ratio, measured at the sensor output and input respectivly;
- *sensitivity*; it's the lowest amplitude signal that can be detected by the sensor;
- *count rate*; the average rate of occurrence of events revealed by the detector; high count rate let high photon flux operation;
- *dead time*; the time interval between the start of a counted event and the earliest instant at which a new event can be counted.

Other minor features are:

- *sensitivity to polarization*;
- *low sensitivity to static magnetic fields*;
- *simple readout electronics*.

A.2 Different detector type overview

Different types of X-ray detectors (energy range 0.1 – 100 keV) were developed during their long historical evolution, each of them based on its own operation principles and characterized by its performances. In this energy range the photoelectric effect is the most probable interaction between radiation and matter, in particular in high atomic number materials. Main sensor classes are now reviewed.

<u>Gas detectors</u>

The operation principle of these sensors is based on the ionization provoked by X photons incident on gas atoms or molecules due to the photoelectric effect; the first quantitative study on

gas ionization was developed by J. J. Thomson in 1899, and since then several instruments based on this principle were invented:

Ionization chamber

The basic gas detector is the ionization chamber, in which X photons, passing through a radiation window, enter a gas filled chamber (argon, xenon, carbon dioxide), containing two electrodes, and ionize gas particles; if the photon energy is E and the average ionization energy is w, the number of generated ions by each photon is $N=E/w$. A power supply applies to the electrodes a potential difference letting to collect all generated ions (electrons are much faster than positive ions and are the main contributor to the current) without generating other ions by accelerated primary ion collisions with neutral gas particles (saturation regime); in this case the current passing in the supply circuit depends on the incident photon energy, and by its measurement the latter can be evaluated.

Proportional counter

This device is also based on the gas ionization, but the voltage applied to electrodes is greater than in the ionization chamber; ions generated by the X photons are accelerated and gain energies letting them to ionize other gas particles (Towsend discharge); the process gain G is defined as the number of electron-positive ion pair produced by each firstly generated electron, and so the total number of electrons originated by each X photon is $N_T = NG$, in which G can be large as 10^5. Due to the applied voltage all ions are collected by electrodes and the generated current is still proportional to the primary ionization; the advantage of the proportional counter with respect to the ionization chamber is the greater amplitude of the detection signal.

Geiger-Müller counter

The Geiger-Müller counter is a device whose detection signal is the number of incoming X photons, but their energy information can't be obtained; in fact it is also based on a ionization chamber, but it operates in the gas discharge regime, in which each X photon striking gas particles produces ions that gain so much energy to provoke a Towsend discharge in the whole volume of the chamber; also, excited neutral atoms during their decay emit UV radiations, stimulating other electron emission by the cathode, and this origins new discharges; so, in such devices, the dead time is quite long, up to 200 μs, implying very low count rates.

<u>Scintillators</u>

Scintillators are radiation detectors made by high bandgap materials in which a suitable doping with elements called activators produces energetic states sited in the energy gap.

When a X photon strikes the scintillator material electron-hole pairs are created and electrons hops to high energy states; when decaying they are temporarily trapped in activator states, placed at energy levels for which the successive transition to ground state produces the emission of visible light. Such signal can be sent to a photomultiplier to be amplified.

Main scintillator types are: NaI(Tl) – sodium iodide tallium activated; CsI(Tl); CsI(Na); $Bi_4Ge_3O_{12}$.

Scintillators are characterized by a very poor energy resolution (some keV at tens of keV).

Photomultipliers

Photomultipliers are very sensitive detector whose operation principle is the secondary electron emission by metals.

It is constituted by a vacuum tube in which a photocathode emits electrons by photoelectric effect when photons of sufficient energy, depending on the electrode material, strike it; a series of successive electrodes, called dynodes, each of them kept at an electric progressively increasing potential, greater than the cathode one, attract primary and secondary electrons emitted by the previous electrode, and in particular the first dynode collects electrons emitted by the cathode; at the end of this amplification chain the anode, at potential greater than the highest dynode one, collects the whole current.

The photomultiplier gain G, defined as the total electron number generated for each electron emitted by hit photon on the photocathode, is: $G = f^n$, in which f in the secondary electron emission coefficient and n is the number of dynodes.

In this way, by properly designing the photomultiplier with adequate dynode number and material, also the emission of a single electron by the photocathode, apart thermal noise contribution by the electrode material, can be converted in a suitable voltage signal by sending the anode current to a low noise resistor and picking up the related potential difference.

Photomultiplier are often coupled with scintillators for high energy (X and γ rays) photon detection.

Microchannel plates

Microchannel plates (MCP) are both radiation and particle detectors consisting of a very high number (about 10^7) of densely packet, all equal tiny diameter (about 2 – 10 μm) glass channels; each of them operates as an independent, continuous dynode photomultiplier.

These devices are made of lead glass tubes, containing up to 48% in weight of lead oxide, a semiconductor material; at tube ends, coated with electrodes, a suitable (1.5 – 4 keV) potential difference is applied, and they operate at the internal gas pressure less than 10^{-5} Torr. Conventionally, the input face is connected to the highly negative potential, while the opposite end is grounded. When a photon strikes the tube wall at the entrance end a photoelectron is emitted and it's accelerated towards the opposite side of the pipe by the applied field; as the material has a secondary electron emission coefficient greater than 1, a discharge starts and a gain (about 10^8) at the exit end is generally obtained.

In order to increase the quantum detection efficiency, that is in the range 1% - 10 % for soft X rays, materials with high photoelectric yield, in particular cesium iodide, are deposited on the front end of the MCP and on the tube walls.

Semiconductor detectors

Semiconductor detectors are based on the electron-hole pair creation by the photoelectric effect when photons hit material atoms. If E is the energy of the photon and w is the average ionization energy, with $E > w$, $N = E/w$ is the number of electron-hole pairs generated.

A type of semiconductor detector is constituted by a block of material at the opposite ends of which suitable electrodes are placed; by applying a voltage across them a current pulse is generated when a photon is received and charge carrier are generated in the lattice. Of course,

it's necessary to reduce the thermal noise effect to increase both the energy resolution and the sensitivity of the detector; at this aim germanium crystals (energy gap E_g=0,785 eV at T=300K) have to operate at cryogenic temperatures, while high bandgap semiconductor (CdTe, E_g=1.44eV, and CdZnTe, E_g = 1,57 eV) work at room temperature. This last two materials have also the advantage of high Z numbers, so they are well suited to realize high energy detectors.

Charge coupled devices

Charge coupled devices (CCD) are semiconductor radiation detector devices constituted by an array of metal-oxide-semiconductor (MOS) capacitors (cells) connected in rows; electrons are generally majority charge carriers.

When a high logic voltage polarizes a MOS capacitor of the CCD array, a depletion zone is formed under the metal layer, and, if a low logic voltage is applied at both neighbor cells in the same row, charges generated by incoming photons in the depletion zone of that capacitor accumulate in it during the so called frame time, after which the voltage of one side neighbor cell is increased to the high logic level; at this point the accumulated charge starts moving to the new depletion zone, and this process is completed by reducing the first capacitor voltage.

This process is implemented contemporarily at different cells, according to specific sequences, in the same row, and at every row, depending on the CCD type; then single accumulated charges, representing each pixel of the received image, are transferred, row by row, to the conversion circuit to produce the image or its recording in the system memory.

Microwave kinetic inductance detectors (MKIDs)

Superconductor metals working at cryogenic temperatures ($T << T_c$) are characterized by a two component inductance: the magnetic inductance and the kinetic one, related to the kinetic energy of charge carriers (electrons); this second component is relevant in this case due to the negligible Joule effect in superconductors.

The kinetic inductance value is inversely proportional to the quasiparticle density in the superconductor.

In a MKID an inductor characterized by its kinetic inductance L_k is coupled with a capacitor to form a resonant circuit with a very high quality factor, due to its very low resistances, as it operates at cryogenic temperatures. The resonance frequency is in the microwave range.

The operating principle of such devices is based on the displacement of the resonance frequency of the resonant circuit due to the kinetic inductance L_k change of the superconducting inductor (sensing element); this is caused by the quasiparticle density excess generated by Cooper pair breaking caused by suitable energy photon arrival on the detector.

The advantage of such devices with respect to the other microcalorimeters is related to the possibility of reading out several (more than one thousand) detectors by the technique of frequency division multiplexing by designing each microwave resonator with a different resonance frequency.

A.3 Microlithographic process

The microlithography is based on the photoresist, that is a polymeric material constituted by a photoactive compound and an alkaline soluble resin. When radiation of suitable wavelength, depending on the photoresist type, illuminates the polymer, it's chemically modified. Two classes

of photoresist exist: positive and negative one. The first class of polymers, when irradiated, become soluble in base solutions, and the solution concentration sets the dilution speed. Negative photoresists, on the contrary, harden itself when irradiated, and they can be removed in unilluminated areas by specific chemical agents.

Main photoresist properties are:

- resolution: the minimum line width that can be reproduced in the photoresist layer from an areal image;
- contrast: the different answer of the photoresist at light and dark regions;
- sensitivity: minimum energy needed to activate chemical photoreactions for patterning.

Depending on the applications, photoresist can be impressed by visible, ultraviolet, X-ray or electron radiation, with specific threshold wavelengths. The irradiation dose (mJ/cm^{-2}), given by the light intensity times the irradiation (exposure) time, is the energy density which the photoresist is illuminated with; the optimal exposure dose is that minimum value letting the total conversion of the photoinitiator.

For practical reasons, positive photoresistsphotoresist are more advantageous, in particular due to easy and safe development, by simple easily available and cheap chemical solutions (e.g. KOH, NaOH). A general microlithographic process is divided in the following steps:

- photoresist spinning on the substrate;
- photoresist baking;
- photoresist exposure, by direct laser writing technique or by a patterned mask;
- photoresist development.

The single steps will be now detailed described in details.

<u>Photoresist spinning on the substrate</u>

The fotoresist spinning consists in dispensing a polymer drop on the substrate mounted on a chuck spinning at high speed (thousands of rpm). When the drop reaches the substrate, it starts forming a film, that enlargesenlargs while its thickness fastly decreases up to a limit thickness, depending on rotation speed.

The photoresist is a liquid compound, whose viscosity can be controlled by the addiction of a suitable diluent, said thinner; the more viscous the photoresist is, the thicker the film will be at fixed spinning speed.

This process is performed by the photoresist spinner, a machine in which the chuck spinning is speed and time controlled and, in many models, also the acceleration can be set; the substrate is vacuum locked to the chuck.

<u>Photoresist baking</u>

The photoresist baking after the spinning (soft baking) consists in placing photoresist coated samples on a hotplate or in an oven at temperatures around 90 ÷ 100 °C for typical times in the range 1 ÷ 10 min, generally.

In fact, photoresists contain a residual percentage of solvent, after the spinning; baking is required in order to improve its adhesion to the substrate, to avoid its sticking to the mask when used, and to prevent photoresist foaming by nitrogen production during the exposure.

The baking hasn't doesn't have to be too hot or too long, as, in positive photoresists, in these cases a relevant fraction of the photoactive compound is dissolved, and the development time increases.

Photoresist exposure

Photoresist exposure is the process in which the polymer is irradiated by suitable wavelength (energy) light to activate the photochemical reactions that improve causes positive photoresist solubility (or reduce prevents negative photoresist one) in the developer, to let the polymer removing in selected areas.

Photoresist exposure can be executed by the direct writing technique or by patterned masks. The first method requires a focused light (or electron) beam of suitable wavelength (energy) patterning a photoresist coated substrate according to a designed layout.

In the second method, suitable light emitted by a wide and uniform source pass through a mask, perpendicularly to its surface, in the ideal model, to reach the photoresist coated substrate which is placed parallel to the mask at its opposite side with respect to the radiation source.

A microlithographic mask is a structure in which transparent and opaque (for the used radiation) areas are patterned. The radiation illuminating the mask hits the photoresist only through transparent regions, reproducing the mask pattern in it.

The exposure time has to be strictly controlled; in fact, at the fixed light intensity, if the irradiation dose is less than the optimal exposure one, not all the photoinitiator will be transformed to be developed, whilst, if the exposure time produces an excessive exposure dose, due to diffraction also areas that should be covered by the mask will be partially or totally exposed.

Optical lithography uses visible or ultraviolet light, and masks are made of quartz or, for visible light, glass plates on which a patterned metal film, usually chrome, is deposited.

Photoresist exposure is usually performed by a mask aligner, a complex system letting both the relative positioning between the mask and the photoresist coated sample (or another mask plate), and the photoresist exposure with different conditions (proximity, soft contact, hard contact, and others, depending on the model) and doses.

Photoresist development

This process dissolve exposed or unxeposed photoresist, in positive or negative processes respectively, letting pattern areas are open on the substrate; then, such areas can be furtherly processed (e.g., chemical etching or electroplating).

The photoresist development is performed by immersing the sample in a development bath, depending on the polymer type; for positive ones, different concentration base solutions (KOH, NaOH) are usually employed as developers.

After having chosen the solution, both development bath temperature and immersion time are critical parameters; in fact, the higher the bath temperature is, the shorter the development time results, and, if this one is too long with respect to the optimal one (able to dissolve all but only right exposed area photoresist), also under mask exposed areas due to diffraction will be

(partially or totally) dissolved, and the obtained substrate pattern will result enlarged, in particular edges will be evidently rounded.

REFERENCES

[1] https://www.cosmos.esa.int/web/athena

[2] https://heasarc.gsfc.nasa.gov/docs/xrism/

[3] https://wwwastro.msfc.nasa.gov/lynx/docs/presentations/2018-06_Gaskin-10699-v2.pdf

[4] http://astro-h.isas.jaxa.jp/en/the-astro-h-mission/astro-h-overview/

[5] T. Takahashi et al., "The ASTRO-H X-ray astronomy satellite, Proc. of SPIE Astronomical telescopes + instrumentation, v. 9144, 2014.

[6] U. Lo Cicero et al., "Planar array technology for the fabrication of germanium X-ray microcalorimeters", Proc. of IEEE Nuclear Science Symposium Conference Record, NSS'08, 1789-1792, 2008.

[7] U. Lo Cicero et al., "Planar Technology for NDT-Ge X-Ray Microcalorimeters: Absorber Fabrication", Proc. of AIP Conference, 1185, 112-114 (2009).

[8] U. Lo Cicero et al., "Fabrication of Electrical Contacts on Pyramid-Shaped NTD-Ge Microcalorimeters Using Free-Standing Shadow Masks", J. low temp. phys., 167, 541-546 (2012).

[9] U. Lo Cicero et al., "Electroplated indium bumps as thermal and electrical connections of NTD-Ge sensors for the fabrication of microcalorimeter arrays", J. low temp. phys., 167, 535-540, (2012).

[10] G. Villa. et al., "Optical/UV filters for the EPIC experiment", Proceedings of the 1997 IEEE Nuclear Science Symposium, Albuquerque (USA), 1997.

[11] M. Barbera et al., "Calibration of the XRT-SOLARB flight filters at the XACT facility of INAF-OAPA", SPIE Proc. of Astronomical Telescopes + Instrumentation, San Diego (USA), 2004.

[12] M. Barbera et al., "Status of the EPIC thin and medium filters on-board XMM-Newton after more than 10 years of operation II: analysis of in-flight data", Proc. SPIE Optical engineering + applications, v. 8859, 2013.

[13] M. Barbera et al., "Baseline design of the thermal blocking filters for the X-IFU detector on board Athena", Proc. of SPIE Space Telescopes + instrumentations, Montreal (Canada), 2014.

[14] https://aas.org/obituaries/herbert-friedman-1916-2000

[15] P. Testa, "X-ray emission processes in stars and their immediate environment", Proc. of the national academy of sciences of the United States of America, 107, 16, p. 7158, 2010.

[16] https://www.cosmos.esa.int/web/xmm-newton/home

[17] http://www.chandra.si.edu

[18] M. S. Longair, High energy astrophysics, Cambridge University Press, 3rd ed., 2011.

[19] E. Brocato et al., "La visione strategica dell'INAF per l'astronomia italiana 2015 – 2024", INAF – Istituto nazionale di astrofisica, http://www.inaf.it/it/sedi/sede-centrale-nuova/consiglio-scientifico/Vision_I.pdf

[20] M. Branchesi, "Multi messanger astronomy: gravitational waves, neutrinos, photons, and cosmic rays", J. phys. conf. series, 718, 2016.

[21] https://dcc.ligo.org/public/0145/P1700294/007/ApJL-MMAP-171017.pdf

[22] M. Guainazzi and M. S. Tashiro, "The hot universe with XRISM and Athena", Proc. IAU Symp. n. IAUS342, 2019.

[23] http://astro-h.isas.jaxa.jp/en/the-astro-h-mission/astro-h-overview/

[24] M. A. Leutenegger et al. "In-flight verification of the calibration and performance of the ASTRO-H (Hitomi) soft X-ray spectrometer", SPIE proc. Astronomical telescopes + instrumentation 2016, v. 9905, 2016.

[25] https://heasarc.gsfc.nasa.gov/docs/xrism/
[26] X._Barcons et al., “Athena: the X-ray observatory to study the hot and energetic Universe”, Journal of Physics, Conference Series, V. 610, 1, 2015.
[27] K. Nandra et al., “The Hot and Energetic Universe: A White Paper presenting the science theme motivating the Athena+ mission," e-print arXiv:1306.2307, 2013.
[28] R. Willingale et al., "The Hot and Energetic Universe: The Optical Design of the Athena Mirror", e-print arXiv:1307.1709W, 2013.
[29] M. Bavdaz et al., “The ATHENA telescope and optics status”, Proc. SPIE, 10399, 2017.
[30] D. Barret et al., “The Athena X-ray Integral Field Unit (X-IFU),” Proc. SPIE, 9905, 2016.
[31] F. Pajot et al., “The Athena X-ray Integral Field Unit (X-IFU)”, JLTP, 2018. doi:10.1007/s10909-018-1904-5.
[32] A. Rau et al., "The Hot and Energetic Universe: The Wide Field Imager (WFI) for Athena", e-print arXiv:1308.6785 (2013).
[33] N Meidinger et al., “The Wide Field Imager instrument for Athena,” Proc. SPIE, 10397, 2017.
[34] https://wwwastro.msfc.nasa.gov/lynx/docs/presentations/2018-06_Gaskin-10699-v2.pdf
[35] M. Barbera, ”Thermal Filters for the ATHENA X-IFU: Conceptual Design, Performance Modelling and Preliminary Characterization Tests”, XIFU-UNPA-THF-TN-0001, 2019.
[36] R. A. Mewald, ”Cosmic rays”, Macmillan encyclopedia of physics, v. 1, Simon & Schuster Macmillan, New York, 1996.
[37] S. Gabici et al., ”The origin of galactic cosmic rays: challenges to the standard paradigm”, submitted to Frontiers in Astronomy and Space Science, special issue, "Multi-Messenger Astrophysics: New Windows to the Universe", 2019.
[38] T. Takahashi et al., ”The ASTRO-H X-ray astronomy satellite”, SPIE proc. Astron. Telesc. And instrum. 2014.
[39] L. E. Casano, ”I rivelatori di radiazioni”, Dispense di fisica applicata, V ed., 2004.
[40] G. W. Fraser, ”X-ray detectors in astronomy”, Cambridge university press, 1989.
[41] S. O. Flyckt and C. Marmonier, ” Photomultiplier tubes – principles & applications”, Brive, France, 2002.
[42] R. A. Jansen, ”Basics of CCDs and astronomical imaging”, AST 598/494 “The distant universe” course, ASU, 2014.
[43] B. A. Mazin, ”Microwave kinetic inductance detector: the first decade”, Thirteenth int. work. on Low Temperature Detectors-LTD13, AIP Conf. Proc., 1185, 1, p. 135, 2009.
[44] P. A. J. De Korte, ”Cryogenic imaging spectrometers for X ray astronomy”, Nucl. inst. meth. phys res. A, 444, p. 163, 2000.
[45] S. Bandler et al., ”NTD Ge based microcalorimeter performance”, Nucl. Instr. and Meth. in Phys. Res. A Accelerators Spectrometers Detectors and Associated Equipment, 444, 2000.
[46] M. Maeda et al., ”Development of TES microcalorimeter for high precision spectroscopy of LX-rays from transuranium elements”, Progr. in nucl. sci. tech., 1, p. 226, 2011.
[47] E. Silver et al., ”An NTD germanium-based microcalorimeter with 3.1 eV at 6 keV”, Nucl. inst. Meth. in phys. Res. A, 545, 2005.
[48] S. Friedrich, ”Cryogenic X-ray detectors for synchrotron science”, J. synchrot. rad., 13, 159, 2006.
[49] E. Silver et al., ”NTD-germanium based microcalorimeters for hard X-ray spectroscopy”, Proc. SPIE 4140, 2000.
[50] A. R. Miniussi et al., ”Performance of an X-ray microcalorimeter with a 240 μm absorber and a 50 μm TES bilayer”, J. low temp. phys. 193, 2018.

[51] S. Kempf, ”Physics and applications of magnetic metallic microcalorimeters”, J. low temp. phys., 193, 2018.
[52] S. Friedrich et al., ”Magnetic microcalorimeter gamma-detectors for high-accuracy nuclear decay data”, Lawrence Livermore National Laboratory report LLNL-TR-755521.
[53] M. Daal et al., ”Results from X-ray microcalorimeter arrays based on thermal MKIDs (TKIDs)”, 18th Int. work. low temp. detect., Milano (Italy), 2019.
[54] G. Ulbricht et al., ”Highly multiplexable thermal kinetic inductance detectors for x-ray imaging spectroscopy”, Appl. phys. lett., 106, 2015.
[55] R. L. Kelley et al., ”The microcalorimeter spectrometer on the ASTRO-E X-ray observatory”, Nucl. instrum. And meth. in phys. res. A, 444, 2000.
[56] ESA’s Athena L2 payload definition document, 2014.
[57] M. Barbera et al., ”Thermal filters for the Athena X-IFU: ongoing activities towards the conceptual design”, J. low. temp. phys, 184, 3-4, 2016.
[58] https://heasarc.gsfc.nasa.gov/docs/xrism/
[59] M. E. Eckart et al., ”Design of IR/optical blocking filter for the Lynx X-ray microcalorimeter”, J. Astron. Telesc., instrum., and syst., 5, 2019.
[60] S. Musset et. al., ”Diffusive transport of energetic electrons in the solar corona: X-ray and radio diagnostics”, Astron. and Astrophys., 610, 2018.
[61] R. P. Lin et al., ”The Reuven Hamaty high-energy solar spectroscopic imager (RHESSI) mission”, SPIE proc. 5171, 2004.
[62] F. Effenberger et al., ”Hard X-ray emission from partially occulted solar flares: RHESSI observations in two solar cycles”, The astrophys j., 835, 2017.
[63] I. G. Hannah et al., ”The First X-Ray Imaging Spectroscopy of Quiescent Solar Active Regions with NuSTAR”, The Astrophysical Journal Letters, 820, L14, 2016.
[64] N. P. Palaio, ”Development of neutron-transmutation-doped germanium bolometer material”, Thesis, Lawrence Berkeley Laboratory, University of California, Berkeley (CA), 1983.
[65] I. S. Shlimack, ”Neutron transmutation doping in semiconductors: science and applications”, Phys. sol. state, 41, 5, 1999.
[66] N. Fukuoka and H. Saito, ”Defects in neutron-transmutation-doped germanium”, Jap. jour. appl. phys., 23, 1, 2, 1984.
[67] https://physics.nist.gov/PhysRefData/XrayMassCoef/chap2.html
[68] H. Hirayama, ”Lecture note on photon interactions and cross sections”, International conference on the Monte Carlo 2000, Lisbona, 2000.
[69] J. H. Scofield, ”Theoretical photoionization cross sections from 1 to 1500 keV”, Lawrence Livermore laboratory report UCRL 51326.
[70] https://physics.nist.gov/PhysRefData/XrayMassCoef/tab3.html
[71] P. Duthil, ”Material properties at low temperature”, CERN Yellow report, CERN-2014-005, p.77, 2015.
[72] M. Tinkam, ”Introduction to superconductivity”, Dover, 2004.
[73] R. J. Corruccini and J. J. Gniewek, ”Specific heats and enthalpies of technical solids at low tenperatures”, National bureau of standards monograph 21, United States Department of Commerce, 1960.
[74] “Thermal conductivity – Theory, properties and applications”, T. M. Tritt ed., Kluwer, 2004.

[75] U. Kobler, ”On the thermal conductivity of metals and insulators”, Int. j. thermod., 20, 4, p. 210, 2017.
[76] G. Davey et al., ”Heat conductivity of ore metals below 1 °K”, Proc. of IX int. conf. on Low Temp. Phys. LT9, Columbus (USA), 1964.
[77] R. L. Powell and W. A. Blampied, ”Thermal conductivity of metals and alloys at low temperatures”, National bureau of standards circular 556, United States Department of Commerce, 1964.
[78] N. F. Mott, ”Conduction in non-crystalline materials – III. Localized states in a pseudogap and near extremities of conduction and valence bands”, Phil. Mag., 19, 835, 1969.
[79] “Hopping transport in solids”, M. Pollak and B. I. Shklovskii ed., Elsevier, Amsterdam, 1991.
[80] K. M. Itoh, ”Variable range hopping conduction in neutron transmutation doped ^{70}Ge:Ga”, Phys. stat. sol. (b), 218, 211, 2000.
[81] A. L. Danilyuk et al., ”Low temperature conductivity in n-type uncompensated silicon below insulated-metal transition”, Adv. cond. Matt. Phys., 2017, 5038462, 2017.
[82] A. L. Woodcraft et al., ” Hopping conduction in NTD germanium: comparison between measurement and theory”, J. low temp. phys., 134, 3, 2004.
[83] A. Alessandrello et al., ”Fabrication and low-temperature characterization of Si-implanted thermistors”, J. Phys. D: appl. phys. 32, p. 3099, 1999.
[84] M. Galeazzi, D. McCammon, ”Microcalorimeter and bolometer model”, J. appl. phys., 93, 8, 2003.
[85] N. F. Mott, ”Conduction in glasses containing transition metal ions”, J. non-crys. Sol., 1, 1, 1968.
[86] A. L. Efros and B. I. Shklovskii, ”Coulomb gap and low temperature conductivity of disordered systems”, J. Phys. C, 8, 4, 1975.
[87] M. Pollack, ”The Coulomb gap: a review, and new developments”, J. Phil. Mag. B, 65, 4, 1992.
[88] B. I. Shklovskii and A. L. Efros, ”Electronic properties of doped semiconductors”, Springer-Verlag, Berlin, 1984.
[89] M. Pollak, "Effect of carrier-carrier interactions on some transport properties in disordered semiconductors", Discussions of the Faraday Society, 50, 13,1970.
[90] N. F. Mott, ”Metal-insulator transition”, Taylor and Francis, London, 1990.
[91] J. Soudée et al., ”Hot electrons effect in a #23 NTD Ge sample”, J. low temp. phys., 110, 5/6, 1998.
[92] E. Pasca et al., ”Low temperature properties of NTD Ge: best choice for CUORE experiment”, Proc. of 8th conf. on Astroparticle, Particle, Space Physics, Radiation Interaction, Detectors and Medical Physics Applications, Como (Italy), 2003.
[93] M. Piat et al., ”Design and tests of high sensitivity NTD Ge thermometers for the Plank-High frequency instrument”, Low temperature detectors, edited by F. Porter et al., American Institute of Physics, 2002.
[94] G. Ventura, M. Perfetti, ”Thermal properties of solids at room and cryogenic temperatures”, Springer, Dordrecht, 2014.
[95] S. Moseley et al., ”Thermal detectors as x-ray spectrometers”, J. appl. phys., 56, 1984.
[96] A. Giachero, ”Characterization of cryogenic bolometers and data acquisition system for the CUORE experiment”, PhD thesis, 2008.
[97] N. Wang et al., ”Electrical and thermal properties of neutron-transmutation-doped Ge at 20 mK”, 41, 3761, 1990.

[98] D. A. Bennett et al., ”Microwave SQUID multiplexing for the Lynx x-ray microcalorimeter”, J. Astron. telesc., instr. and syst., 5, 2019.
[99] W. B. Doriese et al., ”A practical superconducting-microcalorimeter x-ray spectrometer for beamline and laboratory science”, Rew. scient. instr., 88, 2017.
[100] S. J. Smith et al., ”Development of arrays of position-sensitive microcalorimeters for Constellation-X”, SPIE proc. of Space telescopes and instrumentation 2008, v. 7011, 2008.
[101] E. Silver et al., ”High resolution X-ray spectroscopy using germanium microcalorimeters”, 33th SPIE ann. tech. symp. on optical and optoelectronical applied science and engineering, San Diego (CA), 1989.
[102] E. Silver et al., ”X-ray and gamma-ray astronomy with NTD germanium-based microcalorimeters”, AIP Conf. proc., 605, 1, 555, 2002.
[103] J. Beeman et al., ”The Constallation-X focal plane microcalorimeter array: a NTD-germanium solution”, Proc. 9th int. work. Low temp. detect., 605, p. 211, 2002.
[104] E. Silver et al., ”X-ray imaging spectroscopy using an NTD Ge-based microcalorimeter: an interdisciplinary spin off from astrophysics research”, Microsc. Microanal. 16 (suppl.2), 2010.
[105] E. Silver (PI), et al., "X-ray Spectroscopic Explorer (XRASE)", 1998, Proposal submitted to the NASA MIDEX program AO-98-03-OSS-036.
[106] E. Silver (PI), et al., "Baloon-borne MIcrocalorimeter Nuclear line Explorer (B-MINE)", 2000, Proposal submitted to the NASA SMEX program A0-99-05-OSS-048.
[107] G. Peres (PI) et al., "CALorimetri per Osservazioni Solari (CALOS)", 2001, Proposal for a scientific satellite presented to the ASI Bando Nuove Idee di Missioni - March 2001.
[108] E.H. Silver (PI), et al., "INternational Spectro-Polarimetric Imaging x-Ray Explorer (INSPIRE)", 2001, Proposal submitted to the NASA MIDEX program AO-01-OSS-03.
[109] E.H. Silver (PI), et al., "PolaRIZation Explorer (PRIZE)", 2003, Proposal submitted to the NASA program SMEX03-0000-0025.
[110] F. Reines & C. L. Cowan jun., ”The neutrino”, Nature, 178, p.446, 1956.
[111] Y. Fukuda et al., ”“Evidence for oscillation of atmospheric neutrinos”, Phys. rev. lett., 81, p. 1562, 1998.
[112] V. M. Lobashev et al., “Direct search for mass of neutrino and anomaly in the tritium beta-spectrum”, Phys. lett. B, 460, p. 227, 1999.
[113] L. Cardani, ”Neutrinoless double beta decay overview”, Proc. 15th int. work. on tau lepton phys., Amsterdam (The Netherlands), 2018.
[114] M. Goeppert-Mayer, ”Double beta-disintegration”, Phis. rev., 48, 512, 1935.
[115] C. E. Aalseth et al., “Recent results of the IGEX Ge-76 double-beta decay experiment,” Phys atom. nucl., 63, p. 1225, 2000.
[116] H. V. Klapdor-Kleingrothaus et al., ”Search for neutrinoless double beta decay with enriched Ge-76 in Gran Sasso 1990-2003,” Phys. Lett. B, 586, p. 198, 2004.
[117] https://cuore.lngs.infn.it
[118] A. Caminata et al., ”Results from the CUORE experiment”, Universe, 5, 10, 2019.
[119] E. Andreotti et al., ”^{130}Te neutrinoless double-beta decay with CUORICINO”, Astrop. Phys., 34, 11, 2011.
[120] C. Alduino et al., ”CUORE-0 detector: design, construction and operation”, J. instrum., 11, 2016.
[121] Annika H. G. Peter, ”Dark matter: a brief review”, Proc. of science, Frank N. Bash symposium 2011: New horizons in astronomy, Austin (USA), 2011.

[122] E. Armangaud et al., ”Searching for low-mass dark matter particles with a massive Ge bolometer operated above-ground”, Phys, rev. D, 99, 2019.
[123] E. Perinati et al., ”Experimental evidence of an incomplete thermalization in a X ray microcalorimeter with a Ta/Au absorber”, Rev. of scient. instrum., 79, 2008.
[124] R. D. Horansky et al., ”Superconducting absorbers for use in ultra-high resolution γ-ray spectrometers based on low temperature microcalorimeter arrays”, Nucl. instr. and meth. in phys. res. A, 579, 2007.
[125] M. C. Gaidis et al., ”A superconducting X-ray spectrometer with a tantalum absorber and lateral trapping”, IEEE Trans. on appl. superconduc., 6, 1996.
[126] S. R. Bandler et al., ”Performance of TES X-ray microcalorimeters with a novel absorber design”, J. of low temp. phys., 151, 2008.
[127] https://physics.nist.gov/PhysRefData/XrayMassCoef/tab3.html
[128] T. Jones, ”Electrodeposition of osmium”, Metal finish., 100, 2002.
[129] A. Naor et al., ”Electrodeposition of alloys of rhenium with iron-group metals from acqueous solutions”, J. electrochem. soc., 157, 2010.
[130] A. Brown et al., ”Absorber materials for transition-edge sensor X-ray microcalorimeters”, J. low temp. phys., 151, 2008.
[131] S. Jiang et al, ”Synthesis of bismuth with various morphologies by electrodeposition”, Inorg. Chem. Comm., 6, 2003.
[132] L. S. Kothari and V. K. Tewary, ”Calculations on the low temperature specific heat of bismuth”, Phys. lett., 6, 1963.
[133] Encyclopedia Britannica, https://www.britannica.com/science/bismuth
[134] N. A. Lange, ”Manuale di chimica”, UTET – Sansoni Edizioni scientifiche, 1970.
[135] B. L. Henke et al., ” X-ray interactions: photoabsorption, scattering, transmission, and reflection at E=50-30000 eV, Z=1-92, Atomic Data and Nuclear Data Tables, 54, 181, 1993.
[136] D. H. Kim. et al., ”Structure and electrical transport properties of bismuth thin films prepared by RF magnetron sputtering”, Appl. Surf. Sci**.,** 252, 3525-3531, 2006.
[137] R. Pauliukaite et al., ”Characterization and applications of a bismuth bulk electrode”, Electroanal., 16**,** 719-723, 2004.
[138] J. H. Mangez et al., ”Transport properties of bismuth in quantizing magnetic fields”, Phys. Rev B, 14**,** 4381-4385, 1976.
[139] E. Camps et al., ”A Detailed Study of the Synthesis of Bismuth Thin Films by PVD-Methodsand their structural characterization”, MRS online proc. libr. arch., 1477, 2013.
[140] L. Kumari et al., ”Effects of deposition temperature and thickness on the structural properties of thermal evaporated bismuth thin films”, Appl. Surf. Sci., 253, 14, 5931, 2007.
[141] M. F. Ortiz et al., ”Bismuth coatings deposited by the pulsed dc sputtering technique”, Rev. mex. de fis., 59, 374-379, 2013.
[142] M. Boffoué et al., ”Structure and transport properties of polycrystalline Bi films”, J. Phys. Chem. Solids **61**, 1979 (2000).
[143] Y. Ahn et al., ”Thickness dependent surface microstructure evolution of bismuth thin film prepared by molecular beam deposition method”, Curr. Appl. Phys. 12, 1518 (2012).
[144] W. Dingley et al., ”Plating and Surface Finishing 63, 4, 26, 1978.
[145] S. Stanley, M. Cropper, ”Structure and resistivity of bismuth thin films deposited by pulsed DC sputtering”, Loughborough University, Journal contribution.

[146] N. Kanani, ”Basic principles, processes and practice”, Elsevier, Oxford, 2004.
[147] H. Wang and L. Pilon, ”Accurate simulations of electrical double layer capacitance on microelectrodes”, J. phys. chem. 115, 2011.
[148] H. H. Lou, Y. Huang, ”Electroplating”, in Encyclopedia of chemical processing, Taylor and Francis, New York, 2006.
[149] R. G. Ehl, I. Aaron, ”Faraday’s electrochemical laws and the determination of equivalent weights”, J. Chem. Ed., 31, 226 – 232, 1954.
[150] L. M. Gades et al., ”Development of thick electroplated bismuth absorbers for large collection area hard X-ray transition edge sensors”, IEEE Trans. on applied superconductivity, v. 27, n. 4, 2017.
[151] P. Cereceda-Company and J. L. Costa-Kramer, ”Electrochemical growth of bismuth for X-ray absorbers”, J. Electrochem. Soc., 165, 5, D167, 2018.
[152] A. Chiba, T. Kojiama, ”Sono-electroplating of bismuth film form Bi(III)-EDTA bath”, e-Journal of surface science and nanotechnology, v. 7, 2009.
[153] A. Krolicka et al., ”Effect of electroplating variables on the voltammetric properties of bismuth deposits placed potentiostatically”, Electroanalysis, 18, 2006.
[154] M. Pourbaix, “Atlas of Electrochemical Equilibria in Aqueous Solutions”, Pergamon Press, Oxford, 534-536, 1966.
[155] R. S. Nicholson, “Theory and Application of Cyclic Voltammetry for Measurement of Electrode Reaction Kinetics”, Anal. Chem., 37, 1351-1355, 1965.
[156] S. Ferruggia Bonura et al., “Electroplated bismuth absorbers for planar NTD-Ge sensor arrays applied to hard X-ray detection in astrophysics”, SPIE Astronomical telescopes + instrumentation, Austin (Texas), June 10 – 15, 2018.
[157] L. F. Thompson et al., ”Introduction to microlithography”, Am. Chem. Soc. symp. Series, Washington DC, 1983.
[158] A. J. Garratt-Reed and D. C. Bell, ”Energy dispersive X-ray analysis in the electron microscope”, Bios scientific publisher ltd., 2003.
[159] M. Deen, F. Pascal, ”Electrical characterization of semiconductors materials and devices”, in Springer Handbooks of electronic and photonic materials, Springer, 2017.
[160] M. E. Orazem & B. Tribollet, ”Electrochemical impedance spectroscopy”, Wiley, Hoboken (NJ, USA), 2008.
[161] D. A. Harrington, ”Electrochemical impedance spectroscopy”, notes for the electrochemical impedance spectroscopy course, Norwegian University of Science and technology, 2004.
[162] https://www.micro-epsilon.com/download/products/cat-confocal/dax--confocalDT-IFS2405--en-us.html
[163] https://www.micro-epsilon.com/download/manuals/man--confocalDT-2421-2422--en.pdf
[164] S. Ferruggia Bonura et al., ”Fabrication of Bismuth Absorber Arrays for NTD-Ge Hard X-ray Microcalorimeters”, submitted to J. low temp. phys..
[165] https://ecss.nl/standards/ecss-document-tree-and-status/
[166] E. Bozzo et al., “The filter wheel and filters development for the X-IFU instruments onboard Athena”, Proc. SPIE, 9905, 2016.
[167] M. Barbera et al., ”The optical blocking filter for the Athena Wide Field Imager: ongoing activities towards the conceptual design”, Proc. SPIE 9601-8, 2015.
[168] M. Barbera et al., ”ATHENA X-IFU thermal filters development status toward the end of the instrument phase A”, Proc. of SPIE, v. 10699, 2018.

[169] G. Parodi et al., ”Structural modeling and mechanical tests supporting the design of the ATHENA X-IFU thermal filters and WFI blocking filters”, Proc. of SPIE, v. 10699, 2018.
[170] https://www.dupont.com/electronic-materials/polyimide-films.html
[171] D. McCammon et al., ”The X-ray quantum calorimeter sounding rocket experiment: improvements for the next flight”, J. low temp. phys., 151, 3-4, 2008.
[172] https://jwst.nasa.gov/content/about/innovations/coating.html
[173]https://www.dupont.com/content/dam/dupont/products-and-services/membranes-and-films/polyimde-films/documents/DEC-Kapton-summary-of-properties.pdf
[174] R. Wolf et al., ”Optical constants of polyimide films in the soft X-ray region from reflection and transmission measurements”, Appl. opt., 31, 34, 1992.
[175] https://www.accuratus.com/silinit.html
[176] N. Montinaro et al., ”Deformation analysis of ATHENA test filters made of plastic thin films supported by a mesh under static differential pressure”, IEEE Int. work. on metrology for aerospace 2019 (IEEE MetroAeroSpace 2019), June 19-21, 2019, Torino (Italy).
[177] U. Lo Cicero et al., ”Radio frequency shielding of thin aluminized plastic filters investigated for the ATHENA X-IFU detector”, Proc. SPIE 10699, 2018.
[178] R. A. Mewaldt et al., ”Long-term fluences of solar energetic particles from H to Fe”, Space Science Review, 130, 2007.
[179] R. A. Mewaldt, ”Solar energetic particle composition, energy spectra and space weather”, Space science reviews, 124, 2006.
[180] http://swe.ssa.esa.int/space-radiation
[181] National academies of Science, Engineering, Medicine:“Testing at the speed of light – The state of U.S. electronic parts space irradiation testing infrastructure”, The national academic press, Washington D.C., 2018.
[182] A. Kinomura et al., ”Damage of polyimide thin films irradiated by MeV proton microbeams”, Nucl. instr. meth. phys. res. B, 104, 1995.
[183] R. Li et al., ”Damage effect of keV proton irradiation on aluminized Kapton film”, Rad. phys. chem., 77, 2008.
[184] Y. Wu et al., ”A study on the free-radical evolution and its correlation with the optical degradation of the 170 keV proton irradiated polyimide”, Pol. degrad. stab., 95, 2010.
[185] D. C. Ferguson, ”Laboratory degradation of Kapton in a low energy oxygen ion beam”, NASA Technical memorandum 83530, 1983.
[186] J. M. Costantini et al., ”Space-charge formation and relaxation in ion-bombarded poly(imide) Kapton films”, Nucl. instr. meth. phys. res. B, 116, 1996.
[187] D. W. Kim et al., ”Influence of MeV protons on mechanical properties of ITO/aluminum-coated Kapton designed for space missions”, Nucl. instr. meth. phys. res. B, 266, 2008.
[188] H. S. Virk, ”Physical and chemical response of 70 MeV carbon ion irradiated Kapton-H polymer”, Nucl. instr. meth. phys. res. B, 191, 2002.
[189] D. Severin et al., ”Degradation of polyimide under irradiation with swift heavy ions”, Nucl. instr. meth. phys. res. B, 236, 2005.
[190] H. Shimamura, T. Nakamura, ”Investigation of degradation mechanisms in mechanical properties of polyimide films exposed to a low earth orbit environment”, Pol. deg. stab., 95, 2010.
[191] C. Li et al., ”Effect of electron exposure on optical properties of aluminized polyimide films”, J. mat. res., 17, 2002.

[192] R. Li et al., ”Radiation effect of keV protons on optical properties of aluminized Kapton film”, Rad. phys. chem., 76, 2007.
[193] B. Canut et al., ”Ion-induced tracks in amorphous Si_3N_4 films”, Nuclear Instruments and methods in physics research B, 266, 2008.
[194] G. Szenes.”General features of latent track formation in magnetic insulators irradiated with swift heavy ions”, Phys. Rev. B, 51, 1995.
[195] Y. Morita et al., ”Surface effect on ion track formation in amorphous Si_3N_4 films”, Nuclear Instruments and methods in physics research B, 315, 2013.
[196] B. Canut et al., ”Swelling and optical properties of Si_3N_4 films irradiated in the electronic regime”, The seventh international symposium on swift heavy ions in matter, Lyon (France), 2008.
[197] M. Matsunami et al., ”Ion irradiation effects on optical properties of silicon nitride films”, Surface and coating technology, 201, 2007.
[198] http://gwyddion.net/
[199] https://www.itl.nist.gov/div898/handbook/eda/section3/eda35b.htm
[200] U. Sarac and M. C. Baykul, ”Evolution of surface roughness parameters and microstructures in two-phase nanocrystalline Cu-Co films electrodeposited onto ITO coated glass substrates at different deposition potentials”, J. mat. sci: mat. electron., 25, 2013.
[201] “X-Ray absorption and X-ray emission spectroscopy: theory and applications”, J. A. van Bokhoven, C. Lamberti ed., Wiley, 2016.

PUBLICATIONS

This section lists publications produced during this PhD, both already published, or presently in preparation.

1. M. Barbera,…, **S. Ferruggia Bonura** et al.:”Shielding characteristic changes of thin silicon nitride filters for X-ray cryogenic sensors due to space particle irradiation”, in preparation.

2. F. Di Franco,…, **S. Ferruggia Bonura** et al.: ”Optimization of electrodeposition process of bismuth layers as X-ray absorbers”, in preparation.

3. **S. Ferruggia Bonura** et al.:”Fabrication of Bismuth Absorber Arrays for NTD-Ge Hard X-ray Microcalorimeters”, Presented at the 18th International Workshop on Low Temperature Detectors (LTD18), Milano, July 22-26, 2019.

4. N. Montinaro,…, **S. Ferruggia Bonura** et al.:”Deformation analysis of ATHENA test filters made of plastic thin films supported by a mesh under static differential pressure”, IEEE Int. work. on metrology for aerospace 2019, June 19-21, 2019, Torino (Italy).

5. **S. Ferruggia Bonura** et al. "Electroplated bismuth absorbers for planar NTD-Ge sensor arrays applied to hard x-ray detection in astrophysics," Proc. SPIE 10709, High Energy, Optical, and Infrared Detectors for Astronomy VIII, 107092D, 2018.

6. M. Barbera, …,**S. Ferruggia Bonura**, et al.:"ATHENA XIFU thermal filters development status toward the end of the instrument phase-A," Proc. SPIE 10699, Space Telescopes and Instrumentation 2018: Ultraviolet to Gamma Ray, 106991R, 2018.

7. G. Parodi, …, **S. Ferruggia Bonura**, et al.:"Structural modelling and mechanical tests supporting the design of the ATHENA X-IFU thermal filters and WFI optical blocking filter," Proc. SPIE 10699, Space Telescopes and Instrumentation 2018: Ultraviolet to Gamma Ray, 106994C, 2018.

8. U. Lo Cicero, …, **S. Ferruggia Bonura**, et al.:"Radio frequency shielding of thin aluminized plastic filters investigated for the ATHENA X-IFU detector," Proc. SPIE 10699, Space Telescopes and Instrumentation 2018: Ultraviolet to Gamma Ray, 106994R, 2018.

9. L. Sciortino, …, **S. Ferruggia Bonura**, et al.:"Thermal modelling of the ATHENA X-IFU filters," Proc. SPIE 10699, Space Telescopes and Instrumentation 2018: Ultraviolet to Gamma Ray, 1069950, 2018.

10. M. Barbera, …, **S. Ferruggia Bonura**,et al.:”Preliminary Mechanical Characterization of Thermal Filters for the X-IFU Instrument on Athena”, Journal of Low Temperature Physics, 2018.

11. L. Sciortino, …, **S. Ferruggia Bonura**, et al.:A temperature dependent X-ray absorption characterization of test filters for the ATHENA mission X-IFU instrument, Journal of Low Temperature Physics, 193, 2018.

12. G. Tumminelli, …, **S. Ferruggia Bonura**, et al.:"Towards an AMTEC-like device based on non-alkali metal for efficient, safe and reliable direct conversion of thermal to electic power", AEIT International annual conference 2018, Bari, 3 – 5 ottobre 2018.

13. G. Tumminelli, …, **S. Ferruggia Bonura**, et al.:"A thermodynamic-statistical model of the electrical characteristics of a 2nd generation AMTEC-type cell for the renewable heat-to-electrical energy direct conversion", submitted to AIP – Journal of renewable and sustainable energy (2018).

14. **S. Ferruggia Bonura** et al. NTD Ge microcalorimeters for hard X-ray solar observation, XIV School of synchrotron radiation: fundamentals, methods and applications, Muggia (TS), 18-29/9/2017.

15. U. Lo Cicero, …, **S. Ferruggia Bonura**, et al.: "Electrical contacts on germanium at cryogenic temperatures (<300 mK)", presented at the 17th Int. Workshop on low temperature detectors (LTD17), Kurume, Japan, 17 - 21/7/2017.

AKNOWLEDGMENTS

The author of this thesis wishes to thank his tutor prof. Marco Barbera, of the Dipartimento di Fisica e Chimica of the Università di Palermo, and his co-tutor dr. Ugo Lo Cicero, of the National Institute for Astrophysics – Astronomical Observatory of Palermo, for their scientific support and useful suggestions during all this Ph.D. course, and for careful revisions of this thesis.

The author is also grateful to dr. Alfonso Collura of the National Institute for Astrophysics – Astronomical Observatory of Palermo, to dr. Clint Bockstiegel, to dr. Giulia Collura and to dr. Luisa Sciortino of the Dipartimento di Fisica e Chimica of the Università di Palermo for helpful suggestions and careful revisions of this thesis.

Many thanks also to prof. Monica Santamaria, dr. Francesco Di Franco and dr. Andrea Zaffora, of the Electrochemical Material Science Laboratory of the Università di Palermo - Dipartimento di Ingegneria, for long lasting hosting in their laboratory to perform experimental electrochemistry activity and for helpful research collaboration.

Many thanks also to dr. Daniele Gulli, of the National Institute for Astrophysics – Astronomical Observatory of Palermo, that strictly collaborated to the electrochemistry research for bismuth absorber fabrication.

The author wishes also to thank prof. Simonpietro Agnello and dr. Giampiero Buscarino, of the Dipartimento di Fisica e Chimica of the Università di Palermo, and dr. Luigi Botta, of the Dipartimento di Ingegneria of the Università di Palermo, for helpful research collaboration.

Many thanks also to ing. Giuseppe Lo Cicero, dr. Nicola Montinaro, dr. Elena Puccio, and dr. Michela Todaro, of the National Institute for Astrophysics – Astronomical Observatory of Palermo, and to ing. Anna Maniscalco, of the Dipartimento di Ingegneria of the Università di Palermo, for helpful research collaboration.

The author wishes also to thank ing. Salvatore Varisco, Mr. Roberto Candia and Mr. Gaspare Di Cicca, of the National Institute for Astrophysics – Astronomical Observatory of Palermo, for technical collaboration to the development of different phases of this research.

The author wishes also to thank very much his mother, prof. Emanuela Spotorno, for having encouraged this very interesting work.